

Proposal for the ESA F Mission Programme
March 20, 2019

This proposal is submitted on behalf of the All-Sky-ASTROGAM Collaboration by:

A. De Angelis (INFN & INAF Padova; Univ. Udine and Padova, Italy; LIP/IST Lisboa, Portugal);
V. Tatischeff (CSNSM, France); M. Tavani (INAF/IAPS, Roma, Italy); U. Oberlack (University
Mainz, Germany); R. Walter (University of Geneva, Switzerland); G. Ambrosi (INFN Perugia,
Italy); A. Argan (INAF Headquarters, Italy); P. von Ballmoos (IRAP, France); S. Brandt (DTU
Space, Denmark); A. Bulgarelli (INAF/OAS-Bologna, Italy); A. Bykov (Ioffe Institute, Russia); V.
Fioretti (INAF/OAS-Bologna, Italy); I.A. Grenier (AIM Saclay, France); L. Hanlon (UC Dublin,
Ireland); D. Hartmann (Clemson University, USA); M. Hernanz (CSIC-IEEC, Barcelona, Spain);
G. Kanbach (MPI Garching, Germany); I. Kuvvetli (DTU Space, Denmark); P. Laurent (APC,
France); M.N. Mazziotta (INFN Bari, Italy); J. Mc Enery (NASA GSFC, USA); S. Mereghetti
(INAF/IASF, Milano, Italy); A. Meuris (CEA Saclay, LSAS, France); A. Morselli (INFN Roma
"Tor Vergata", Italy); K. Nakazawa (University of Tokyo, Japan); M. Pearce (KTH Stockholm,
Sweden); R. Rando (INFN Padova, Italy); J. Rico (IFAE-BIST, Barcelona, Spain); R. Curado da
Silva (LIP Portugal); X. Wu (University of Geneva, Switzerland); A. Zdziarski (NCAC, Poland);
A. Zoglauer (UC Berkeley, USA)

Contact Information

Lead proposer: Prof. Alessandro De Angelis, INFN and INAF Padova
c/o Dipartimento di Fisica e Astronomia “Galileo Galilei”
via Marzolo 8, Padova I-35131, Italy
Tel. +39 391 3484634
e-mail alessandro.deangelis@pd.infn.it

The Lead Proposer declares that he will support the study activities by making available at least 20% of his time throughout the study period.

Co-Lead proposer: Dr. Vincent Tatischeff,
CSNSM, CNRS and University of Paris Sud F-91405, Orsay, France
Tel. +33 01 69 15 52 41
e-mail Vincent.Tatischeff@csnsm.in2p3.fr

Contents

1	Executive Summary	3
2	Science Case	5
2.1	The most powerful accelerators of our Universe	5
2.2	Multimessenger Astronomy	8
2.3	Explosive nucleosynthesis and chemical evolution of the Galaxy	14
3	Scientific Requirements	15
4	The Scientific Instrument	17
4.1	Measurement principle and payload overview	17
4.2	Performance assessment	25
4.3	Required resources	30
4.4	Specific interface requirements	31
4.5	Calibrations	32
4.6	Technology readiness and relevant heritage	33
5	Mission Configuration and Profile	34
5.1	Mission overview	34
5.2	Spacecraft overview	34
5.3	Operational orbit	35
5.4	Spacecraft preliminary design	36
5.5	Deployable boom	38
5.6	Technology readiness	40
5.7	System budgets	40
5.8	Ground segment	42
6	Management Scheme	43
6.1	Instrument development group	43
6.2	Product tree and Work Breakdown Structure	43
6.3	Procurement Scheme	45
6.4	Model philosophy and schedule	46
6.5	Technology development activity for the deployable boom	46
7	Costing	48

1 Executive Summary

In the era of multimessenger astronomy, recently opened by the discovery of simultaneous gravitational wave- γ ray and neutrino- γ ray signals, it is of paramount importance to have a monitor capable to detect energetic transients in the energy range from 0.1 MeV to a few hundred MeV, with imaging capabilities. Binding energies of nuclei fall in this energy range, which therefore is as important for high-energy astronomy as optical astronomy is for phenomena related to atomic physics; in addition, this region includes the electron and pion rest energies, which are appropriate to tag leptonic and hadronic processes occurring in astrophysical sources of electromagnetic radiation and cosmic particles.

To fill this gap we propose All-Sky-ASTROGAM, an instrument dedicated to fast detection, localization, and gamma-ray spectroscopy of flaring and merging activity of compact objects in the Universe, with excellent polarimetric capabilities. The instrument is a nearly 4π gamma-ray imager attached to a deployable boom (Fig. 1), capable of continuously observing every single gamma-ray source in the sky during 2 years, i.e. the entire mission lifetime. It is based on the ASTROGAM concept [28, 29, 79]: a telescope made of thin silicon tracking planes and a scintillation calorimeter to image the Compton interaction and the pair production by gamma rays. The main constituents of the All-Sky-ASTROGAM scientific payload are:

- A 3D-imaging Calorimeter to measure the energy of photons and electrons/positrons, made of an array of 784 CsI (Tl) bars of $1 \times 1 \times 5 \text{ cm}^3$ each, with relative energy resolution of 4.5% at 662 keV;
- Two Si Trackers, one on each side of the Calorimeter, in which cosmic gamma rays can undergo Compton scattering or pair conversion, based each on 25 planes of double-sided Si strip detectors, each plane with total area of about $(0.3 \times 0.3) \text{ m}^2$;
- An Anticoincidence system (AC), composed of a standard plastic scintillator shielding, to veto the charged particle background.

The photon energy range from 0.1 MeV to a few hundred MeV is also crucial in different sectors of astrophysics [29]. Many cosmic phenomena have their peak emissivity in this region; MeV energies are the typical emission energies consequent to the excitation of molecular clouds by Cosmic Rays. All-Sky-ASTROGAM will be nearly an order of magnitude more sensitive than the most sensitive imaging telescope in the MeV region up to now: COMPTEL onboard the *Compton Gamma Ray Observatory* was launched almost three decades ago, when the silicon tracking technology was not yet ready for space missions.

The mission data, inserted in a multiwavelength and multimessenger context, will allow addressing major topics of modern astrophysics, The observations in the X-ray and GeV–TeV energy ranges of relativistic jet and outflow sources (both in our Galaxy and in active galactic nuclei, AGNs) have shown that the MeV–GeV band holds the key to understanding the transition from the lower energy continuum to a spectral range shaped by very poorly understood particle acceleration processes. In this context, it is crucial to have data at energies around $m_\pi/2 \sim 70 \text{ MeV}$ to determine the composition (hadronic, leptonic, or lepto-hadronic) of the outflows and jets, which strongly influences the environment, polarimetric capability, and capability to perform nuclear spectroscopy. Such capabilities will allow identifying the physical acceleration processes in outflows and jets (e.g. diffusive shocks, magnetic field reconnection, plasma effects), that may lead to dramatically different particle energy distributions in the MeV–GeV region, and clarifying the role of the magnetic field in powering ultrarelativistic gamma-ray burst (GRB) jets.

MeV spectra will allow measuring cosmic-ray diffusion in interstellar clouds and their impact on gas dynamics and state; they will provide crucial diagnostics about the wind outflows and their feedback on the Galactic environment (e.g., *Fermi* bubbles, Cygnus cocoon).

The deep exposure of the Galactic plane region will determine how different isotopes are created in stars and distributed in the interstellar medium; it will also unveil the recent history of supernova explosions in the Milky Way. Furthermore, All-Sky-ASTROGAM can detect a few supernovae in the Milky Way and in nearby galaxies, thus addressing fundamental issues in the explosion mechanisms

of both core-collapse and thermonuclear supernovae. The gamma-ray data will provide a much better understanding of Type Ia supernovae and their evolution with look-back time and metallicity, which is a pre-requisite for their use as standard candles for precision cosmology.

In addition to addressing its core scientific goals, All-Sky-ASTROGAM will achieve many serendipitous discoveries (the unknown unknowns) through its very wide field of view (FoV).

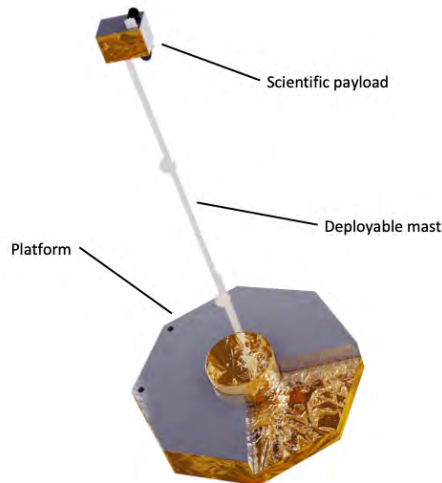


Figure 1: The All-Sky-ASTROGAM satellite.

All-Sky-ASTROGAM will operate in a maturing gravitational wave and multi-messenger epoch, opening up new and exciting synergies. The detector will have almost no occultation (Fig. 1), and will provide unique and complementary data of significant interest to a broad astronomical community, in a decade of powerful observatories such as LIGO-VIRGO-KAGRA-INDIGO, SKA, ALMA, E-ELT, LSST, JWST, Athena, CTA, IceCube. It will complement other observatories, being:

- a unique γ -ray monitor for astrophysical transients with large FoV (almost 4π sr) and optimal sensitivity to detect bright and intermediate flux sources (GRBs, AGN, Galactic) in the range 0.1 MeV - 500 MeV at different timescales (seconds, hours, days, weeks);
- a unique instrument for the New Astronomy of gravitational waves and neutrinos being able to detect prompt hard X-ray/gamma-ray emission from coalescing NS-NS and NS-BH binaries (with a capability of fast alerts to the community through GCN and IPN) and ν counterparts;
- a unique instrument to improve our knowledge of our Galaxy in an energy range crucial for studying nucleosynthesis and chemical evolution of the Milky Way.

All-Sky-ASTROGAM is complementary to ATHENA: (1) it will measure the particle background and characteristics in L2; (2) it will study AGN in the MeV range with the best sensitivity so far achieved.

The mission will act as an Observatory facility open to a wide astronomical community, with the customary ESA data policy.

All-Sky-ASTROGAM is proposed by a team largely overlapping with the core teams of AGILE and of the *Fermi* Large Area Telescope (LAT), which also used a technology based on silicon strip detectors. The proposing team can largely base the work of construction of the scientific payload on existing facilities; in particular three INFN laboratories are equipped with facilities able to test and mount silicon wafers for the trackers, and are already experienced thanks to the work done for AGILE, *Fermi* LAT, AMS-02 and, more recently, DAMPE. The number of Si wafers is less than 1/10 with respect to the M5 proposal e-ASTROGAM [28], and the number of crystals for the calorimeter is less than 1/30.

The core of the All-Sky-ASTROGAM team is EU-based; scientific and technical contributions from extra-EU countries (USA, Russia and Japan in particular) are envisaged.

2 Science Case

All-Sky-ASTROGAM (also called AS-ASTROGAM in the following) will open the MeV region for exploration, with an improvement close to one order of magnitude in sensitivity (Fig. 2) compared to the current state of the art, much of which was derived from the COMPTEL instrument more than two decades ago. All-Sky-ASTROGAM will also achieve an improvement in terms of source localization and energy resolution, and will allow to measure the contribution to the radiation of the Universe in an unknown range (Fig. 3). At higher energies, reaching almost one GeV, the sensitivity of All-Sky-ASTROGAM will reveal the transition from nuclear processes to those involving electro- and hydro-dynamical, magnetic and gravitational interactions.

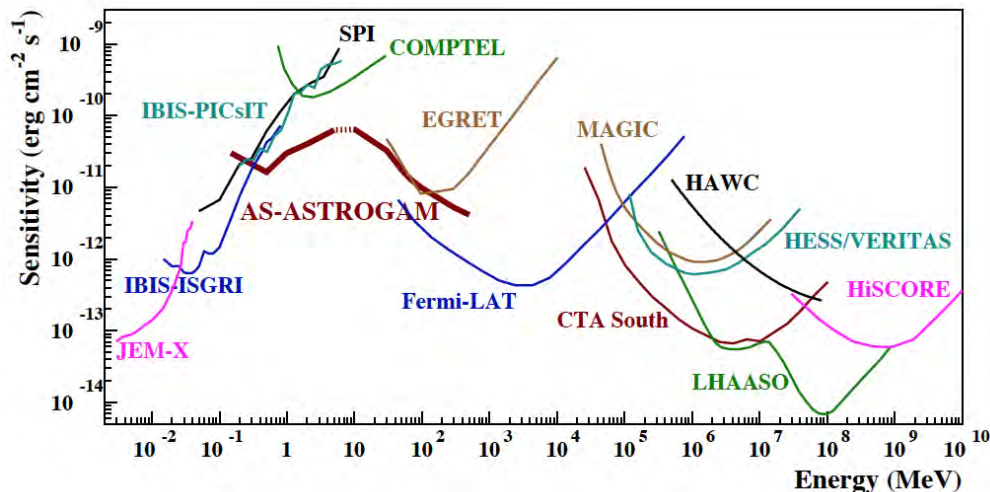


Figure 2: Point source continuum sensitivity of different X- and γ -ray instruments. The curves for INTEGRAL/JEM-X, IBIS (ISGRI and PICsIT), and SPI are for an observing time $T_{\text{obs}} = 1$ Ms. The COMPTEL and EGRET sensitivities are given for the observing time accumulated during the whole duration of the CGRO mission ($T_{\text{obs}} \sim 9$ years). The *Fermi*/LAT sensitivity is for a high Galactic latitude source and for a mission duration of 10 years. For MAGIC, VERITAS, and CTA, the sensitivities are given for $T_{\text{obs}} = 50$ hours. For HAWC $T_{\text{obs}} = 5$ yr, for LHAASO $T_{\text{obs}} = 1$ yr, and for HiSCORE $T_{\text{obs}} = 1000$ h. The All-Sky-ASTROGAM sensitivity is for an effective exposure of 1 year of a source at high Galactic latitude.

An important characteristic of All-Sky-ASTROGAM is its ability to measure polarization in the MeV range, which is mostly afforded by Compton interactions in the detector. Polarization encodes information about the geometry of magnetic fields and adds a new observational pillar, in addition to the temporal and spectral, through which fundamental processes governing the MeV emission can be determined. The addition of polarimetric information will be crucial for a variety of investigations, including accreting black holes (BH) systems, magnetic field structures in jets, and the emission mechanisms of GRBs. Polarization will provide definitive insight into the presence of hadrons in extragalactic jets and the origin of ultra-high-energy cosmic rays.

In the following sections, the core science questions addressed by All-Sky-ASTROGAM are presented. The requirements flowing from the scientific objectives, and driving the instrument design, will be presented in Section 3.

2.1 The most powerful accelerators of our Universe

Studying the spectral energy distribution (SED) of high energy emitters near compact objects is crucial to identify the processes in the central engine responsible for the highest energy photons.

The Universe accessible to All-Sky-ASTROGAM is dominated by strong particle acceleration. Ejection of plasma (jets or uncollimated outflows), ubiquitous in accreting systems, drives the transition from the keV energy range, typical of the accretion regime, to the GeV-TeV range,

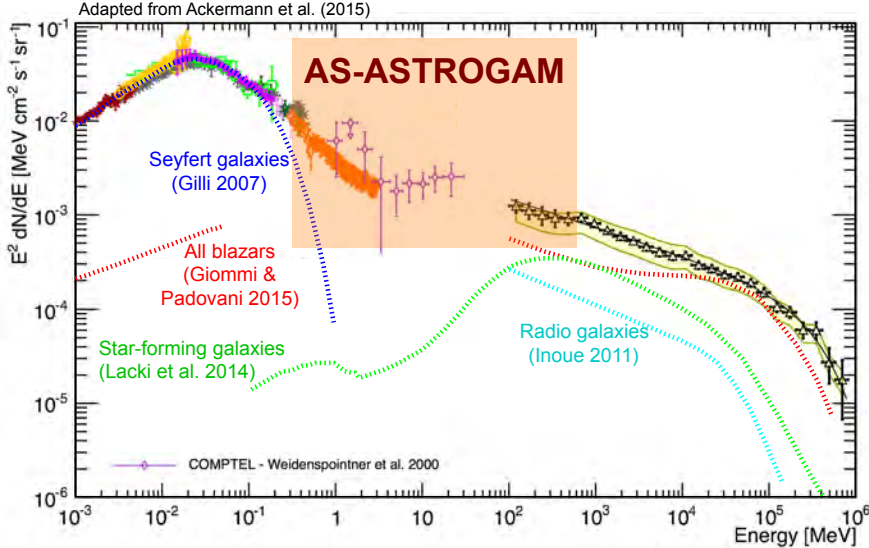


Figure 3: Compilation of the measurements of the total extragalactic gamma-ray intensity between 1 keV and 820 GeV [12], with different components from current models; the contribution from MeV blazars is largely unknown. The semi-transparent band indicates the energy region in which All-Sky-ASTROGAM will dramatically improve on present knowledge.

through reprocessing of synchrotron radiation (e.g. inverse Compton) or hadronic mechanisms. For some sources the MeV band naturally separates the acceleration and reprocessing energy ranges. Other systems radiate the bulk of their output in the MeV band.

In addition, MeV-band observations address the energy limit to which electrons may be accelerated, and the location where this acceleration happens.

While stationary SEDs of AGN can be modeled, some of the most intriguing variability features are still not understood. By studying the spectral response to changes in the activity of variable sources, we can distinguish the emission from electrons from that of energetic ions. Purely leptonic models predict simultaneous flux increases in the low energy and high energy peak, while lepto-hadronic models can accommodate more complex variability patterns depending on the dominant process responsible for the gamma-ray emission.

The transition to non-thermal processes involves, in particular, the emission of relativistic jets and winds. In our Galaxy, this transition is particularly relevant for compact binaries and micro-quasars.

The interplay between accretion processes and jet emission can best be studied in the MeV region, where disk Comptonization is expected to fade and other non-thermal components can originate from jet particles. All-Sky-ASTROGAM observations of Galactic compact objects and in particular of accreting BH systems (such as Cygnus X-1 [82], Cygnus X-3 ([78, 10]), V404 Cygni [69]) will determine the nature of the steady-state emission due to Comptonization and the transitions to highly non-thermal radiation (Fig. 4). The main processes behind this emission are Compton scattering by accelerated non-thermal electrons and its attenuation/reprocessing by electron-positron pair production. The magnetic field in the BH vicinity can be quite strong, and have both random and ordered components. Then, synchrotron emission by the non-thermal electrons in the accretion flow may give rise to polarized MeV emission (e.g. [67]), which can be effectively measured by All-Sky-ASTROGAM, together with spectral transitions. Signatures of electron-positron production and annihilation (e.g. [73]) can be definitely detected by All-Sky-ASTROGAM.

To draw conclusions on the mechanisms in the central engine of AGN not only the spectral but also the temporal coverage of All-Sky-ASTROGAM will be important.

All-Sky-ASTROGAM will be sensitive to flares like the ones displayed by 3C279 (Fig. 5), providing a key ingredient for monitoring and for the multiwavelength description of the SED.

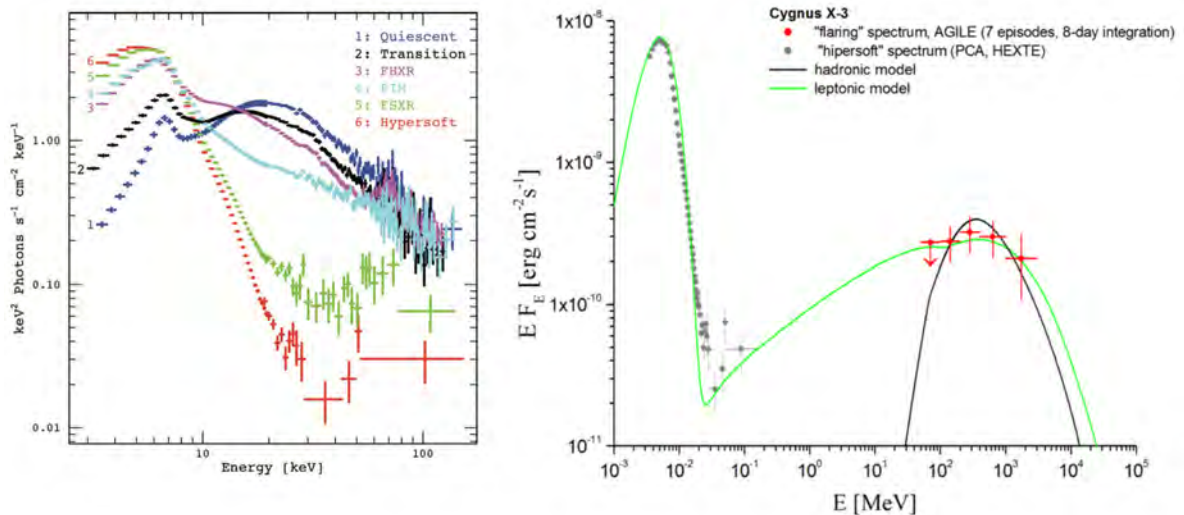


Figure 4: Left panel: Different spectral states of Cyg X-3 in the X-ray/hard X-ray ranges (adapted from [50]). Right panel: the SED of Cyg X-3 during the gamma-ray flaring activity in 2011 (adapted from [65]). The green curve refers to a leptonic model and the black curve to a hadronic model.

2.1.1 MeV-GeV astronomy and AGNs

The majority of the sources (2415 out of 3033) from the 3rd *Fermi*–LAT Catalog of GeV-band sources (3FGL), have power-law spectra (at energies larger than 100 MeV) steeper than E^{-2} , implying that their peak energy output is below 100 MeV (see an example in Fig. 6). The subset of extragalactic sources hosts BHs with masses reaching $10^{10} M_{\odot}$, and are often located at high redshift ($z \geq 2 - 3$). They are therefore ideal tracers of the formation and history of super-massive BHs in the Universe [38, 39]. In particular, the sources hosting the most massive BHs are elusive in the GeV band – as probed by the *Fermi* LAT.

Recent hard X-ray surveys ([15], [38], [16]) have been shown to be more effective in detecting higher redshift blazars compared to gamma-ray surveys, despite the sensitivity of the *Fermi* mission. The main reason is that the SEDs of these sources peak in the MeV region (hereafter, MeV blazars) and detection becomes a difficult task for gamma-ray instruments, even *Fermi*. All-Sky-ASTROGAM will detect hundreds of these blazars, constraining their SED peaks very tightly (Fig. 6). These discoveries will help our understanding of: (i) how the two populations of AGNs (radio-quiet and radio-loud) evolve with redshift; (ii) the formation and growth of supermassive BHs; (iii) the connection between the jet and the central engine and (iv) the role of the jet in the feedback occurring in the host galaxies [81]. All-Sky-ASTROGAM will very substantially advance our knowledge of MeV-blazars up to redshift ~ 3.5 , with implications for blazar physics and cosmology. These observations will be invaluable and complementary to ATHENA data for the study of super-massive black holes.

By detecting the population of MeV-blazars up to redshift ~ 3.5 , All-Sky-ASTROGAM will resolve the extragalactic gamma-ray background (EGB) in the MeV range (Fig. 3). In addition, the MeV band carries the cascade emission of all the absorbed Very-High-Energy (VHE) gamma-ray emission that is emitted in the universe, and so its study provides a unique view of its extreme particle acceleration history, including the feedback on the intergalactic medium and the generation of the magnetic field within.

2.1.2 GRBs and Polarization Measurements

All-Sky-ASTROGAM will be also an instrument studying GRBs in one of the most important energy regions. It will be able to detect ~ 100 GRBs per year and accurately measure the polarization properties of several tens of GRBs per year. This polarization signal information, combined with spectroscopy over a wide energy band, will provide unambiguous answers regarding the origin of the GRBs' highly relativistic jets and the mechanisms of energy dissipation and high-energy pho-

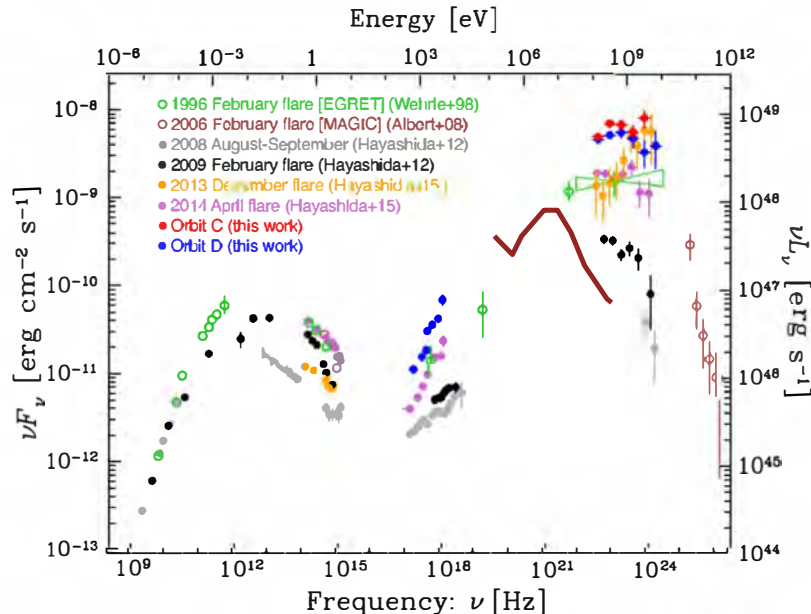


Figure 5: SED from different spectral states of the FSRQ 3C 279 showing a dramatic γ -ray flaring activity, including the minute-timescale episode detected by *Fermi* in June 2015. The solid line is the 3σ All-Sky-ASTROGAM sensitivity for a 50 ks exposure.

ton emission in these extreme astrophysical phenomena [77]. In addition, gamma-ray polarization measurement from cosmological sources provides a fundamental test of the vacuum birefringence effect and address major questions related to Lorentz Invariance Violation [29, 34].

Figure 7 shows an example of a simulated polarigramme in the 0.1 – 0.5 MeV range (i.e. in the Compton domain). The calculations were done for a gamma-ray burst like GRB 140206A detected at 30° off-axis, assuming the fluence and polarization properties measured by *INTEGRAL*/IBIS for this burst [34]. However, only a lower limit to the polarization fraction of 48% (at the 68% confidence level) could be derived from the *INTEGRAL* data, whereas All-Sky-ASTROGAM would be able to measure accurately both the polarization fraction and angle for such a burst.

Short GRBs deserve a special discussion, as we will see in the next subsection.

2.2 Multimessenger Astronomy

Multimessenger astronomy has been opened during the last years thanks to the detection of gravitational waves (GWs) from binary mergers and of a neutrino from the AGN TXS 0506 +056.

The MeV range is the perfect companion for multimessenger astronomy.

The MeV band is ideally suited for the inquiry of the acceleration mechanisms in AGN, because emission at higher gamma-ray energies may be absorbed, and the specific contribution from photo-pair-production by high-energy cosmic nuclei is a critical discriminant in the soft gamma-ray band, as an analysis of the recent detection of the association of a 300-TeV neutrino event with an extended gamma-ray flare in TXS0506+056 has shown [2].

On top of the SED of the EM emission by TXS0506+056 [2], the recent binary neutron-star (NS-NS) merger generating the GW event GW170817 and the corresponding gamma-ray signal detected by the *Fermi* GBM and *INTEGRAL* [7] have shown that the electromagnetic cutoff of this class of mergers is likely in the (tens of) MeV range.

2.2.1 Electromagnetic counterparts to gravitational wave transients

The long-standing quest for the observation of GWs simultaneously with gamma rays met with success when LIGO and Virgo detected GW170817, the first signal from the coalescence of two NS, 1.7

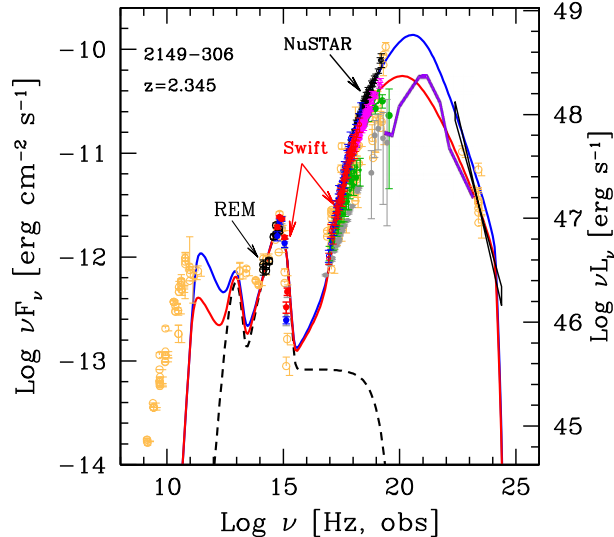


Figure 6: SED of PKS 2149-306 at $z = 2.345$ and the fitting model by [74]. The sensitivity of All-Sky-ASTROGAM is shown as a purple curve in the $0.3 \text{ MeV} - 0.9 \text{ GeV}$ range. The bulk of the power is expected in the MeV band, around $10^{20} \text{ Hz} - 10^{21} \text{ Hz}$.

s before the gamma-ray signal detected by the *Fermi* GBM and by *INTEGRAL*. Thanks to a dedicated follow-up campaign, EM counterparts to GW170817 were found in the visible, X-ray and radio bands. Also NS-BH mergers, not observed yet, are expected to have an associated EM emission. The energy cutoff for the gamma-ray counterparts on NS-NS (Fig. 10, left) and NS-BH mergers is expected to fall in the region of tens of MeV, well appropriate for All-Sky-ASTROGAM[29] – detections in this energy region thus provide an estimate of energetics independent of GW detectors.

These systems are expected to be the progenitors of short GRBs (see [22] for a review). Furthermore, NS-NS mergers are theoretically predicted to entail significant mass ejection which interacts with the surrounding medium on timescales of years, producing a remnant in which accelerated electrons can generate gamma ray emission [75]. The association between GW170817 and the GRB 170817A by *Fermi* GBM [7] supports the connection between NS-NS mergers and short GRBs. Joint GW and EM observations are key to obtain a more complete knowledge of the sources and their environments, since they provide complementary information. From one side, GW signals provide information about the physics of the source such as, e.g., the mass and the distance; on the other hand, the identification of the possible EM counterpart pinpoints the location of the burst, possibly identifying the host galaxy and properly defining the astrophysical context. The detection of the gamma ray counterpart with All-Sky-ASTROGAM will help to understand if also NS-BH systems are progenitors of short GRBs and to characterize the astrophysical properties of the source. These results will also improve our knowledge of the stellar population of our Galaxy, with a particular focus on the progenitor of merging binary systems.

The search for the EM counterpart to GW transient events is challenging for several reasons. First of all, the sky localization provided by the current ground-based interferometers is in order of tens to hundreds of square degrees (see, e.g., [6]), therefore large field-of-view (FoV) instruments are essential to properly cover the large GW error boxes. Furthermore, within these boxes, a huge number of EM transients is expected, making it difficult a clear and univocal identification of an EM counterpart to the GW event (e.g., the number of optical transients spatially and temporally coincident with GW events is expected to be of the order of hundreds, see e.g. [58]); this is somewhat mitigated at gamma ray energies, where the number of transient events is much smaller than at lower energies (for instance, the *Fermi* GBM transient catalog comprises only a few events in an area of 100 square degrees, see [45]). In the gamma ray domain, the favorite EM counterparts to NS-NS mergers are short GRBs, possibly accompanied by a thermal signal associated to the

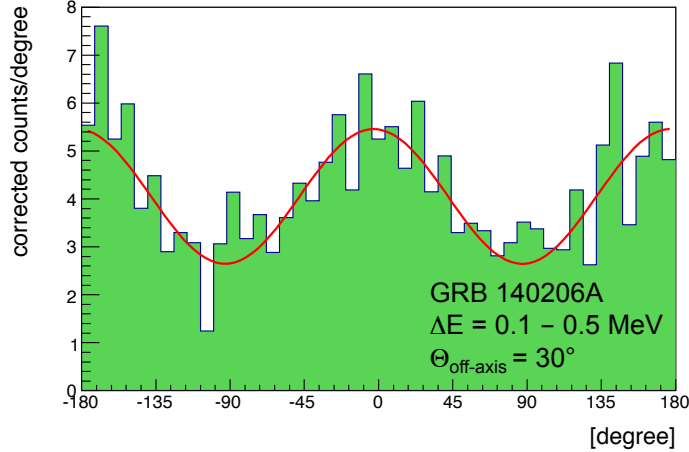


Figure 7: All-Sky-ASTROGAM polarization response in the 100–500 keV band to a GRB like GRB 140206A ($z = 2.739$, see [34]) detected at 30° off-axis, assuming a polarization fraction of 75%.

“kilonova” emission (see [20, 43]). The EM emission from short GRBs is believed to be beamed and the observed sources are typically the on-axis ones, i.e. the ones for which the angle between the line-of-sight and the jet axis is less than the jet opening angle. However, the majority of NS-NS merger events will correlate to off-axis short GRBs, as suggested by simple geometrical arguments based on the presumable small opening angle $\theta \sim 10^\circ$ of the jet [31]. Taking into consideration that the observed flux from on-axis GRBs is enhanced by beaming, off-axis GRBs flux is dramatically weaker and very sensitive gamma ray instruments are needed to reveal nearby off-axis GRBs associated to GW events.

From the observational point of view, the follow-up of GW170817 conducted in optical, IR and UV revealed the presence of an EM counterpart with emission consistent with a kilonova, while X-ray and radio data are interpreted as due to an off-axis afterglow emission [9].

Polarization is expected if the jet launching is driven by magnetic energy and depending on the magnetic field configuration. Off-axis observations can introduce an anisotropy that enhances the degree of polarization [37, 41]. In case a high-energy MeV-GeV component is observed, polarization can help to discriminate between different emission processes such as Inverse-Compton (IC) emission of leptons (no polarization) and synchrotron polarized emission from hadrons. Measurement of the gamma ray polarization in GW triggered events could provide a new tool for the interpretation of the GW/EM emission. When Advanced LIGO and Advanced Virgo will operate at design sensitivity, the expected range for the detection will be ~ 200 Mpc for NS-NS mergers and ~ 1 Gpc for BH-NS systems [6].

All-Sky-ASTROGAM will be able to detect also off-axis sources and will have negligible occultation and no significant off time, at variance with respect to satellites in LEO, with the consequent sizeable increase in the detection rates. All-Sky-ASTROGAM will also be able to detect events like GRB170817. This GRB is characterized by an isotropic peak luminosity $L=1.6 \cdot 10^{47}$ erg/s, a luminosity distance 40 Mpc and its spectrum is well described by an exponentially cut-off power law (see [8, 40]; the expected flux in the 0.2-2 MeV energy range for such an event is ~ 0.8 ph cm $^{-2}$ s $^{-1}$, that is above the All-Sky-ASTROGAM sensitivity.

Figure 8 illustrates the superior sensitivity of All-Sky-ASTROGAM (compared to *INTEGRAL*) to detect the continuum emission expected from the kilonova following a merger event like GW170817. Kilonovae are thought to be primarily powered by the radioactive decay of r-process nuclei synthesized in the merger outflows, and All-Sky-ASTROGAM could detect the predicted gamma-ray emission [43] up to a maximum distance of $\sim 5 - 6$ Mpc.

Simulations of the large GRB database yield detection rates of about 25 short GRBs and 75 long GRBs per year in the “Gamma-ray imager” trigger mode of All-Sky-ASTROGAM, and these events will be localized within ~ 2 square degrees to initiate observations at other wavelengths. Additional,

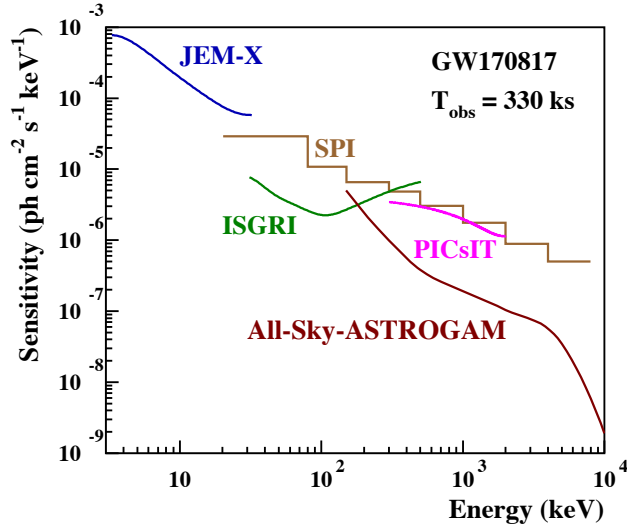


Figure 8: Continuum sensitivity reached in the *INTEGRAL* targeted follow-up observation of GW170817, compared to the corresponding sensitivities of All-Sky-ASTROGAM. All sensitivities are shown for a total exposure of 330 ks. Adapted from Fig. 5 of Ref. [71].

softer bursts will be detected by the “Calorimeter burst search” mode of data acquisition (i.e. using triggers generated only by an increase of the Calorimeter count rate). The trigger threshold in this mode is $\sim 0.3 \text{ ph cm}^{-2} \text{ s}^{-1}$ in the 100–300 keV energy range over 1 s timescale, which is significantly lower than the measured flux in the main pulse ($\Delta t = 0.576 \text{ s}$) of GRB 170817A, $F_\gamma(100\text{--}300 \text{ keV}) = 0.49 \text{ ph cm}^{-2} \text{ s}^{-1}$ [7]. Finally, GRB170817A is likely to have been observed at an angle $\sim 30^\circ$ from the jet axis (see also [49]). The on-axis energy should be larger by a factor of 20 to 30 [80], allowing All-Sky-ASTROGAM to track Compton events (Fig. 9).

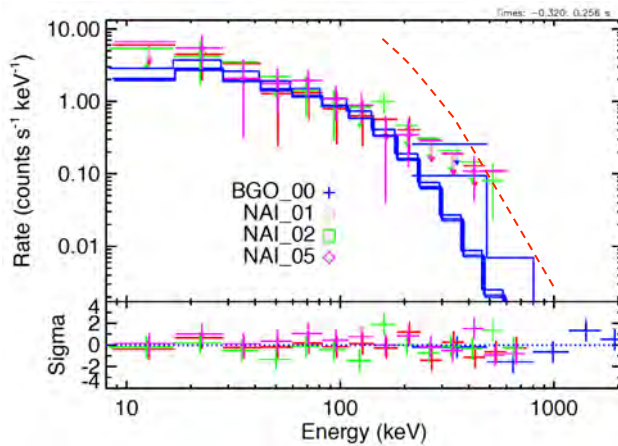


Figure 9: The flux from the hard component of GRB170817A as recorded from *Fermi* GBM (solid blue line), and a conservative extrapolation (20x) to an on-axis flux (dashed red line).

The detection of the gamma ray counterpart with All-Sky-ASTROGAM will help to understand if and which binary systems are progenitors of short GRBs and to characterize the astrophysical properties of the source. Simultaneous GW/EM emission will transform our understanding of the formation, evolution, properties and environment of different mass compact objects through cosmic history.

Polarization is expected if the jet launching is driven by magnetic energy and depending on the magnetic field configuration; such a polarization is enhanced for off-axis emission. All-Sky-ASTROGAM will also allow to measure the polarization of the brightest events with the highest

fluence, typically of the order of $10^{-4} - 10^{-5}$ erg/cm² down to the level of 10-20%. The possible detection of polarization from GRB associated to GW events with All-Sky-ASTROGAM shall have a tremendous impact on the interpretation of the formation of the jet and radiation mechanisms.

The simulation of All-Sky-ASTROGAM predicts that a number between 0.2 and 6 NS-NS mergers per year will be detected within 30 degrees (see, e.g., [61]) of the jet axis in coincidence with a GW detection, after the incorporation of KAGRA and INDIGO in the GW network. Such an estimate is conservative, since the detection of a short GRB with the characteristics of a kilonova will enhance the sensitivity of GW experiments by increasing the confidence in detections below the significance threshold, and provide small temporal and positional windows for targeted *a-posteriori* searches of GW data. All-Sky-ASTROGAM will also play a key role in the multiwavelength study of GW events: in fact, its large FoV will maximize the detection probability and provide accurate sky localization (< 1 square degree at 1 MeV), thus allowing the follow-up of the GW events by other telescopes. This capability will be crucial for the identification and the multiwavelength characterization of the GW progenitor and of its host galaxy.

Localizations will also guide wide-field follow-up observers in afterglow detection and redshift measurement, and allow long-baseline observations.

2.2.2 Synergies with neutrino telescopes

Neutrinos are unique probes to study high-energy cosmic sources. Contrary to cosmic rays (CRs), they are not deflected by the magnetic fields and unlike high-energy photons, they are not absorbed by pair production via $\gamma\gamma$ interactions. Astrophysical high-energy neutrinos at TeV–PeV energies are generated by the decay of charged pions produced in inelastic photo-hadronic ($p\gamma$) or hadronuclear (pp) processes, involving protons ~ 20 times more energetic than the resulting neutrinos. A simultaneous emission of hadronic gamma rays is also expected from both processes. An approximate relation holds *at emission* between the spectral production rates of neutrinos and gamma rays in hadronic production:

$$E_\nu^2 \frac{dN_\nu(E_\nu)}{dE_\nu} \sim \frac{3K}{4} E_\gamma^2 \frac{dN_\gamma(E_\gamma)}{dE_\gamma}$$

with $K = 1/2(2)$ for the γp (pp) process. Depending on the source optical depth, such photons may escape or further cascade, complicating time and energy correlation between neutrinos and EM counterparts [30].

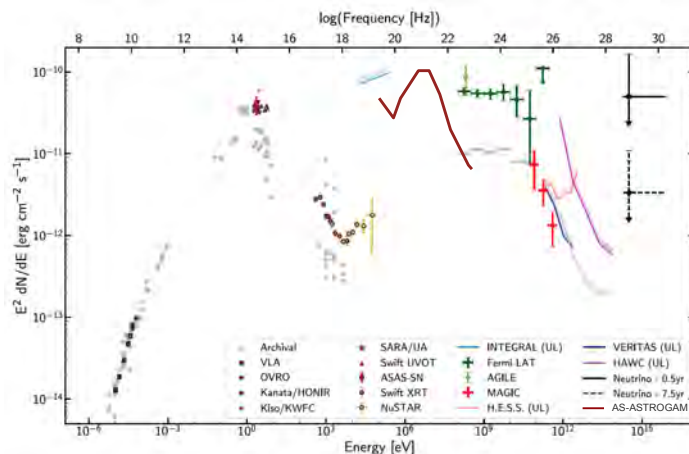


Figure 10: SED of the blazar TXS 0506+056. Dark points are data taken during the flare; grey points correspond to non-flaring states. The All-Sky-ASTROGAM sensitivity (solid brown) is calculated for an effective exposure of 7 days, corresponding to the observations by *Fermi* LAT and MAGIC during the flare.

A diffuse flux of cosmic neutrinos has been detected by IceCube [1], the sources of which are still unknown. Identifying those sources and their association with EM counterparts would provide unique insights into the long-standing problem of the origin of CRs [70]. Many astrophysical source classes have been suggested as responsible for the IceCube signal, like star-forming and/or star-burst galaxies, GRBs, or AGN. Galactic sources like microquasars are also expected to be emitters of astrophysical neutrinos. For a review on neutrino source candidates and multimessenger connections see e.g. [14].

In conventional GRBs, the neutrino emission is expected to be in temporal coincidence with the prompt gamma ray emission. Recent results from IceCube [4] disfavor them as the sources of the highest energy CRs and neutrinos. Such conclusions however would not apply if the central engine is surrounded by a dense material envelope, like the shocked jets proposed in [72]. For AGN, predicted fluxes strongly vary with the assumed emission mechanisms. A recent IceCube analysis [5] suggests that blazars contribute at most 27% of the observed IceCube intensity.

Neutrinos could be emitted during flaring events, making simultaneous observation of neutrino and gamma ray signals mandatory to probe this scenario. The first compelling evidence was recorded on September 2017, when the *Fermi* LAT and MAGIC observed enhanced gamma ray emission from a blazar positionally consistent with the neutrino IC170922A [35, 76, 55], and one year later published [2, 3, 18]. On September 22, 2017, IceCube detected a muon coming from the bottom of the detector through the Earth, produced by a neutrino of energy of $E_\nu \sim 300$ TeV. Promptly alerted, the *Fermi* LAT and MAGIC detected at more than 5σ a flare from the blazar TXS 0506 +056, at a redshift ~ 0.34 [60], within the region of sky consistent with the 50% probability region of the IceCube neutrino (about one degree in size). The MAGIC detection allowed to determine that the electromagnetic emission had a cutoff at ~ 400 GeV. The simultaneous emission of gamma rays and neutrinos from the same source proves that the “hadronic mechanism” has been seen at work. The estimated energy of a proton producing such a high energy neutrino in a “beam dump” is:

$$E_p \gtrsim 20 E_\nu \sim 10 - 20 \text{ PeV}$$

an energy above the knee and well appropriate for a blazar. This event opened the era of multimessenger astronomy with neutrinos; upgrades of neutrino detectors are expected in the next years, and these events will become common.

One of the main challenges in neutrino astronomy is the detection of excesses of events due to astrophysical sources among background signals. The ANTARES and IceCube neutrino telescopes operate extensive programs of real-time multi-wavelength follow-up, enabling the search for an EM counterpart of astrophysical neutrino candidates by generating alerts whenever an interesting neutrino event is detected (namely a significant multiplet of events, an energetic event or an event whose direction is compatible with a local galaxy). Broad-band data, from the radio domain to the VHE gamma ray regime, are requested as Target-of-Opportunity (ToO) observations to the partners. In particular, high-energy observations from the X-ray (keV) to the gamma ray (MeV-GeV) domains are among the most decisive if they are performed simultaneously or shortly after the neutrino trigger, since they allow for the detection of transient cataclysmic events which might involve hadronic processes. Conversely, selecting only neutrino events coincident with the EM flare allows for a much better background rejection, and thus a better sensitivity. Such studies generally assume a correlation between X-ray/gamma ray flares and neutrino emission, and thus require light curves measured by X-ray/gamma ray instruments as an input, with the largest possible time coverage. Just one source of cosmic neutrinos has been found [2], but it yielded already important model constraints (see e.g. [4, 17]).

A next generation of neutrino telescopes is coming. In the Northern hemisphere, KM3NeT will succeed ANTARES in the coming years and will greatly improve both the sensitivity to neutrino point-sources and the angular resolution ($\sim 0.2^\circ$ for muon track events and $\sim 1.5^\circ$ for showers). In parallel, the upgraded IceCube and IceCube-Gen2 will increase the performance of the current detector by one order of magnitude with the deployment of 120 new detection lines by the next decade. Such upgrades will enable significant improvement on the EM follow-up activities and will benefit from the multi-wavelength facilities operating at the same time.

All-Sky-ASTROGAM can play a decisive role in this scenario. In Fig. 10, the sensitivity of All-Sky-ASTROGAM in 7 days (the time in which MAGIC observed an enhanced signal associated to the blazar TXS 0506+056) is compared to the SED of TXS 0506+056 [2]. Simultaneous time-resolved multi-wavelength information of variable objects at a daily-timescale (as TXS 0506+056) is fundamental for pinpointing the emission mechanism but is currently not feasible with *Fermi*. All-Sky-ASTROGAM will have a higher sensitivity than *Fermi* LAT over the overlapping energy range. This would have allowed to resolve the state of the source associated to the IceCube neutrino IC170922A. All-Sky-ASTROGAM would have covered an energy range not yet dominated by IC electron emission. There, it can be expected to be easier to single out hadronic components and constrain the efficiency as neutrino source. Its large field-of-view (FoV) will maximize the detection probability and provide an accurate sky localization. Those follow-up abilities will be important to test a potential association between high-energy neutrino candidates and various classes of transient astrophysical events, and will continue the programs currently performed with the *Swift* and *Fermi* satellites.

Furthermore, thanks to its wide FoV, All-Sky-ASTROGAM will detect and follow variable point-like sources (microquasars, AGN, etc). It has been recently claimed that the gamma ray transparency of astrophysical sources of neutrinos and gamma rays coming from photoproduction of pions might be severely reduced [57]. This result consequently suggests a population of cosmic-ray accelerators invisible in GeV–TeV gamma rays but bright in the MeV domain (see e.g. [72]). All-Sky-ASTROGAM will provide a good sampling of their MeV light curves that will be used to search for neutrino counterparts.

More specifically, the typical double-humped SED of blazars peaks at MeV energy and can be explained by both hadronic and leptonic processes. In photo-hadronic models, the neutrino flux F_ν can be related to the bolometric high-energy EM flux F_γ (integrated from 1 keV to 5 GeV) with $F_\nu \approx F_\gamma$ [51], which makes the MeV photon flux a good proxy of the neutrino emission from blazars. Thanks to its high sensitivity in the MeV domain, All-Sky-ASTROGAM will be perfectly suited to select the best blazar candidates for a neutrino emission and will help to interpret the neutrino observations. In addition, its unique polarimetric capability will enable to reveal the structure of the magnetic field and test the presence of hadrons in relativistic jets. All-Sky-ASTROGAM should also observe ~ 600 GRBs during the first three years of its mission. Its sub-millisecond trigger and alert capabilities will enable to look for neutrino counterparts of GRBs in nearly real-time and will then take over from *Swift*, *INTEGRAL* and *Fermi* instruments.

Finally, one of the yet unanswered questions is the nature of the process generating the observed cosmic neutrinos ($p\gamma$ or pp processes). If IceCube neutrinos are mainly produced by pp interactions, their sources should significantly contribute to the IGRB and their flux should be consistent with the total flux. Recent studies (see e.g. [21]) show that pp models are in tension with the IGRB, disfavoring the pp origin of the cosmic neutrino flux observed by IceCube. Further understanding the contribution of different source populations to the IGRB is therefore crucial. Measurement of spectral features in the 10 – 200 MeV range with All-Sky-ASTROGAM will help to constrain the population models of the IGRB and will consequently have an important impact on the interpretation of the multimessenger connection between gamma rays and neutrinos.

2.3 Explosive nucleosynthesis and chemical evolution of the Galaxy

Exploding stars play a very important role in astrophysics since they inject important amounts of kinetic energy and newly synthesized chemical elements into the interstellar medium in such a way that they completely shape the chemical evolution of galaxies. Furthermore, the “pyrotechnical” effects associated with such outbursts can be so bright and regular that they can be used to measure distances at the cosmological scale. For instance, Type Ia supernovae (SNIa) allowed the discovery that the Universe was expanding in an accelerated way.

The majority of the outbursts are associated with instabilities of electron degenerate structures in single stars (core collapse and electron capture supernovae) or when they accrete matter from a companion in a close binary system (SNIa and classical novae, for instance). Systematic research on

transient events have revealed a surprising variety of outbursts that goes from “Ca-rich” transients, placed in the gap between Type Ia supernovae and novae, Type Iax, “02es-like” SNe, “super-Chandrasekhar” SNe in the domain of the so-called thermonuclear supernovae, to, e.g., Type II_n, Type In, and so-called “impostors” in the domain of core collapse of massive stars.

Many of these events, if not all, imply the activation of thermonuclear burning shells that synthesize new isotopes, some of them radioactive. As the ejecta expand, more and more photons avoid thermalization and escape, such that they can be used as a diagnostic tool. Each one of the different explosion scenarios leads to differences in the intrinsic properties of the ejecta, like the density and velocity profiles, and the nature and distribution of the radioactive material synthesized. This translates into differences in the light curves and line widths of the expected γ -ray emission. Therefore, the observation with γ -rays becomes a privileged diagnostic tool with respect to other measurements thanks to the penetration power of high energy photons and the association of γ -lines to specific isotopes created by the explosion. All-Sky-ASTROGAM has a sensitivity and energy resolution fully appropriate for nuclear astrophysics.

- With a gain in sensitivity for the ^{56}Co line at 847 keV by a factor of about six compared to *INTEGRAL*/SPI, All-Sky-ASTROGAM has a very high probability to detect at least one **Type Ia SN** in two years of nominal mission lifetime, thus allowing a direct measurement of the total mass of $^{56}\text{Ni}/^{56}\text{Co}$ ejected by the explosion. This value is fundamental to calibrate the Phillips [64] relation used in cosmology and the yield of synthesized Fe. Furthermore, with its all-sky coverage, All-Sky-ASTROGAM will be able to detect the early γ -ray emission before the maximum optical light, which is fundamental to understanding the nature of the progenitor and the explosion mechanism.
- Continuous monitoring of the gamma-ray sky will also be essential to detect the early positron-electron annihilation emission expected before the optical maximum in **classical novae**, with positrons coming from the short-lived isotopes ^{13}N and ^{18}F . Gamma-rays are also produced in novae through particle acceleration, in strong shocks between the ejecta and the surrounding medium - in recurrent symbiotic novae - and internal shocks in the ejecta itself - in classical novae. By the early detection of the high-energy gamma-rays originated by neutral pions decay (hadronic origin) and IC scattering (leptonic origin) [11], All-Sky-ASTROGAM will give unique insights on the particle acceleration and mass ejection processes in novae.
- The observation of the radioactive emission from the $^{44}\text{Ti}/^{44}\text{Sc}$ chain can shed light on the clumping degree of remnants of **core-collapse SNe** (CCSNe) as a diagnostic of internal asymmetries produced in the explosion. The sensitivity of All-Sky-ASTROGAM will allow the detection of this emission in most young Galactic SNRs and in the remnant of SN1987A. The determination of the amount of ejected ^{56}Ni would also be very important to understand the physics of the explosion.
- All-Sky-ASTROGAM’s continuous imaging of the whole sky will provide a detailed mapping of the **positron annihilation radiation** from the inner Galaxy and the diffuse gamma-ray emission from the **long-lived radioactivities** ^{26}Al and ^{60}Fe . Building precise maps of these Galactic emissions will shed new light on nucleosynthesis in massive stars, supernovae and novae, as well as on the structure and dynamics of the Galaxy.

3 Scientific Requirements

All-Sky-ASTROGAM’s requirements, such as the angular and energy resolution, the field of view, the effective area and continuum sensitivity, the line sensitivity, and polarization sensitivity, to achieve its core science objectives are summarized in Table 1.

The requirements reflect the dual capacity of the instrument to detect both Compton scattering events in the 0.1 – 10 MeV range and pair-producing events in the 10 MeV - 1 GeV energy range. The main instrument features of All-Sky-ASTROGAM necessary to meet the scientific requirements in Table 1, are described in Sect. 4.2.

Table 1: All-Sky-ASTROGAM scientific requirements.

Parameter	Value
Energy bands:	100 keV – 1 GeV (Gamma-ray imager: Tracker + Calorimeter) 30 keV – 200 MeV (Calorimeter burst search)
Gamma-ray imager total FOV	$> 3\pi$ sr
Gamma-ray imager Continuum flux sensitivity at 3σ confidence level	$< 1.5 \times 10^{-4}$ MeV cm ⁻² s ⁻¹ at 1 MeV ($T_{\text{obs}} = 10^6$ s effective observation time) $< 1.5 \times 10^{-4}$ MeV cm ⁻² s ⁻¹ at 10 MeV ($T_{\text{obs}} = 10^6$ s, high-latitude source) $< 2.5 \times 10^{-5}$ MeV cm ⁻² s ⁻¹ at 100 MeV ($T_{\text{obs}} = 10^6$ s, high-latitude source)
Gamma-ray imager Line flux sensitivity at 3σ confidence level	$< 5 \times 10^{-5}$ ph cm ⁻² s ⁻¹ for the 511 keV line ($T_{\text{obs}} = 10^6$ s effective obs. time) $< 5 \times 10^{-5}$ ph cm ⁻² s ⁻¹ for the 847 keV SN Ia line ($T_{\text{obs}} = 10^6$ s) $< 5 \times 10^{-5}$ ph cm ⁻² s ⁻¹ for the 1157 keV line from CCSNe ($T_{\text{obs}} = 10^6$ s)
Gamma-ray imager angular resolution	$\leq 1.6^\circ$ at 1 MeV (FWHM of the angular resolution measure) $\leq 1.5^\circ$ at 100 MeV (68% containment radius) $\leq 0.3^\circ$ at 1 GeV (68% containment radius)
AC particle background rejection efficiency	$> 99.99\%$
Polarization sensitivity	MDP $< 3\%$ (3σ c.l.) for a Crab-like source in $T_{\text{obs}} = 10^6$ s (0.2-2 MeV) Detection of a polarization fract. $\geq 25\%$ in more than 10 GRBs per year
$\Delta E/E$ (Gamma-ray imager)	3.0% at 1 MeV 30% at 100 MeV
$\Delta E/E$ (Calorimeter burst)	$< 25\%$ FWHM at 0.3 MeV $< 10\%$ FWHM at 1 MeV $< 5\%$ FWHM at 10 MeV
Time tagging accuracy	1 microsecond (at 3 sigma)
Impulsive event acquisition logic (Calorimeter burst)	sub-millisecond trigger and photon-by-photon acquisition capability
Orbit	quasi-periodic orbit around the Sun-Earth L2 Lagrange point
Average scientific telemetry	> 350 kbps (after data compression)
Satellite attitude reconstruction	1' (at 3 sigma)
Satellite pointing modes	1. survey mode (spinning); 2. pointing mode (depending on the source visibility in the FOR).
Target of Opportunity observations	within 24-48 hours from alert
Mission duration	2 years

The wide field-of-view requirement is consistent with the L2 orbit imposed by the dual launch with the ARIEL mission. Attached to a 6 m-long boom, the gamma-ray instrument will have almost no occultation and will be able to continuously monitor every single gamma-ray source in the sky during the entire mission lifetime.

Table 1 also includes the most important system requirements such as the satellite attitude reconstruction, telemetry budget, and pointing capability. All-Sky-ASTROGAM is a multi-purpose astrophysics mission with the capability of a flexible observation strategy. However, the main scientific observation mode is the survey mode, where the spacecraft maintains a slow rotation around the boom axis while keeping the fixed solar array panels properly oriented toward the Sun. The pointing mode will be implemented as a fixed inertial pointing.

Requirements for the Ground Segment are standard for an observatory-class mission. Target of Opportunity observations (ToOs) are required to follow particularly important transient events that need a satellite pointing depending on the source visibility in the field of regard. The All-Sky-ASTROGAM mission requirement for ToO execution is within 1–2 days.

4 The Scientific Instrument

4.1 Measurement principle and payload overview

Interactions of photons with matter in the All-Sky-ASTROGAM energy range is dominated by Compton scattering from 100 keV up to about 15 MeV in silicon, and by electron-positron pair production in the field of a target nucleus at higher energies. All-Sky-ASTROGAM maximizes its efficiency for imaging and spectroscopy of energetic gamma-rays by using both processes. Figure 11 shows representative topologies for Compton and pair events.

For Compton events, point interactions of the gamma-ray in the Tracker and Calorimeter produce spatially resolved energy deposits, which have to be reconstructed in sequence using the redundant kinematic information from multiple interactions. Once the sequence is established, two sets of information are used for imaging: the total energy and the energy deposit in the first interaction measure the first Compton scatter angle. The combination with the direction of the scattered photon from the vertices of the first and second interactions generates a ring on the sky containing the source direction. Multiple photons from the same source enable a full deconvolution of the image, using probabilistic techniques. For energetic Compton scatters (above ~ 1 MeV), measurement of the track of the scattered electron becomes possible, resulting in a reduction of the event ring to an arc, hence further improving event reconstruction. Compton scattering angles depend on polarization of the incoming photon, hence careful statistical analysis of the photons for a strong (e.g., transient) source yields a measurement of the degree of polarization of its high-energy emission (e.g. [32]).

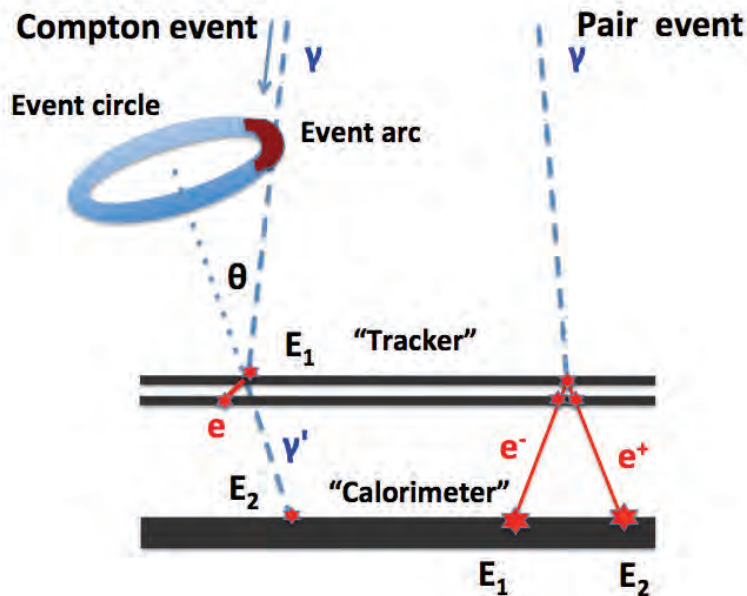


Figure 11: Representative topologies for a Compton event and for a pair event. Photon tracks are shown in pale blue, dashed, and electron and/or positron tracks are in red, solid.

Pair events produce two main tracks from the created electron and positron. Tracking of the initial opening angle and of the plane spanned by the electron and positron tracks enables direct back-projection of the source position. Multiple scattering of the pair in the tracker material (or any intervening passive materials) leads to broadening of the tracks and limits the angular resolution. The nuclear recoil taking up an unmeasured momentum results in an additional small uncertainty. The energy of the gamma-ray is measured using the Calorimeter and information on the electron and positron multiple scattering in the Tracker. Polarization information in the pair domain is given by the azimuthal orientation of the electron-positron plane.

The gamma-ray instrument of All-Sky-ASTROGAM is shown in Figure 12. It will be attached to a six meters-long deployable boom, which will be deployed when the spacecraft reaches its operational orbit, to reduce the gamma-ray shadow cast by the satellite platform on the telescope and decrease the instrument background induced by cosmic-ray interactions with the platform materials. The gamma-ray imager consists of three main detectors:

- A **silicon Tracker** in which the cosmic gamma-rays undergo a first Compton scattering or a pair conversion; it is based on the technology of double sided Si strip detectors to measure the energy and the 3D position of each interaction with an excellent energy and spatial resolution;
- A 3D-imaging **Calorimeter** to absorb and measure the energy of the secondary particles; it is made of an array of small scintillation crystals (784 CsI (Tl) bars of $10 \times 10 \times 50 \text{ mm}^3$) read out by silicon drift photodetectors to achieve the required energy resolution (4.5% at 662 keV);
- An **Anticoincidence** (AC) system covering the six faces of the instrument to veto the prompt-reaction background (as opposed to the delayed background due to the instrument material activation) induced by charged cosmic-ray particles; it is designed with plastic scintillator tiles covering the instrument to detect charged relativistic particles with an efficiency exceeding 99.99%.

The Calorimeter is placed in the middle of the instrument (Fig. 12) to allow the detection of gamma-rays from almost any direction in the sky (see Sect. 4.2.3).

The payload is completed by a Payload Data Handling Unit (PDHU) and a Power Supply Unit (PSU) located inside the satellite platform together with the back-end electronics (BEE). The PDHU is in charge of the payload internal control, the scientific data processing, the operative mode management, the on-board time management, and the telemetry and telecommand management. The total mass and power budget of the gamma-ray imager (including maturity margins) are 77.5 kg and 140 W, respectively (see Tables 5 and 6).

Especially for the Compton mode at low energies, but also more broadly over the entire energy range covered by All-Sky-ASTROGAM, it is important to keep the amount of passive materials in the detector to a minimum, to reduce background production in the field of view and optimize angular and energy resolutions. In addition, the passive materials between the Tracker layers, and between the Tracker and the Calorimeter must be minimized for best performance.

4.1.1 Silicon Tracker

The Tracker is the heart of the All-Sky-ASTROGAM payload. It is based on the silicon strip detector technology widely employed in medical imaging and particle physics experiments (e.g. ATLAS and CMS at LHC), and already applied to the detection of gamma-rays in space with the AGILE and *Fermi* missions. The All-Sky-ASTROGAM Tracker needs double sided strip detectors (DSSDs) to work also as a Compton telescope.

The essential characteristics of the All-Sky-ASTROGAM Tracker are:

- its light mechanical structure minimizing the amount of passive material within the detection volume to enable the tracking of low-energy Compton electrons and electron-positron pairs,

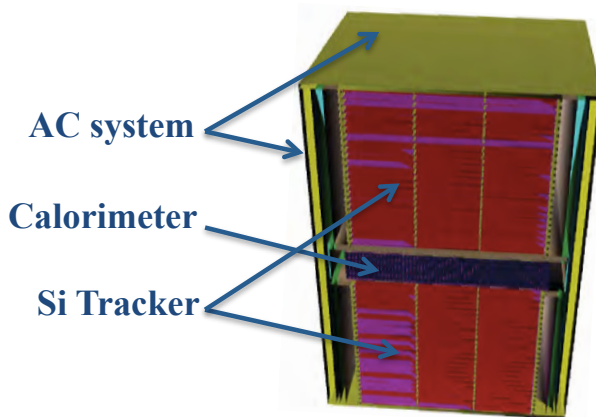


Figure 12: Overview of the All-Sky-ASTROGAM gamma-ray imager showing the silicon Tracker, the Calorimeter and the Anticoincidence system.

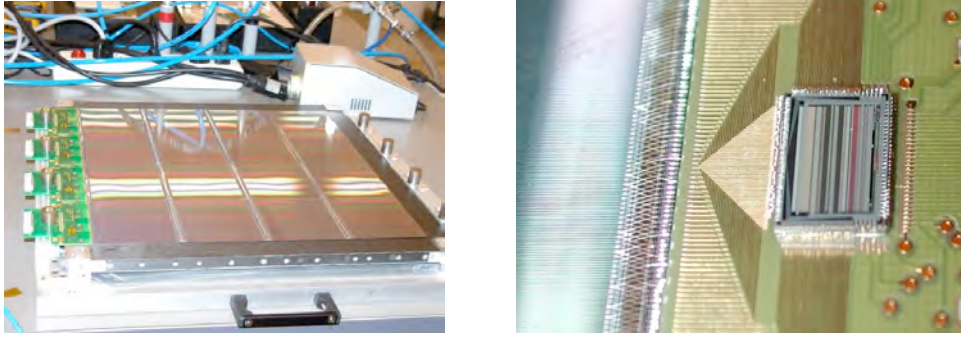


Figure 13: *Left Panel* - Silicon microstrip detectors of the type to be used in the All-Sky-ASTROGAM Tracker arranged in ladders of four bonded tiles placed on a tray during the AIV of the AGILE Tracker using test electronic boards. *Right panel* - Detail of the AGILE Tracker showing the Si sensor bonding with the FEE ASIC through a pitch adaptor.

and improve the point spread function in both the Compton and pair domains by reducing the effect of multiple Coulomb scattering;

- its fine spatial resolution of less than $40 \mu\text{m}$ ($< 1/6$ of the microstrip pitch) obtained by analog readout of the signals (as in the AGILE Tracker);
- its charge readout with an excellent spectral resolution of $\sim 4 \text{ keV}$ FWHM obtained with an ultra low-noise FEE, in order to accurately measure low-energy deposits produced by Compton events; the energy threshold is 10 keV.

The Si Tracker comprises 450 DSSDs arranged in 2×25 layers of 3×3 daisy-chained detectors. Such a stacking of relatively thin detectors enables an efficient tracking of the electrons and positrons produced by pair conversion, and of the recoil electrons produced by Compton scattering. The DSSD signals are readout by 115,200 independent, low-power electronics channels with self-triggering capability.

Silicon detectors The active element is a Si DSSD of $500 \mu\text{m}$ thickness and $9.5 \times 9.5 \text{ cm}^2$ area, with electrodes of $100 \mu\text{m}$ width, and $240 \mu\text{m}$ pitch (corresponding to 384 microstrips per side), a guard ring of 1.5 mm, and polysilicon resistors for the bias. It can be manufactured from high resistivity ($R \geq 5 \text{ k}\Omega \text{ cm}$) 6" substrate by, e.g., the Silicon Radiation Sensors[©] group of the Fondazione Bruno Kessler FBK (SRS-FBK) or Hamamatsu Photonics[©].

The electrical behavior of the All-Sky-ASTROGAM DSSDs was simulated with the SILVACO TCAD semiconductor toolkit in order to specify the requirements for the FEE and the thermal control. At full depletion voltage, the total capacitance on the p-side is found to be 13.0 pF/strip and the p-side leakage current amounts to about 150 pA/strip at $T = 0^\circ \text{ C}$ ($I_{\text{leak}} = 55 \text{ pA/strip}$ at $T = -10^\circ \text{ C}$).

Each layer contains 3×3 DSSDs, which are chained together with wire bonding strip to strip. Ladders of three Si tiles are first assembled and then bonded to three other ladders in the orthogonal direction. Si strip bonding is now a standard technology previously used in, e.g., the Fermi/LAT and AGILE Tracker (see Figure 13) and the PAMELA and AMS-02 cosmic-ray experiments.

Mechanical structure The All-Sky-ASTROGAM Tracker is composed of $2 \times 25 = 50$ basic elements named trays, each one comprising a layer of 3×3 DSSDs with the associated FEE, held by a very light mechanical structure minimizing the amount of passive material within the detection volume. This structure is composed of two frames sandwiching the Si

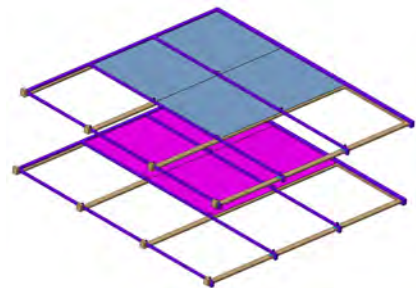


Figure 14: Exploded view of the light mechanical structure of two trays of the Si Tracker.

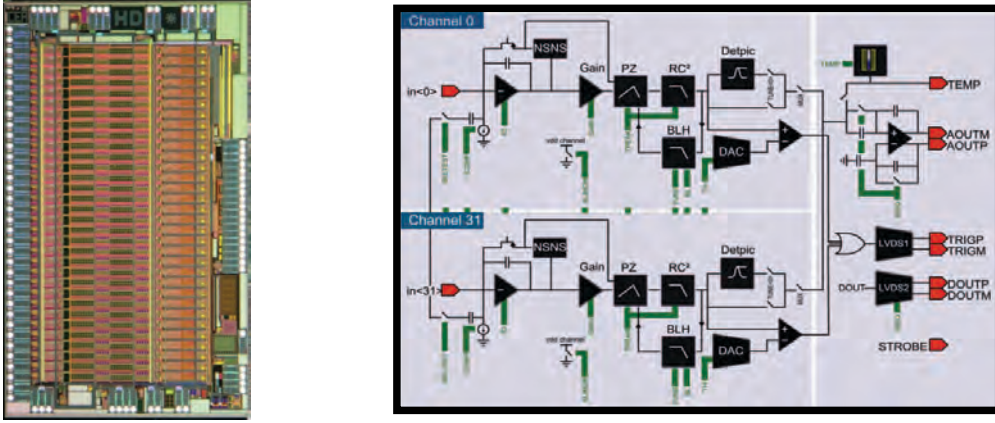


Figure 15: *Left panel* – Picture of the ASIC IDEF-X; the 32 channel inputs are located at the left, distributed every $150 \mu\text{m}$. *Right panel* – Electrical architecture of IdeF-X.

detectors, the rods direction of the upper frame being orthogonal to that of the lower frame, to form a grid (Figure 14). On each side, the support rods are parallel to the DSSD strips to enable the wire bonding. The DSSDs are glued onto the frames with a structural adhesive, and a Kapton[®] foil is added in the middle of the glue thickness to ensure electrical insulation. The frames, which are 2 mm thick, are made of a polymer resin reinforced by high modulus carbon fibers woven into fabrics. Carbon fiber spacers determine a total spacing of the Si layers of 10 mm; placed at the crossing between frames, they limit the vertical displacements under loads achieving a uniform distribution of the displacement among them and realize unilateral connections between the trays.

The trays are assembled together by a structural mainframe composed of vertical fixing aluminum columns. In order to increase the stiffness of each tower, the baseline configuration of the Tracker comprises two honeycomb panels (e.g. Hexel 3/16-5052 + 1 mm thick carbon fiber foils), one at the top (4 cm thickness) and one at the bottom (1 cm thickness).

The Tracker mechanical design is the result of detailed structural calculation based on a simplified Finite Element Model (FEM) and including both static and modal analyses. The maximum vertical displacement obtained by FEM is of 280 microns, far below the rupture limit of Si detectors.

Front-End Electronics The FEE is distributed over the four sides of the Tracker, the detector microstrips being connected to the FEE ASICs through pitch adapters (see Figure 13). The FEE ASICs are the 32-channels IDEF-X BD circuits developed at CEA/Saclay. The 115,200 DSSD signals are read by a total of 3600 ASICs (72 ASICs per layer).

IDEF-X is a $5.8 \times 2.5 \text{ mm}^2$ chip operated at 3.3 V and consuming $800 \mu\text{W}/\text{channel}$ (static dissipated power). IDEF-X BD is bi-directional and thus can read both the n-side and the p-side of a DSSD. It was built based on the AMS CMOS $0.35 \mu\text{m}$ technology using the full custom Rad-Hard libraries, and combine the most recent developments for space applications, including fully space-qualified devices [53, 36]. In particular, IDEF-X BD was extensively studied with respect to radiation tolerance (Single Event Latchup (SEL) – free; Single Event Effect (SEE) $> 9 \text{ MeV cm}^2 \text{ mg}^{-1}$; Total Ionizing Dose (TID) $> 300 \text{ krad}$ w/o effect on noise response), as it was selected for the FEE of the STIX instrument of the Solar Orbiter mission.

Each individual channel of IDEF-X is made of (Figure 15): a charge sensitive preamplifier (CSA) optimized for low current ($< 1 \text{ nA}$) and capacitance around 10 pF, a variable gain (inverting or non inverting) stage, a pole-zero cancellation stage, an adjustable shaper in the range from 1 to 11 μs (peaking time), a baseline holder, providing a stable offset whatever the leakage current into a channel, a peak detector and hold, and a discriminator (each channel, 6 bit DAC) in the range from 0 to 13 keV for Si (the settings is not linear to allow fine tuning in the low range and coarse in the high range). Together with the 32 inputs (DC or AC coupled), the other interfaces of IDEF-X BD are two differential analog output and two independent slow controls. The CSA includes a continuous reset feedback circuitry, with a non stationary noise suppressor to optimize the noise

response into the whole dynamic range.

Figure 16 shows the expected noise performance of IDeF-X BD when used for the readout of three daisy-chained DSSDs of the All-Sky-ASTROGAM Tracker. We see that the ASIC can reach a noise level of about 4 keV FWHM for a shaping time of 6 μs , which meets the All-Sky-ASTROGAM Tracker requirements.

The analog output signals of IDeF-X will be converted to digital signals with the OWB-1 ADC integrated system. OWB-1 is a low noise (0.6 LSB), low power (1 mW per active channel) chip of 11.55 mm² area, including parallel Wilkinson ADC for 16 differential channels with a real 13 bits resolution at a conversion rate of 2.8 μs (and 11 bits resolution at 0.9 μs conversion rate). The chip was also built from the AMS CMOS 0.35 μm technology and it is radiation hard by design (SEL hardened + Single Event Upsets flag). Qualification procedure of this ASIC is on going.

Each side of a DSSD ladder (384 signals) will be readout by 12 IDeF-X ASICs, which will output 12 differential lines. These lines will be connected to one OWB-1 ASIC, which will make the analog-digital conversion. Each side of a tray will then have three OWB-1 ADCs, which will transmit their data to a dedicated FPGA board. This board will have to read the information from the ADC, transmit the Slow Control to the OWB-1 and IDeF-X ASICs, format and transmit the digital data to the BEE.

Back-End Electronics The BEE of the Si Tracker will be placed in the satellite platform (Sect. 5.2). The connection with the FEE will be guaranteed by a dedicated flex fixed to the deployable structure. The BEE is in charge of (i) acquiring the digital signals A/D-converted by the FEE, (ii) matching x- and y- signals to remove single strip noise, (iii) distinguishing and marking events as Compton or pair events; (iv) managing the FEE configuration, (v) providing the required FEE power supplies and the silicon detector polarization voltage (between 40 and 100 V depending on the Si wafer substrate resistivity), and (vi) managing the analog and digital housekeeping data.

4.1.2 Calorimeter

The All-Sky-ASTROGAM Calorimeter is a pixelated detector made of a high- Z scintillation material – Thallium activated Cesium Iodide – for an efficient absorption of Compton scattered gamma-rays and electron-positron pairs. It consists of an array of 784 parallelepiped bars of CsI(Tl) of 5 cm length and 10 \times 10 mm² cross section, read out by silicon drift detectors (SDDs) at both ends. The Calorimeter is arranged in an array of 49 (= 7 \times 7) elementary modules comprising each 16 crystals (see Figure 17). The Calorimeter thickness – 5 cm of CsI(Tl) – makes it a 2.7 radiation-length detector having an absorption probability of a 1-MeV photon on axis of 72%.

The Calorimeter detection principle and architecture are based on the heritage of the space instruments *INTEGRAL*/PICsIT, *AGILE*/MCAL and *Fermi*/LAT, as well as on the particle physics experiment LHC/ALICE at CERN. However, the All-Sky-ASTROGAM Calorimeter features three major improvements with respect to the previous instruments:

- it is a symmetrical detector, designed to be able to detect gamma rays and e^+e^- pairs from the front and the back of the telescope with the same efficiency;
- the energy resolution is optimized to a FWHM of 4.5% at 662 keV (scaling with the inverse of the square root of the energy) by the use of low-noise SDDs for the readout of the scintillation signals, combined with an ultra low-noise FEE;

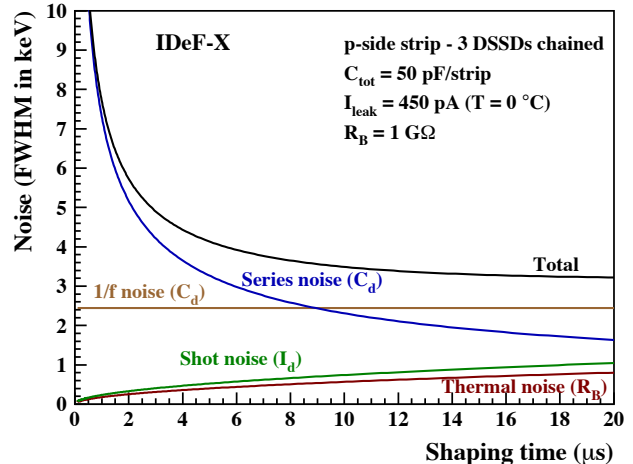


Figure 16: Noise performance of the ASIC IDeF-X for the readout of three chained DSSDs of the Tracker. All noise sources are indicated.

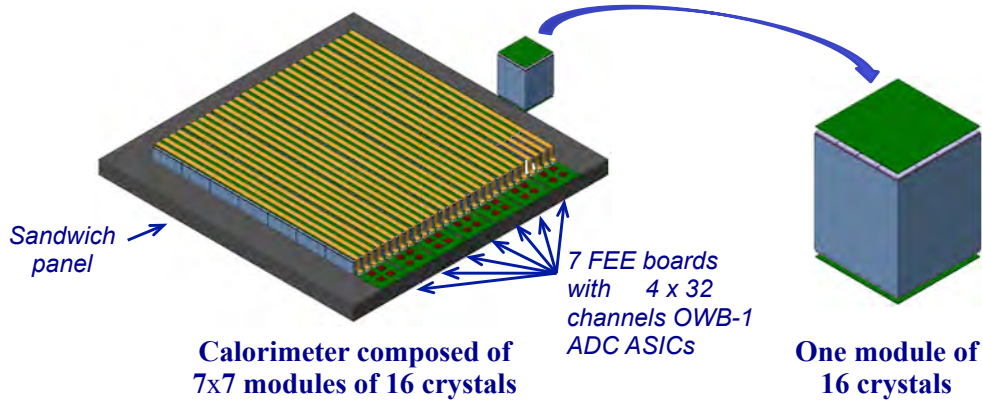


Figure 17: Overview of the Calorimeter and of one of its 49 ($= 7 \times 7$) basic modules comprising 16 CsI(Tl) crystals.

- the spatial resolution is improved by measuring the depth of interaction in the detector from a suitable weighting function of the recorded scintillation signals at both ends; the position resolution along the CsI(Tl) bars is ~ 5 mm FWHM. Accurately measuring the 3D position and deposited energy of each interaction is essential for a proper reconstruction of the Compton events.

The simultaneous data set provided by the Silicon Tracker, the Calorimeter and the Anticoincidence system constitutes the basis for the gamma-ray detection. However, the Calorimeter will also have the capability to trigger the gamma-ray event processing independently of the Tracker, in order to search for fast transient events such as GRBs and terrestrial gamma-ray flashes (See Sect. 4.1.5).

Scintillation crystals and housing The choice of CsI(Tl) as the scintillation material in the baseline design is motivated by the facts that (i) it is one of the brightest scintillator (light yield of 54 photons per keV), (ii) it matches well to the response of Si photodiodes (broad emission spectrum with a maximum at 540 nm), (iii) it is only slightly hygroscopic (much less than, e.g., LaBr₃ and CeBr₃), (iv) it has good radiation hardness properties, and (v) it has already flown on, e.g., the *INTEGRAL*, *AGILE* and *Fermi* satellites. The required 784 CsI(Tl) bars could be produced by, e.g., Saint Gobain Crystals[©], Scionix[©] or Detec Europe[©].

Each crystal will be wrapped with a reflective material in order to optimize the light collection and reduce the optical cross talk. The selected reflective material is the Radiant Mirror Film ESR from 3M, with a thickness of 63 μm . This wrapping material, which is a non-metallic multilayer polymer, was previously employed for the CsI crystals of the *Fermi/LAT* calorimeter, as well as, e.g., for the calorimeters of the *JLAB/DVCS* and *GSI/PANDA* particle physics experiments.

Photosensors: silicon drift detectors Silicon Drift Detectors (SDDs) are solid-state devices suitable for scintillation light detection [33], which can provide an order of magnitude improvement in noise performance with respect to PIN photodiode of equivalent active area. When SDDs are used as readout devices for CsI(Tl) scintillation crystals, the improved noise performance results in a very good energy resolution (4.5% FWHM at 662 keV) and an energy threshold lower than 30 keV [54].

For the All-Sky-ASTROGAM calorimeter we foresee the use of SDDs designed and developed at INFN Trieste, and fabricated at the FBK (SRS-FBK). SDD development at INFN Trieste is a more than 20-years old effort, culminating in the delivery of the large-area SDDs for the Inner Tracking System

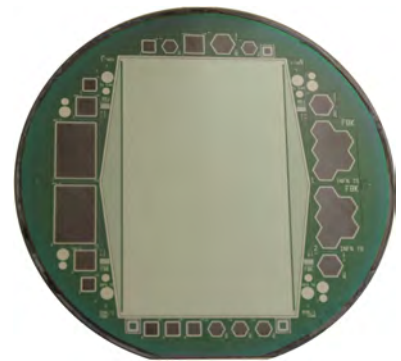


Figure 18: Samples of SDDs fabricated at SRS-FBK.

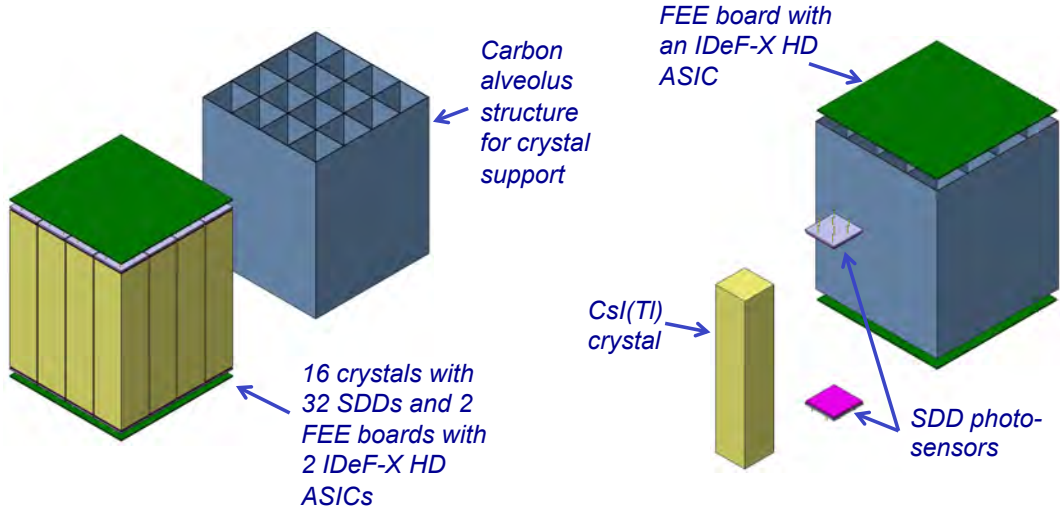


Figure 19: Exploded view drawing of a elementary module of the Calorimeter with its alveolus structure.

of the ALICE experiment at LHC. Later, developments based on this expertise were carried out in the framework of INFN funded R&D projects (XDXL, ReDSOX) aiming at the optimization of SDDs for X-ray and scintillation light detection [66]. In this framework, several SDD arrays of different shape and dimensions were fabricated and tested (Figure 18) and a 6" wafer processing line was successfully set up at SRS-FBK, with mass production capabilities.

In the All-Sky-ASTROGAM Calorimeter, the basic detector element is formed by the optical coupling of a CsI(Tl) bar to two SDDs, one on top and the other at the bottom of the crystal. Such a detector element was already developed in the framework of the R&D efforts described above. The light collection at both ends of the scintillation crystals will enable the reconstruction of the energy and position of interaction along the bars by means of a suitable weighting function of the recorded signals. This hodoscopic architecture was already employed for the AGILE and *Fermi* LAT calorimeters, but using much larger crystals and PIN photodiodes as readout devices. The improved noise performance of the SDDs will allow us to obtain a depth-of-interaction resolution of about 5 mm FWHM when coupled to 50 mm long scintillator bars, as already demonstrated at laboratory level [52].

Mechanical structure The All-Sky-ASTROGAM Calorimeter is made of 49 ($= 7 \times 7$) elementary modules, each of which comprising 16 basic elements made of a CsI(Tl) bar coupled to two SDDs. This gives a total of 784 identical crystals and 1568 SDDs. The active surface covered by the calorimeter is $28 \times 28 \text{ cm}^2$.

An exploded view of a basic module of the Calorimeter is shown in Figure 19. The crystals are supported by an alveolar structure made of a polymer resin reinforced by high modulus carbon fibers. The thickness of the structure walls is $200 \mu\text{m}$. The module array is fixed to a sandwich panel (see Fig. 17), which is stiff enough to hold the weight of the Calorimeter (20 kg). The FEE boards with the OWB-1 ADC ASICs (see below) are fixed to the sandwich panel. The SDD boards with the IDeF-X HD analog ASICs in contact of the collecting anodes are connected to the ADC ASIC boards via Kapton foils (Fig. 17). The low heat generated by the SDD boards ($2 \times 630 \text{ mW}$ for the entire Calorimeter) is also evacuated by the Kapton circuits.

FEE and BEE We foresee using also the IDeF-X ASIC (see Sect. 4.1.1 on the Si Tracker) for the FEE of the Calorimeter. The most appropriate version of IDeF-X for the Calorimeter is HD (high dynamic), which has a dynamic range up to 300,000 electrons, which is four times larger than that of the IDeF-X BD version and is well adapted to the Calorimeter requirements. The 16 signals collected on each side of a module will be read by an IDeF-X HD ASIC placed in the middle of

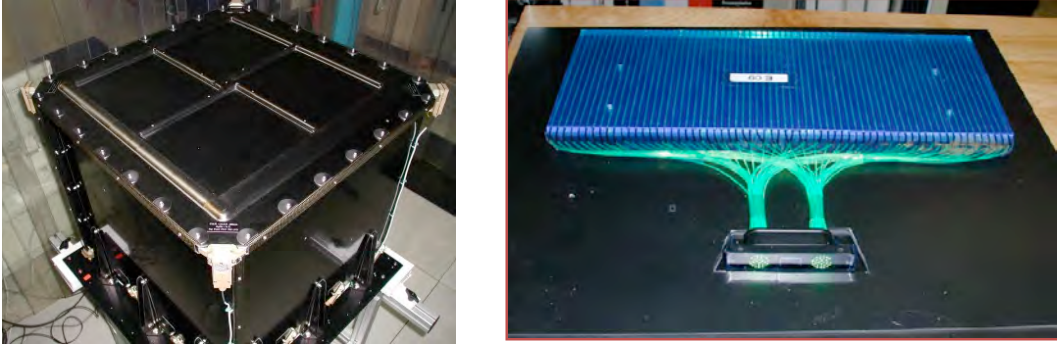


Figure 20: *Left panel* - AGILE AC detector flight unit. *Right panel* - Scintillator tile detector assembly (shown unwrapped) of the Fermi/LAT AC. The green wavelength-shifting fibers carry light to the optical connector in the foreground.

the SDD board. IDeF-X HD is a 32-channels ASIC, but the unused input channels can be readily inhibited.

The analog output signals of the IDeF-X HD ASICs will be converted to digital signals with the same OWB-1 ADC integrated system as used for the Tracker FEE. Each row of the Calorimeter comprising 7 modules generates 112 signals, which can be processed by four 32-channels OBW-1 ASICs placed on a dedicated board fixed to the sandwich panel (see Fig. 17).

The Calorimeter BEE will be placed in the platform, next to the Tracker BEE, the Payload Data Handling Unit and the Power Supply Unit. The BEE is in charge of (i) acquiring the digital signals A/D-converted by the FEE, (ii) managing the FEE configuration, (iii) providing the required FEE power supplies and the SDD polarization voltage (typically between 150 and 200 V), and (iv) managing the analog and digital housekeeping data.

4.1.3 Anticoincidence system

The third main detector of the All-Sky-ASTROGAM payload consists of an Anticoincidence (AC) system composed of panels of plastic scintillators covering the six faces instrument, requiring a total active area of about 1.6 m^2 . All scintillator tiles are coupled to silicon photomultipliers (SiPM) by optical fibers. The architecture of the AC detector is fully derived from the successful design of the AGILE [63] and *Fermi*/LAT [56] AC systems (Figure 20). The particle background rejection is designed to achieve a relativistic charged particle detection inefficiency lower than 10^{-4} , a standard value already realized in current space experiments.

The plastic scintillator type that was selected is the BC400 or BC408 from Saint Gobain Crystals[©] or the equivalent EJ212 or EJ200 from Eljen Technology[©]. For all these materials, the scintillator peak emission is around 425 nm. The scintillator thickness has been set to a minimum of 6 mm in order to get enough light to detect more than 99.99% of the passing through relativistic charged particles. The energy threshold of the AC detectors is set to 100 keV. The light emitted by the plastic is transferred to the SiPM through wavelength shifting optical fibers.

The combination of optical fibers and SiPM provides the best solution to collect the scintillator optical light, as it has the higher gain and gives the best efficiency of charged particle rejection. SiPM has also the advantage over traditional photomultiplier tubes to work at low bias (few tens of volts), so without the need of high voltage. The selected SiPM could be from the B-Series (blue sensitive) of the SensL[©] company. The peak sensitivity of these photosensors is at 420 nm (within a sensitivity range of 300 - 800 nm), which copes well with the plastic scintillator emission. SensL[©] SiPMs were recently studied with respect to radiation tolerance in an ESA-led program and are now at TRL 5. For the readout electronics, we foresee the selection of the VATA64 ASIC from the Ideas Company[©], this chip being optimized for SiPM readout and already space qualified (see Ref. [19]).

4.1.4 Data Handling and Power Supply

The All-Sky-ASTROGAM payload is completed by a Payload Data Handling Unit (PDHU) and a Power Supply Unit (PSU). The PDHU is in charge of carrying out the following principal tasks: (i) payload internal control; (ii) scientific data processing; (iii) operative modes management; (iv) on board time management; (v) Telemetry and Telecommand management. The main functions related to the scientific data processing are: (i) BEE interfacing through dedicated links to acquire the scientific data; (ii) the real-time software processing of the collected silicon Tracker, Anticoincidence and Calorimeter scientific data aimed at rejecting background events to meet the telemetry requirements; (iii) scientific data compression; (iv) formatting of the compressed data into telemetry packets.

The hearth of the PDHU architecture is based on a powerful Digital Signal Processor (DSP) running the payload on-board software. A possible DSP could be the HiRel component C6727B-250 produced by Texas Instruments[©]. This floating point CPU running at 250 MHz is capable of 500 MMACS (2000 MIPS / 1500 MFLOPS) by executing up to 8 instructions in parallel (6 of which floating points).

The PSU is in charge of generating the required payload voltages with high DC/DC conversion efficiency and distributing them to the other sub-systems.

4.1.5 Trigger logic and data flow architecture

The All-Sky-ASTROGAM on-board scientific data processing is composed of two main trigger pipelines, the gamma-ray acquisition mode and the Calorimeter burst search. Both are based on the experience of the AGILE and *Fermi* missions. The simultaneous data sets provided by the silicon Tracker, the Calorimeter and the AC constitute the basis for the gamma-ray detection and processing. The gamma-rays trigger logic is structured on two main levels: Level-1 (fast: 5-10 μ s logic, hardware); and Level-2 (asynchronous, 50 μ s processing, software).

Level-1 is a hardware trigger logic with fast response implemented in the silicon Tracker BEE providing a preliminary discrimination between Compton and pair-producing photon events and a first cut of background events. Discrimination criteria based on the hit multiplicity in the Tracker and in the Calorimeter can provide optimal algorithms to identify Compton events. The Level-1 trigger configuration is defined to save the largest possible number of potential Compton events.

Level-2 is a software trigger stage carried out by the PDHU and aimed, at further reducing the residual particle and photon background of the pair data set and at finalizing the selection of the Compton events. The hearth of the Level-2 trigger stage consists of the track reconstruction of the candidate pair events implemented with Kalman Filter techniques. The Level-2 trigger is a full asynchronous processing stage and does not increase the dead time of the instrument. At the end, the Compton events and the pair events surviving the Level-2 trigger are collected in dedicated telemetry packets and sent to the ground.

The Calorimeter burst search is a software algorithm implemented by the PDHU. The burst search is based on the integration and processing of a proper set of rate meters measuring the trend of the background and foreground counting rates. Since the expected impulsive signals (mainly gamma-ray bursts) are energy and timescale dependent, the rate meters are integrated on different timescales (in the range 100 μ s – 10 s) and energy ranges (in the overall range 30 keV – 200 MeV).

4.2 Performance assessment

The scientific performances of the All-Sky-ASTROGAM instrument were evaluated by detailed numerical simulations with the software tools MEGALib and BoGEMMS. The MEGALib package [84] was originally developed for analysis of simulation and calibration data related to the Compton scattering and pair-creation telescope MEGA [47]. It has then been successfully applied to a wide variety of hard X-ray and gamma-ray telescopes on ground and in space, such as COMPTEL, NCT, and *NuSTAR*. BoGEMMS (Bologna Geant4 Multi-Mission Simulator) is a software for simulation of payload of X- and gamma-ray missions, which has been developed at the INAF/IASF Bologna [26].

It has already been applied to several hard X-ray/gamma-ray instruments and mission projects, including Simbol-X, NHXM, Gamma-Light, AGILE, and GAMMA-400. Both software packages exploit the Geant4 toolkit to model the geometrical and physical parameters of the detectors and simulate the interactions of photons and particles in the instrument.

The numerical mass model of the gamma-ray imager used to simulate the performance of the instrument is shown in Figure 21. An accurate mass model that includes passive material in the detector and its surroundings, true energy thresholds and energy and position measurement accuracy, as well as a roughly accurate S/C bus mass and position are crucial to the modeling. In particular, care was taken to include all passive materials close to the Si and CsI(Tl) detectors.

4.2.1 Background model

The dominant sources of background for All-Sky-ASTROGAM in the MeV domain are the cosmic diffuse gamma-ray background and the background produced by the radioactivity of the telescope materials activated by fast protons and alpha particles. In the pair domain above 10 MeV, the background is mainly induced by fast particles impinging the spacecraft, as well as by the cosmic diffuse radiation. All these components were carefully modeled using the MEGAlib and BoGEMMS environment tools.

The radiation spectrum in L2 is dominated by energetic particles from the Sun (mostly electrons, protons and helium ions) and by Galactic Cosmic Rays (GCRs). So far away from the Earth the screening and trapping effects of the terrestrial magnetic field are negligible. At lower energies (up to roughly 100 MeV) the satellite is exposed to the solar particle flux, with a significant steady flux and frequent energetic events (from every few days to several times per day, depending on the solar activity); on the other hand there are no trapped particles in the geomagnetic field. At higher energies GCRs are modulated by the solar influence, which manifests as a low-rigidity cutoff potential ranging from a few 100s MV to ~ 1000 MV, being anti-correlated with the solar activity.

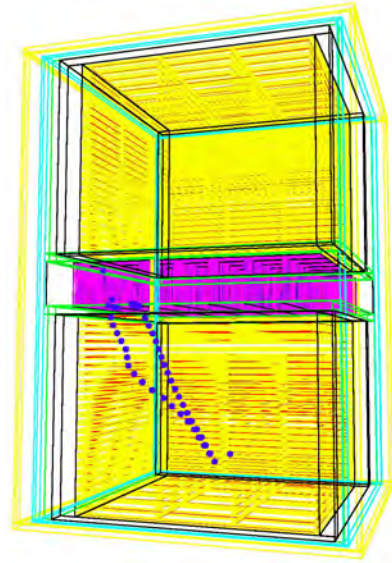


Figure 21: Geant4/MEGAlib mass model of the All-Sky-ASTROGAM telescope, with a simulated pair event produced by a 30-MeV photon.

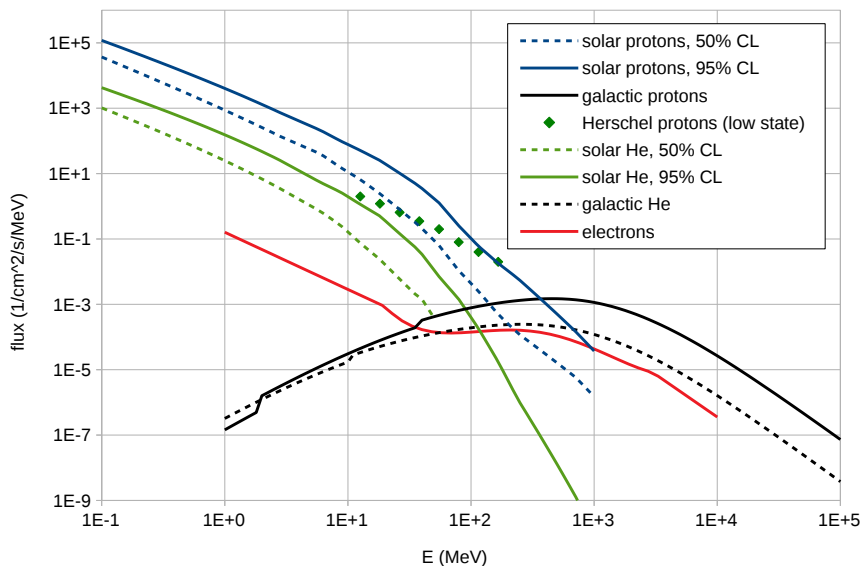


Figure 22: Expected particle background levels for All-Sky-ASTROGAM in L2 (see text).

For protons and ions, especially at low energies, a probabilistic approach must be used. The total particle fluence over the mission lifetime (e.g. to evaluate activation) is easiest to quantify, and an estimate can be obtained by several models for a set confidence level. For shorter mission times (e.g. to estimate sensitivity) we can assume that time intervals corresponding to intense solar particle events can be removed from the data set: at the cost of a limited loss of lifetime the background level is significantly lower than what one would infer from the previous long-timescale fluence estimate. For our environment model (see Fig. 22) we assume launch in 2028, and we use the SAPHIRE model [46] for solar protons and He, at 95% C.L. for the activation and at 50% C.L. for the evaluation of the particle background, respectively. GCRs are described by the ISO15390 model for the mission epoch [44]. Our low solar state estimate is in reasonable agreement with the measurements of the proton flux by Herschel [42], taking into account the difference in solar cycle. Electrons cause no activation, and for simplicity we use an empirical model describing the steady flux from Ref. [62].

At very low energies (below a few tens of keV for protons and α -particles, and below a few hundreds of eV for electrons) a significant plasma flux from the Earth magnetotail is present, dependent on the orbit characteristics and on the solar activity. However, we expect no significant background contribution from this component.

The cosmic diffuse gamma-ray background is taken from *INTEGRAL* and *Fermi*/LAT observations (see [27] and references therein).

4.2.2 Angular and spectral resolution

All-Sky-ASTROGAM will achieve an unprecedented angular resolution both in the MeV domain and above a few hundreds of MeV, i.e. improving the angular resolution of the *CGRO*/COMPTEL telescope and that of the *Fermi*/LAT instrument by a factor of about 3 at both 1 MeV and 100 MeV (Figure 23, left panel).

In the pair production domain, the PSF improvement over *Fermi*/LAT is due to (i) the absence of heavy converters in the Tracker, (ii) the light mechanical structure of this detector minimizing the amount of passive material within the detection volume and thus enabling a better tracking of the secondary electrons and positrons, and (iii) the analog readout of the DSSD signals allowing a fine spatial resolution of about $40 \mu\text{m}$ ($\sim 1/6$ of the microstrip pitch). In the Compton domain, the improvement is due to the better spatial and spectral resolutions of both the Tracker and the

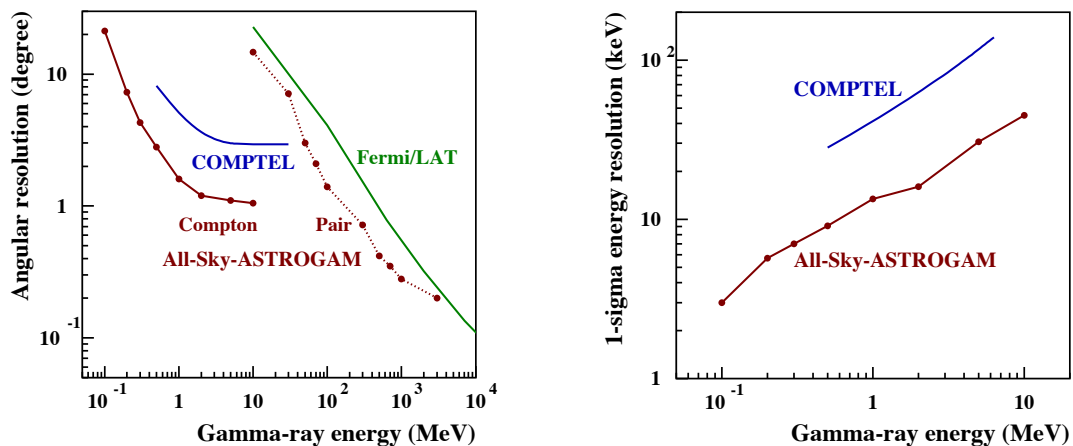


Figure 23: *Left panel* – All-Sky-ASTROGAM on-axis angular resolution compared to that of COMPTEL and *Fermi*/LAT. In the Compton domain, the presented performance of All-Sky-ASTROGAM and COMPTEL is the FWHM of the angular resolution measure (ARM). In the pair domain, the point spread function (PSF) is the 68% containment radius for a 30° point source. The *Fermi*/LAT PSF is from the Pass 8 analysis (release 2 version 6) and corresponds to the FRONT and PSF event type. *Right panel* – 1σ energy resolution of COMPTEL and All-Sky-ASTROGAM in the Compton domain after event reconstruction and selection on the ARM.

Calorimeter. The increase of the angular resolution below ~ 1 MeV is due to the physical limit induced by the Doppler broadening effect from the velocity of the target atomic electrons.

All-Sky-ASTROGAM will also significantly improve the energy resolution with respect to COMPTEL, e.g. by a factor of ~ 3.1 at 1 MeV, where it will reach a 1σ resolution of $\Delta E/E = 1.3\%$ (Figure 23, right panel). In the pair production domain above 30 MeV, the simulated spectral resolution is within 20–30%.

4.2.3 Field of view

The All-Sky-ASTROGAM field of view was evaluated from detailed simulations of the incident angle dependence of the effective area (see Figure 24 as an example). In the Compton domain, the sensitivity is predicted to degrade significantly only for off-axis angles close to 90° . Thus, at 1 MeV, 96% of the sky will be covered *at any time* with a sensitivity within a factor < 2 of the optimal sensitivity for on-axis observations (see Table 2). At 1 MeV, the mean sensitivity over the whole sky is higher (i.e. less good) than the on-axis one by a factor of 1.56.

In the pair production domain, the sensitivity degrades further between 40° and 140° off-axis angle (see Fig. 24). However, at 30 MeV, the mean sensitivity over the whole sky is higher than the on-axis one by only a factor of 2.0.

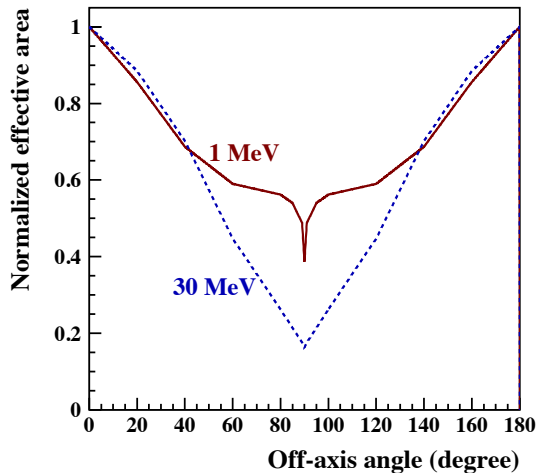


Figure 24: Simulated field of view of All-Sky-ASTROGAM at 1 MeV (Compton domain) and 30 MeV (pair creation).

4.2.4 Effective area and continuum sensitivity

Significantly improving the sensitivity in the medium-energy gamma-ray domain (1–100 MeV) compared to previous missions is a major requirement for the proposed All-Sky-ASTROGAM mission. Tables 2 and 3 present the simulated effective area and continuum sensitivity in the

Table 2: Continuum sensitivity (3σ) of All-Sky-ASTROGAM in the Compton domain simulated with MEGALib, for the detection of a point source on axis in $T_{\text{obs}} = 10^6$ s.

E (MeV)	ΔE spectrum ^(a) (MeV)	Angular selection ^(b)	Effective area after selection ^(c) (cm ²)	Background rate after selection ^(d) (count s ⁻¹)	Sensitivity (photon cm ⁻² s ⁻¹)	Notes
0.15	0.1 – 0.2	8.9°	7.2	1.1	4.3×10^{-4}	Without e-tracking
0.3	0.15 – 0.45	4.9°	17.3	1.1	1.8×10^{-4}	Without e-tracking
0.5	0.25 – 0.75	3.0°	20.1	0.57	1.1×10^{-4}	Without e-tracking
1	0.5 – 1.5	1.7°	9.7	0.19	1.4×10^{-4}	Without e-tracking
2	1.0 – 3.0	1.3°	3.0	0.023	1.5×10^{-4}	With e-tracking
5	2.5 – 7.5	1.4°	2.5	0.0099	1.2×10^{-4}	With e-tracking

(a) Source spectrum is an E^{-2} power-law in the range ΔE .

(b) ARM radius. The best sensitivity results are obtained for an ARM selection slightly larger than the optimal ARM.

(c) Effective area after event selection optimized for sensitivity.

(d) Total background in L2 after event selection optimized for sensitivity.

Table 3: Continuum sensitivity of All-Sky-ASTROGAM in the pair-production domain simulated with BoGEMMS. All results are for a 30° off-axis source and for $T_{\text{obs}} = 10^6$ s.

E (MeV)	ΔE spectrum ^(a) (MeV)	PSF ^(b)	Effective area ^(c) (cm ²)	Inner Galaxy Backgr. rate (count s ⁻¹)	Inner Galaxy Sensitivity (ph cm ⁻² s ⁻¹)	Galactic Center ^(d) Sensitivity (ph cm ⁻² s ⁻¹)	Extragal. Backgr. rate (count s ⁻¹)	Extragal. Sensitivity 3σ (ph cm ⁻² s ⁻¹)
10	7.5 - 15	14.7°	41.97	8.0×10^{-2}	2.0×10^{-5}	3.5×10^{-5}	2.4×10^{-2}	1.1×10^{-5}
30	15 - 40	7.1°	43.34	9.5×10^{-3}	6.7×10^{-6}	1.2×10^{-5}	1.4×10^{-3}	2.6×10^{-6}
50	40 - 60	3.0°	46.71	1.2×10^{-3}	2.2×10^{-6}	3.9×10^{-6}	1.4×10^{-4}	7.6×10^{-7}
70	60 - 80	2.1	48.16	4.8×10^{-4}	1.4×10^{-6}	2.4×10^{-6}	4.4×10^{-5}	4.1×10^{-7}
100	80 - 150	1.4	51.90	1.7×10^{-4}	7.6×10^{-7}	1.3×10^{-6}	1.3×10^{-5}	2.1×10^{-7}
300	150 - 400	0.72	55.73	3.1×10^{-5}	3.0×10^{-7}	5.2×10^{-7}	7.7×10^{-7}	9.0×10^{-8}
500	400 - 600	0.42	60.24	9.0×10^{-6}	1.5×10^{-7}	2.6×10^{-7}	1.4×10^{-7}	8.3×10^{-8}
700	600 - 800	0.35	61.08	5.3×10^{-6}	1.1×10^{-7}	2.0×10^{-7}	6.0×10^{-8}	8.2×10^{-8}
1000	800 - 2000	0.28	62.61	2.6×10^{-6}	8.0×10^{-8}	1.4×10^{-7}	2.4×10^{-8}	8.0×10^{-8}
3000	2000 - 4000	0.20	64.13	4.0×10^{-7}	7.8×10^{-8}	7.8×10^{-8}	2.7×10^{-9}	7.8×10^{-8}

(a) Source spectrum is an E^{-2} power-law in the range ΔE .

(b) Point Spread Function (68% containment radius) derived from a single King function fit of the angular distribution.

(c) Effective area after event selection.

(d) The background for the Galactic Center is assumed to be 3 times larger than that of the Inner Galaxy.

Table 4: All-Sky-ASTROGAM line sensitivity (3σ in 10^6 s) compared to *INTEGRAL*/SPI [68].

E (keV)	FWHM (keV)	Origin	SPI sensitivity (ph cm ⁻² s ⁻¹)	All-Sky-ASTROGAM sensitivity (ph cm ⁻² s ⁻¹)	Improvement factor
511	1.3	Narrow line component of the e ⁺ /e ⁻ annihilation radiation from the Galactic center region	5.2×10^{-5}	3.9×10^{-5}	1.3
847	35	⁵⁶ Co line from thermonuclear SN	2.3×10^{-4}	4.1×10^{-5}	5.6
1157	15	⁴⁴ Ti line from core-collapse SN remnants	9.6×10^{-5}	4.8×10^{-5}	2.0
1275	20	²² Na line from classical novae of the ONe type	1.1×10^{-4}	4.7×10^{-5}	2.3
2223	20	Neutron capture line from accreting neutron stars	1.1×10^{-4}	6.0×10^{-5}	1.8

Compton and pair-production domains. The sensitivity below 10 MeV is largely independent of the source location (inner galaxy vs. high latitude), because the diffuse gamma-ray background is not a major background component in the Compton domain.

4.2.5 Line sensitivity

Table 4 shows the All-Sky-ASTROGAM 3σ on-axis sensitivity for the detection of key gamma-ray lines, together with the sensitivity of the *INTEGRAL* Spectrometer (SPI). The latter was obtained from the *INTEGRAL* Observation Time Estimator (OTE) assuming 5×5 dithering observations. The reported line widths are from SPI observations of the 511 and 847 keV lines (SN 2014J), and from theoretical predictions for the other lines. Noteworthy, the neutron capture line from accreting neutron stars can be significantly redshifted and broadened (FWHM between 10 and 100 keV) depending on the geometry of the mass accretion [25]. We see that All-Sky-ASTROGAM will achieve a gain in sensitivity compared to SPI for all gamma-ray lines, the most significant improvement being for the 847 keV line from ⁵⁶Co decay in Type Ia SNe. Thanks to its very large field of view, All-Sky-ASTROGAM will also be able to detect the early gamma-ray line at 158 keV from ⁵⁶Ni decay, which is expected before the maximum optical light in thermonuclear SNe, and which is fundamental to understanding the nature of the progenitor and the explosion mechanism.

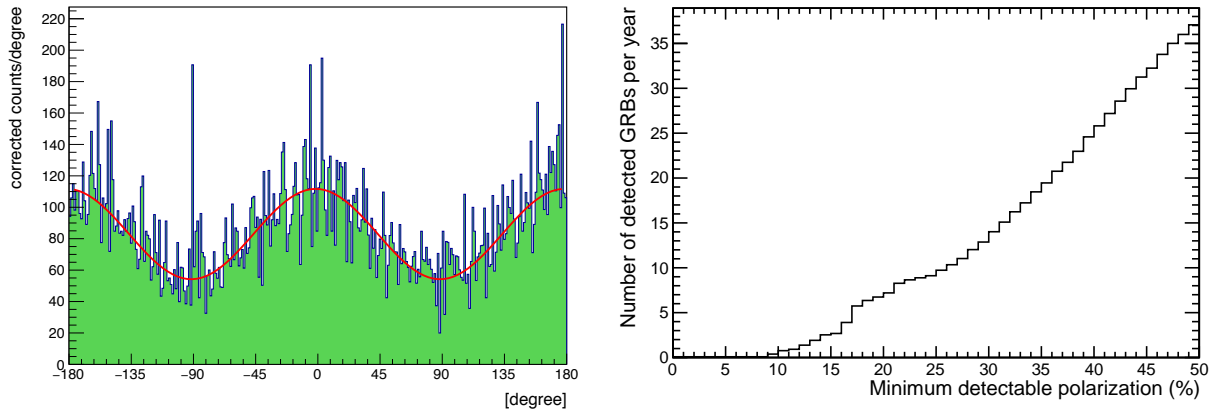


Figure 25: *Left panel* – Geometry-corrected polarization response (polarigramme) of All-Sky-ASTROGAM in the 0.2 – 2 MeV range for a 100% polarized, Crab-like source observed on axis for 10^6 s. The corresponding modulation is $\mu_{100} = 0.35$. *Right panel* – Cumulative number of GRBs to be detected by All-Sky-ASTROGAM as a function of the MDP at the 99% confidence level.

4.2.6 Polarization response

Both Compton scattering and pair creation partially preserve the linear polarization information of incident photons. In a Compton telescope, the polarization signature is reflected in the probability distribution of the azimuthal scatter angle. In the pair domain, the polarization information is given by the distribution of azimuthal orientation of the electron-positron plane (see, e.g., [23]). All-Sky-ASTROGAM will be able to perform unprecedented polarization measurements thanks to the fine 3D position resolution of both the Si Tracker and the Calorimeter, as well as the light mechanical structure of the Tracker, which is devoid of any heavy absorber in the detection volume.

The left panel of Figure 25 shows an example of a polarigramme in the 0.2 – 2 MeV range (i.e. in the Compton domain), simulated with MEGALib. The calculations assume a 100% polarized emission from a Crab-like source observed on axis. From the obtained modulation ($\mu_{100} = 0.35$), we find that at low energies, All-Sky-ASTROGAM will be able to achieve a Minimum Detectable Polarization (MDP) as low as 2% for a Crab-like source in 1 Ms (statistical uncertainties only). The instrument polarization sensitivity is very good whatever the source position: in the 0.2 – 2 MeV range, the modulation remains in the range 0.30 – 0.35 whatever the source incidence angle between 0° and 180° . After one year of effective exposure, the achievable MDP for a 10 mCrab source will be about 29%.

The right panel of Figure 25 shows the number of GRBs that will be detected by All-Sky-ASTROGAM as a function of the MDP fraction at the 99% confidence level (MDP_{99}) in the 100–300 keV band. This distribution was obtained using the Fourth BATSE GRB Catalog [59] and assuming GRBs are uniformly distributed over the entire sky. MDP_{99} was calculated using the 100–300 keV fluence and the T_{90} duration from the catalog and approximating the GRB emission spectrum by a typical Band function [24] with $\alpha = -1.1$, $\beta = -2.3$, and $E_{\text{peak}} = 0.3$ MeV. We see in Figure 25 that All-Sky-ASTROGAM should be able to detect a polarization fraction of 20% in about 7 GRBs per year. This polarization information, combined with spectroscopy over a wide energy band, will provide unambiguous answers to fundamental questions on the sources of the GRB highly relativistic jets and the mechanisms of energy dissipation and high-energy photon emission in these extreme astrophysical phenomena.

4.3 Required resources

Tables 5, 6 and 7 show synthetically the required resources of the gamma-ray imager in terms of mass, power consumption and data acquisition. The mass budget presented in Table 5 includes a maturity margin of 20% for all items, except for the active elements of the Tracker and the

Table 5: Mass budget of the All-Sky-ASTROGAM gamma-ray imager.

PAYLOAD MASS BUDGET		Predicted Mass [kg]	Maturity margin	Predicted mass + maturity margin [kg]
Silicon Tracker	Silicon tiles	4.7	5%	4.9
	FEEs, harness, glue, mechanics	16.0	20%	19.2
Calorimeter	Crystals	17.6	5%	18.5
	FEEs, harness, housing, mechanics	6.0	20%	7.2
Anticoincidence	Plastic scintillators	6.6	20%	7.9
	FEEs, mechanics	8.0	20%	9.6
Thermal control	Thermal harness	3.5	20%	4.2
Harness		5.0	20%	6.0
TOTAL		67.4		77.5

Table 6: Power budget of the All-Sky-ASTROGAM gamma-ray imager.

PAYLOAD POWER BUDGET	Design [W]	Margin	Total [W]
Silicon Tracker	92.0	20%	110.4
Calorimeter	5.0	20%	6.0
Anticoincidence system	5.0	20%	6.0
Heaters	15.0	20%	18.0
TOTAL	117.0		140.4

Calorimeter for which the margin is of 5%.

The power budget is presented in Table 6. It was used to preliminary size the solar panels and batteries of the platform (Sect. 5.2) and specify the required resources of the thermal control (Sect. 4.4.1). This budget does not include the power consumption of the Tracker, Calorimeter, and AC BEEs (24 W), the PDHU (18.0 W), and the PSU (60 W; including the DC-DC conversion inefficiency).

The data acquisition budget presented in Table 7 has been prepared to evaluate the required telemetry in downlink and to size the on-board mass memory requirement (Sect. 5.7). Considering an overall margin of 20%, the total average data generation rate before data compression amounts to 839 kbps, or 72 Gb per day. The most important data generation is associated to the measurement of the pair events, due to the average event packet length (10 kbits).

The raw data generated by the payload will be compressed in the PDHU before being formatted into telemetry packets. Applying standard compression programs optimized for large text file to representative All-Sky-ASTROGAM payload data, a compression factor of 2.6 was obtained. We assume that the payload data size reduction can be higher than 2.6 with a compression code optimized for telemetry packets.

4.4 Specific interface requirements

The All-Sky-ASTROGAM instrument does not have special interface requirements with respect to the platform and ground segment. Specific requirements are described below.

4.4.1 Thermal control system

The P/L thermal control is aimed at channeling the heat generated by the running instrument electronics (140 W) towards the platform interface. The temperature requirement in the Tracker FEE areas is in the range $-10^{\circ} - 0^{\circ}$ C. The temperature gradient over the whole instrument should not exceed 5° C. The thermal control system will be based on consolidated heat pipe technology.

Table 7: Data acquisition budget of the All-Sky-ASTROGAM gamma-ray imager.

Source	Average acquisition rate (kbps)	Note
P/L HKs	12.0	15.000 HK parameters coded with 16 bits; sampling time: 20s
P/L engineering reports	0.1	TC acceptance/execution reports, anomaly reports, memory dump reports etc.
Gamma-ray Compton events (AC, Silicon Tracker, and Calorimeter data)	150.5	Average output event rate: 570Hz; average event packet length: 264 bits
Gamma-ray Pair events (AC, Silicon Tracker, and Calorimeter data)	500.0	Average output event rate (>10MeV): 50Hz; average event packet length: 10 kbits
Silicon Tracker Scientific ratemeters	4.8	300 ratemeters (1 for each ladder); Integration time: 1s
Calorimeter Burst data	13.5	1 GRB/day (100s including pre-burst & post-burst); average event rate: 4kHz
Calorimeter Scientific ratemeters	10.4	Spectra of 13 energy channels between 30keV-200MeV; integration time: 10ms; 8 bits per energy bin
AC Scientific ratemeters	8.0	6 ratemeters (1 for each AC side); integration time: 1ms; 8 bits per energy bin
Total (kbps)	699.3	
Margin 20%	139.9	
Total with margin (kbps)	839.2	

Data handling, back-end electronics and power supply units are hosted within the satellite platform do not require special arrangements and will be subject to the platform thermal control.

4.4.2 Pointing and alignment

The Attitude and Orbital Control Systems requirements are not critical, with an Absolute Pointing Error < 1 deg, a Relative Pointing Error < 0.01 deg/s and an Absolute Knowledge Error < 30 arcsec (to be reached after ground processing), which are to be obtained using standard class sensors and actuators. Given the instrument wide field of view, the payload pointing and alignment requirements are modest. As customary for silicon detectors in space, in-orbit alignment will be checked with high-energy protons. On the ground, alignment will be carried out with muons in standard fashion.

4.5 Calibrations

The on-ground calibration of All-Sky-ASTROGAM will be performed at three levels: calibration of the individual active elements of the three main detectors (DSSDs, CsI(Tl) crystals, plastic scintillators), calibration of the sub-systems separately, and calibration of the whole instrument. The purpose of the calibration of the active elements is to check for their proper operation and measure the energy and spatial response (channel threshold, gain, and offset, possible non-linearity, uniformity, resolution) of all the individual detectors. This work will be performed in parallel in each laboratory contributing to the active element procurement and the Tracker tray assembly. It will be done with a set of appropriate radioactive sources using various dedicated test benches for the different detectors. Calibration of the sub-systems (Tracker, Calorimeter, and AC) will then be done with radioactive sources and a muon telescope.

The purpose of the on-ground calibration of the whole instrument is to validate the numerical simulation and the data analysis software with controlled events (gamma-ray energy, incoming direction, polarization properties) and establish the overall instrument response. The flight model of the instrument will be exposed to both polarized and unpolarized monochromatic beams of gamma rays from (1) high-intensity radioactive sources with energies in the range 100 keV to 1.8 MeV (e.g. ^{57}Co , ^{137}Cs , ^{22}Na , ^{88}Y) (2) nuclear-reaction induced gamma rays from a low-energy van der Graaff accelerator (e.g. at Orsay, France) and (3) a source of tagged gamma rays produced by Bremsstrahlung or Compton scattering as operating at the INFN National Laboratories in Frascati

and at CERN. For the intermediate gamma-ray energy range, we will use the $^{13}\text{C}(p,\gamma)^{14}\text{N}$ nuclear reaction at the two resonance energies $E_p = 550$ and 1747 keV, as it produces a set of well-calibrated gamma-ray lines from $E_\gamma = 1.6$ to 9 MeV [48]. A large number of measurements will be performed for various incident angles and relative positions of the gamma-ray beams, which will require a MGSE able to displace All-Sky-ASTROGAM in 3D and rotate it around two orthogonal axes.

4.6 Technology readiness and relevant heritage

The Technology Readiness Levels (TRL) of the payload is summarized in Table 8. We see that all of the All-Sky-ASTROGAM technologies have $\text{TRL} \geq 5$.

Table 8: Technology Readiness Levels for the All-Sky-ASTROGAM payload.

S/S	Item	TRL	Comments
Si Tracker	Double-sided silicon strip detectors	> 6	DSSDs have been extensively used in high-energy astrophysics/cosmic-ray instruments and have flown on several space missions (NINA, PAMELA, AMS-02). Considering that no specific technological developments are required for the All-Sky-ASTROGAM detectors, the resulting TRL is well over the required level of 6.
	2-D Si ladder bonding	5	The proposed 2-D bonding procedure is a customization of the bonding technique already used for the PAMELA and AMS-02 space missions. The involved development activity is the implementation of mechanical fixtures needed to guarantee the alignment of the silicon tiles during the bonding on the two sides of the silicon planes. Bonding machines with work area in excess of 30×30 cm ² are already available on the market so the procedure is compliant with the state of the art of bonding techniques used in commercial/industrial context. In addition, the 2-D bonding procedure has already been successfully applied for the on-ground MEGA reduced prototype developed in Germany by our group. The resulting TRL is 5.
	Tray mechanics	> 6	The tray design and manufacturing as well as the gluing and alignment procedures are directly derived by the AMS-02 mission, where they have been fully qualified. The resulting TRL is > 6.
	FEE	5	The Silicon Tracker FEE is based on the IDeF-X BD ASIC developed at the CEA/Saclay. This component has been selected for the STIX instrument of the Solar Orbiter mission and on-ground qualified in representative environment. It is at TRL 5 and soon (2020) at TRL 9.
	BEE	> 6	The logic design of the BEE will be implemented on the basis of the architecture and trigger algorithms already developed, implemented and tested in the AGILE and Fermi missions. The part list will be based on new-generation space qualified components. It is reasonable to assume a $\text{TRL} > 6$.
CAL	CsI detector assembly	> 6	The design and manufacturing of the detector assembly (including the CsI crystals, the wrapping and optical coupling) are based on the technologies and procedures developed in the context of the AGILE (Mini-Calorimeter instrument) and INTEGRAL (PICsIT instrument) missions where they have been fully qualified. $\text{TRL} > 6$ is thus appropriate.
	SDD	5	The technology and fabrication process of the Silicon Drift Detectors is the same as the one that was subject of an extensive development activity within the assessment phase of the LOFT ESA M3 mission and for the eXTP mission. The corresponding TRL is now 5.
	FEE	5	The Calorimeter FEE is based on the IDeF-X HD ASIC developed at the CEA/Saclay, which is at TRL 5.
	BEE	> 6	The logic design of the BEE will be implemented on the basis of the architecture and trigger algorithms already developed for the AGILE Mini-Calorimeter. The part list will be based on new-generation space qualified components. $\text{TRL} > 6$ is appropriate.
AC	AC detector	> 6	The nominal configuration of the AC detector (including plastic scintillator, fibers and optical glue), as well as the involved technologies and assembly procedures are derived by the AGILE and Fermi missions. $\text{TRL} > 6$ is appropriate.
	SiPM	5	SiPMs from the SensL [®] company were recently studied with respect to radiation tolerance in an ESA-lead program and are now at TRL 5.
	FEE	> 6	We foresee the use of the VATA64 ASIC from the Ideas [©] company. This chip was optimized for SiPM readout and is already space qualified in the framework of the JAXA/Astro-H mission. $\text{TRL} > 6$ is appropriate.
Avionics	PDHU & PSU	> 6	The PDHU and PSU hardware design will be developed on the heritage of the AGILE and Fermi missions using technologies and electronic components well proven in space. Furthermore, the PDHU HW/SW logic performing the GRID data processing and the CAL Burst Search will be designed on the basis of the trigger algorithms already successfully developed, implemented and tested in the AGILE mission. The part list will be based on new-generation space qualified components. $\text{TRL} > 6$ is appropriate.
Thermal control		> 6	The design of the thermal control will be based on standard technologies for space missions. The resulting TRL is well over the required level of 6.

5 Mission Configuration and Profile

5.1 Mission overview

The All-Sky-ASTROGAM spacecraft will be launched to the Sun-Earth L2 Lagrange point as co-passenger to the ARIEL mission (in stacked configuration). The spacecraft being released at the L2 point will make use of its autonomous propulsion to reach its operational orbit. The launch of the F mission with ARIEL offers a unique opportunity to place on a quasi-periodic orbit around L2 a sensitive gamma-ray detector continuously observing every single gamma-ray source in the sky during 2 years, i.e. the entire mission lifetime, with very good localization capabilities (e.g. 40 arcmin at 300 MeV) and excellent sensitivity to polarization in the MeV range. The gamma-ray imager will be attached to a six meters-long deployable boom, which will be deployed when the spacecraft reaches its operational orbit, to reduce the gamma-ray shadow cast by the satellite platform on the telescope and decrease the instrument background induced by cosmic-ray interactions with the platform materials. The spacecraft is 3-axis stabilized.

The Attitude and Orbital Control Systems requirements are not critical, with an Absolute Pointing Error < 1 deg, a Relative Pointing Error < 0.01 deg/s and an Absolute Knowledge Error < 30 arcsec (to be reached after ground processing), which are to be obtained using standard class sensors and actuators.

5.2 Spacecraft overview

The All-Sky-ASTROGAM system is composed by a spacecraft in L2 and a ground segment, which includes the ESA Deep Space Network stations, in charge of performing the spacecraft control, monitoring, and the acquisition of scientific data. The All-Sky-ASTROGAM spacecraft has the purpose to observe the sky according to a predefined pointing plan uploaded from ground. Different pointing profiles can be selected in order to observe selected sky regions or to perform a scanning that, thanks to the wide P/L field of view, can cover almost the whole sky at each orbit.

The All-Sky-ASTROGAM spacecraft platform is made of a structure that mechanically supports both the ARIEL spacecraft during launch and all the spacecraft elements (boom, instrument, instrument electronics and the platform subsystems). Figure 26 shows the spacecraft in stowed and in deployed configurations.

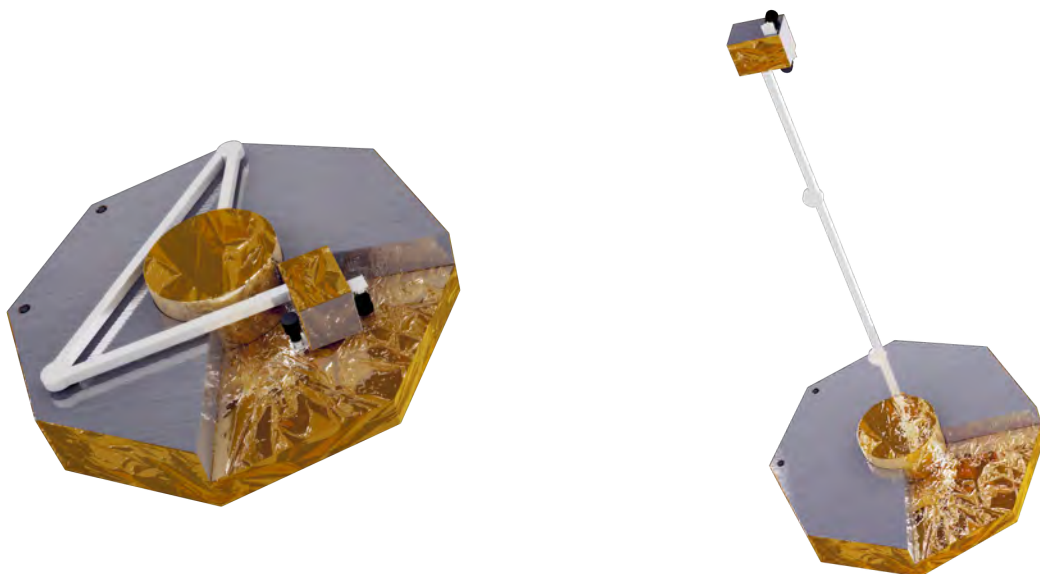


Figure 26: All-Sky-ASTROGAM spacecraft in stowed (*left panel*) and in deployed (*right panel*) configurations.

5.3 Operational orbit

The Lagrangian point L2 lies on the line through Sun and Earth, at 1.5×10^6 km beyond Earth; it is a point nominally unstable but it is possible to find periodic orbits that, even if not perfectly stable, require a modest effort for the station keeping. The following three main categories of orbits can be considered:

- Lyapunov Orbit: a periodic orbit in the plane of motion of the primary bodies.
- Lissajous Orbit: a combination of a planar and vertical components in the periodic orbit
- Halo Orbit: a special case of Lissajous orbits where the in-plane and out-of-plane frequencies are equal.

The Δv budget for maintaining the satellite in its operative orbit around the L2 point is considered applicable whatever the orbit is. The main contributions to the Δv budget are (i) station keeping for 2 years, (ii) wheel desaturation with thrusters, and (iii) de-orbiting.

Station keeping for 2 years. The consumption requested for the Station Keeping is very depending on the final orbit and on the maintenance strategy. For dimensioning the satellite, a conservative estimation of 12 manoeuvres per year with a total Δv of 20 m/s per year is assumed.

Wheel desaturation with thrusters. In the L2 point, the wheel desaturation shall be performed by using chemical thrusters. Assuming standard wheels and propulsion system, about 3 kg per year can be assumed. A total Δv of 10 m/sec per year should also be considered.

De-orbiting. The rather new class of Lagrangian points orbits (LPO) is becoming particularly appealing for a number of space applications. The number of LPO missions has increased over the last 15 years and a further growth is expected within the next 10 years, pointing out the importance of this region for the next space missions. Typically, L1 and L2 are the liberation points most commonly exploited by space missions. Since their dynamical instability, an uncontrolled spacecraft at the end of its operative life tends to leave its operative orbit; this self-cleaning behaviour suggests that no protected regions have to be defined for LPO missions. Nonetheless, these departing trajectories can get back to the Earth-Moon system. In these circumstances, interference with LEO and GEO protected regions can occur as well as re-entry in the Earths atmosphere with large casualty area. In light of this consideration, an end-of-life disposal strategy for LPO spacecraft is mandatory. Three options can be considered:

- Lunar impact;
- Earth reentry;
- Disposal on graveyard heliocentric orbits.

The first two strategies require a controlled re-entry for not impacting on pre-defined zones. The third strategy is the simplest one since, typically, LPO missions can be easily injected into heliocentric orbits, taking advantage of their features. However, long-term propagation highlight the possibility of spacecraft reentries in the Earth-Moon system, which might lead to potential close encounters with the Earth. Thus, despite their natural origin, a disposal manoeuvre is still necessary to stabilize these graveyard orbits or at least to tune the corresponding orbital parameters, avoiding the occurrence of risky conditions in the long-term. In this work, two different methods are proposed. The consumption depends on the time requested for the disposal, but $\Delta v = 10$ m/s are deemed reasonable.

The Δv budget is summarized in Table 9. The corresponding total mass of propellant required for the nominal mission lifetime is < 30 kg (including the propellant need to the AOCs for wheel desaturation).

Table 9: Summary of the Δv budget for 2 years of mission

Contribution	Δv (m/s)
Station keeping	40
Wheel desaturation	20
De-orbiting	10
Margin (15%)	11
Total	81

5.4 Spacecraft preliminary design

The All-Sky-ASTROGAM spacecraft platform is made of a central tube structure that mechanically supports both the ARIEL spacecraft during launch and all the spacecraft elements (boom, instrument, instrument electronics and the platform subsystems). Figure 27 shows different views of the spacecraft, with the boom supporting the payload both in stowed and deployed configuration. The spacecraft is built around the structural central tube: the spacecraft tank is located in the space inside the tube structure, the deployable boom is located around the tube (Fig. 27) and all other satellite subsystems are located inside the octagonal box mounted around the central tube. Four Fixed Solar panels are located on the rear side (with respect to the front side where the boom is located). Both the payload and the boom, when in stowed position, are held down and release mechanisms to the central tube. Figure 28 shows how the spacecraft is accommodated inside the launcher, below the ARIEL Spacecraft.

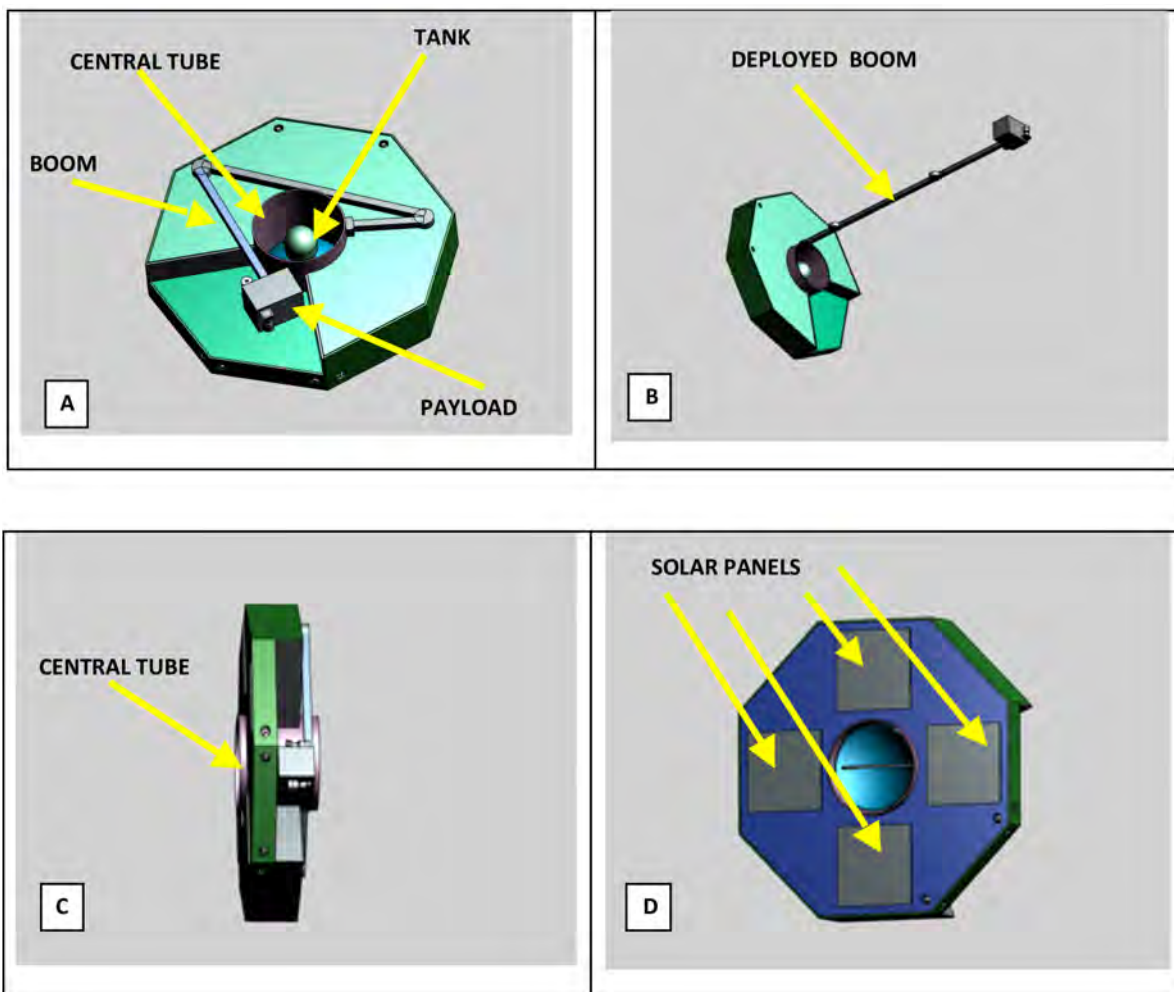


Figure 27: All-Sky-ASTROGAM spacecraft: A) Stowed configuration; B) Deployed configuration; C) Stowed configuration lateral view; D) Stowed configuration rear view.

The All-Sky-ASTROGAM platform is based on a centralized computer, hosted in the OBDH unit, running the SW in charge of managing all satellite services including power and AOCS applications and implementing the satellite FDIR. The OBDH unit is also in charge of TM/TC data encoding/decoding and communication with the payload, including acquisition and storage of scientific data. A mass memory of 32 Gbytes is available for data storage. The OBDH unit redundancy is managed by a reconfiguration function that performs the health check of the active OBDH section providing the possibility to switchover autonomously on the redundant section in case of a detected failure.

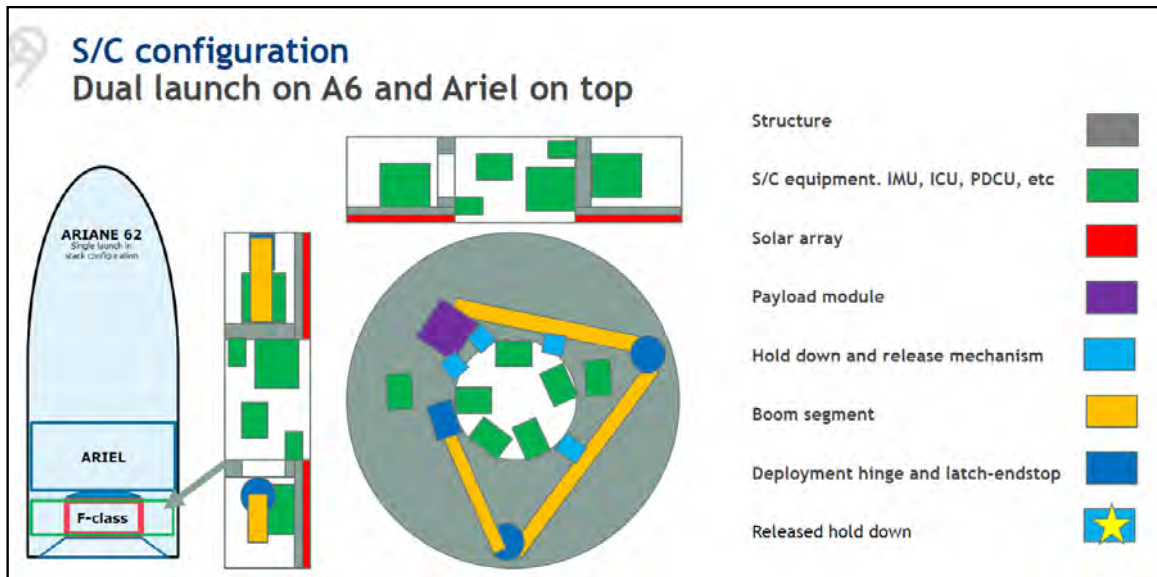


Figure 28: All-Sky-ASTROGAM spacecraft accommodation overview.

A precise timing of the payload data ($1 \mu\text{s}$ at 3σ) is required to perform a proper on-ground data processing able to guarantee the scientific performances of the mission. As already implemented by the AGILE mission, the required timing performance can be obtained by a GPS unit directly connected with the PDHU in order to allow a fine synchronization with the time reference.

Communication with the ground is ensured by an X-band TM/TC subsystem in charge to perform:

- satellite monitoring and control;
- downloading of the scientific data.

The TM/TC subsystem is composed by:

- 2 transmitters in cold redundancy configuration;
- 2 receivers in hot redundancy configuration to guarantee the possibility to contact the satellite;
- a radio frequency distribution in charge to provide proper connection between transceiver and the antenna network;
- a single directional antenna.

The available data rates are:

- downlink: 8 Mbps;
- uplink: 4 kbps.

The AOCS requirements for the All-Sky-ASTROGAM mission are not critical.

The propulsion subsystem is design is a monopropellant hydrazine, blow-down mode propulsion system. The hydrazine is contained in a diaphragm tank, together with the pressurant. From a preliminary estimation of the propellant budget, the amount of hydrazine required to fulfil the mission needs are $< 30 \text{ kg}$ for 2 years mission.

The required pointing accuracy ($\pm 1 \text{ deg}$), stability ($0.01^\circ/\text{s}$), and attitude knowledge of 1 arcmin (to be reached after ground processing) can be obtained using standard class sensors and actuators. The 3-axis stabilized attitude control is achieved mainly using a set of four reaction wheels used in zero momentum mode ensuring the possibility to perform fast repointing manoeuvres. Thrusters are provided to perform wheels desaturation and to support a safe attitude pointing based on a basic subset of ACS items.

Attitude reconstruction is based on star trackers outputs; no gyros are required. Three star trackers are provided in order to guarantee the single point failure tolerance and to ensure the availability of at least one star tracker almost in any attitude condition. In addition to the star trackers, magnetometers and coarse star sensors are available.

The power S/S is in charge to generate, manage and distribute the power to all satellite equipment. It is composed by the following elements:

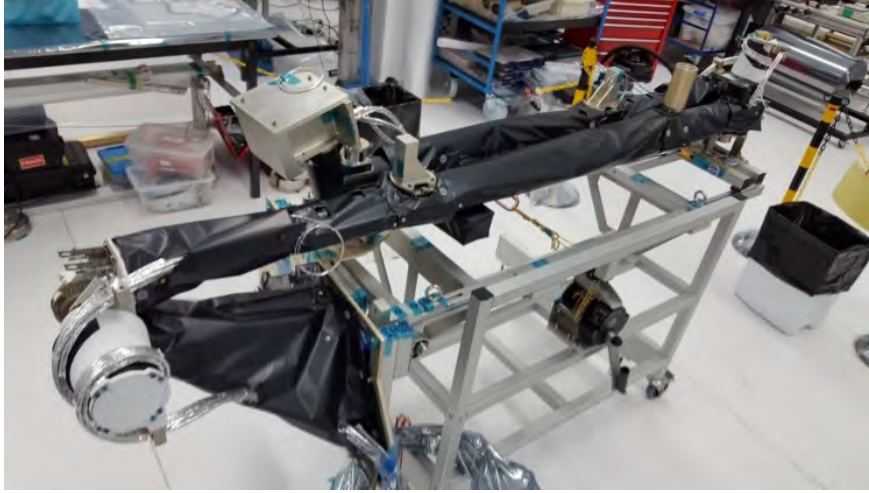


Figure 29: Solar Orbiter Magnetometer boom.

- four solar array panels (1 m² each);
- Li-Ion rechargeable battery
- an internally redundant Power Electronic Box (PEB), to distribute power generated by the solar array and to manage the battery charge-discharge activities.

The four fixed solar array panels are provided to guarantee sufficient power generation in all the expected payload pointing scenarios. The power budget (see Table 12) has been used to preliminary size solar panels and battery. For the solar array, the power required at end-of-life (EoL), including power to recharge the battery, is of about 1000 W taking into account a system margin of 20% on the power consumption. A total surface of solar panels of about 4 m² is then required to fulfil the mission needs (considering a solar radiation in L2 of 1340 W/m²).

5.5 Deployable boom

The proposed concept for the deployable boom is based on an industry study performed by SENER exploiting their experience for the booms of the Solar Orbiter and JUICE Magnetometers (see Fig. 29). The system described here includes:

- Hinge deployment mechanism (DM);
- Rotary Actuator and control electronics;
- Mast (typically made in carbon fiber reinforce plastic);
- Hold-down and release mechanism (HDRM).

The proposed concept is based on three 80 mm diameter CFRP tube segments, each of them bonded to Ti6Al4V end fittings. Additional Ti6Al4V fittings are implemented for HDRMs. For the fixation of the system during launch, four HDRMs will be used as per the following (see Fig. 30):

- HDRM1 will attach the Boom 2 to the spacecraft panel;
- HDRM2 will attach the Boom 3 to the spacecraft panel;
- HDRM3 and HDRM4 will attach the payload to the spacecraft panel.

Table 10: Mass budget of the All-Sky-ASTROGAM deployable boom.

EQUIPMENT	Number of Units	Mass per unit [kg]	Total mass [kg]
Actuators	3.0	2.5	7.5
Hold-down and release mechanism	4.0	1.5	6.0
Boom 1 m	1.0	3.0	3.0
Boom 2 m	1.0	4.0	4.0
Boom 3	1.0	5.0	5.0
Latches and stops	3.0	1.0	3.0
Harness	1.0	2.5	2.5
Total mass			31.0

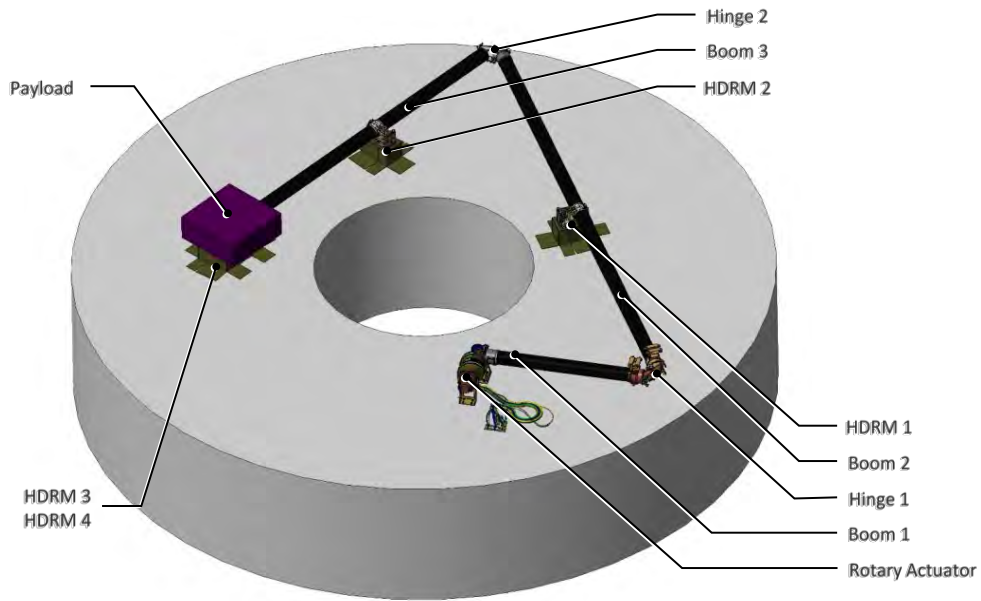


Figure 30: Boom deployment mechanism concept.

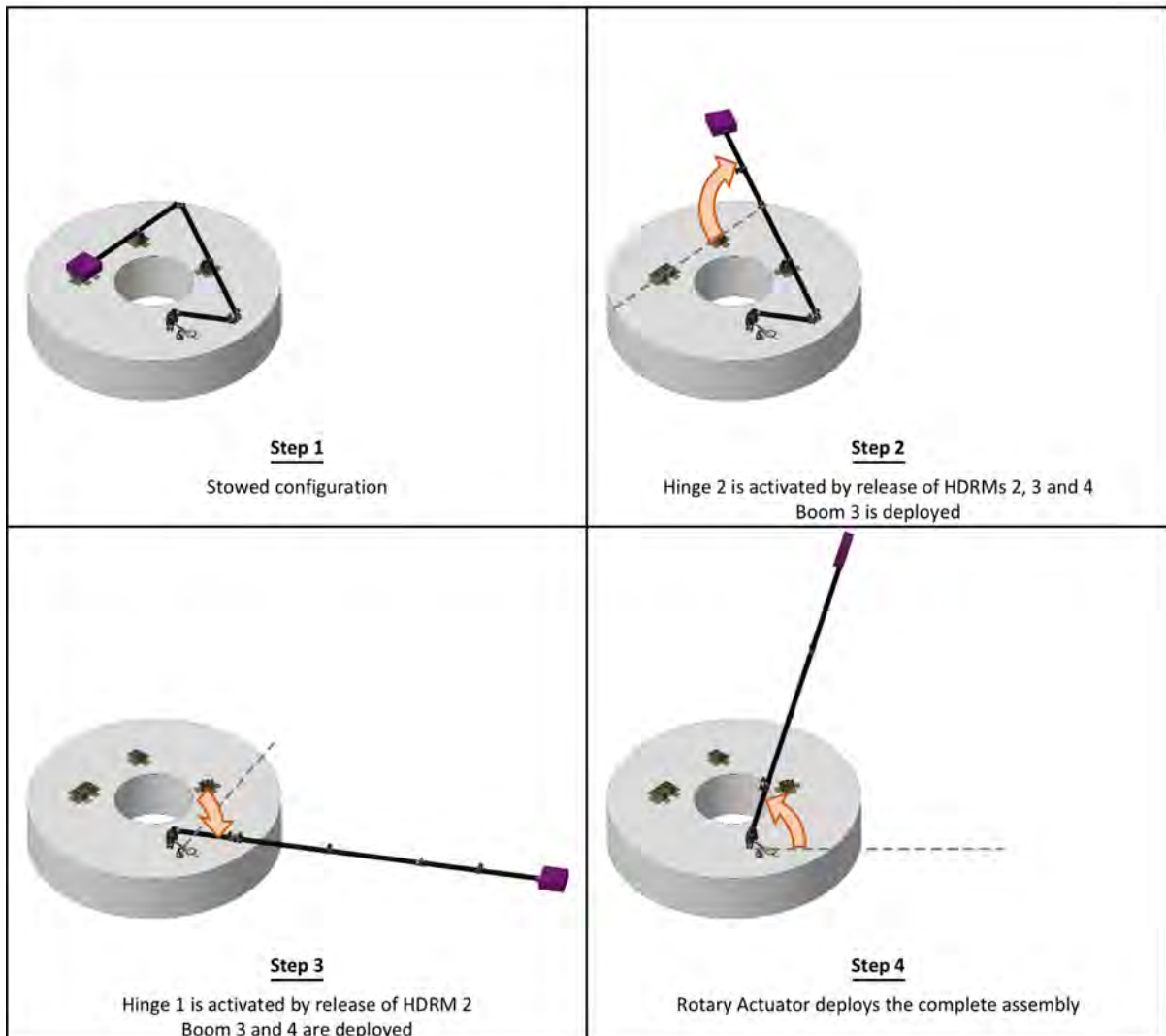


Figure 31: Boom deployment sequence.

The deployment of the booms is in charge of the following components:

- Two hinges based on torsion springs;
- One rotary actuator based on hybrid stepper motor + Harmonic Drive.

The boom mass budget is presented in Table 10. All masses in this Table include a maturity margin.

Figure 31 shows the proposed deployment sequence. The deployment concept uses elements with high TRL due to previous flight experience. However some criticalities of the technology are identified associated to:

- Launch lock of deployable large mass (80 kg) directly attached to the S/C and with interface with the deployment boom;
- Release compatibility with deployment direction;
- Deployment of large inertia;
- Induced torques to the S/C;
- Verification on ground.

The foreseen development activity to reach TRL 6 by the time of mission adoption is presented in Sect. 6.5.

5.6 Technology readiness

The proposed platform architecture is based on commercially available spacecrafts. Table 11 summarizes the technology readiness. All the involved subsystems are based on off-the-shelf products, with the exception of the deployable boom, which, nonetheless, will use elements of high TRL due to previous flight experience (Rosetta, ARTEMIS, Spot 4, GAIA).

Table 11: Technology Readiness Levels for the All-Sky-ASTROGAM platform and deployable boom.

S/S	TRL	Description
OBDH	9	Off-the-shelf
Power S/S	9	Off-the-shelf
Solar panel	9	Custom made based on TRL9 solar panels with triple junction GaAs cells
AOCS	9	Off The Shelf
TM & TC I/F	9	Off The Shelf
Thermal Control	9	Custom made based on TRL9 Technologies well proven in flight missions
Mech. structure	> 7	Modular design based on flight proven structural elements.
Deployable Boom	5	The proposed deployment concept uses elements (hinges, HDRM, rotary actuators) with high TRL due to previous flight experience.

5.7 System budgets

Table 12 shows the spacecraft power budget with 20% system margin. The spacecraft consumption in nominal science operation is 671 W. Table 13 shows the satellite mass budget including maturity margins at sub-system level and an additional system margin of 20%. The mass budget of the gamma-ray imager is presented in Table 5 and that of the deployable boom is Table 10. The spacecraft mass budget includes the resources required for de-orbiting at the end of the mission lifetime.

A data budget is shown to evaluate the required data rate in downlink and to size the on-board mass memory capacity. The average data generation of both P/L and platform is summarized in Table 14. After a data compression by a factor of 2.6 (as obtained with All-Sky-ASTROGAM representative science data and standard compression programs), the overall data generation rate is about 335 kbps, that is 3.6 Gbytes per day. The 32 Gbytes mass memory of the SSR enables to record scientific data acquired for more than five days.

Table 12: All-Sky-ASTROGAM satellite power budget.

EQUIPMENT	Power (W)
PLATFORM	with mat. margin
AOCS	53.0
Power S/S	25.0
OBDH	67.0
TM/TC	35.0
Propulsion	1.0
Thermal Control	115.0
PAYLOAD	with mat. margin
Gamma-ray imager	140.4
Tracker, Calorimeter & AC BEEs	24.0
PDHU	18.0
PSU	60.0
Harness & PCU losses	21.0
Total Power	559.4
System margin 20%	111.9
Total Power Including Margin	671.3

Table 13: All-Sky-ASTROGAM satellite mass budget.

EQUIPMENT	Mass [kg]			
	Design	Margin		Total
PLATFORM				
AOCS	51	10%	5	56
Power S/S	41	10%	4	45
OBDH	29	10%	3	32
TM/TC	30	10%	3	33
Structure	290	20%	58	348
Harness	27	10%	3	30
Propulsion	18	10%	2	20
Thermal Control	14	10%	1	15
Deployable Boom with mat. margin				31
PAYLOAD				
Gamma-ray imager with mat. margin				78
P/L PSU, PDHU and BEE units with mat. margin	25	20%	5	30
SATELLITE DRY MASS				718
System margin 20%				144
SATELLITE DRY MASS WITH SYSTEM MARGIN				861
Propellant				30
SATELLITE MASS AT LAUNCH (WET MASS)				891

Table 14: All-Sky-ASTROGAM satellite telemetry budget.

	Average acquisition rate
Platform Housekeeping (including star tracker, GNSS data and PUS report TM)	10.0 kbps
Payload data	699.3 kbps
Payload data compression factor	2.6
Compressed payload data	269.0 kbps
Total acquisition rate	279.0 kbps
Margin 20%	55.8 kbps
Total with margin	334.8 kbps

Assuming a rate of downlink in X-band of 8 Mbps to one of the 35-meter diameter antennas of the ESTRACK station network (Cebreros, Malargüe, New-Norcia), the science data download can be performed with a passage duration of about 1.0 hour per day. Visibility analysis for a typical halo orbit shows that the average duration of spacecraft visibility by one of these three stations is of the order of 10 hours per day. The downlink of the All-Sky-ASTROGAM data would thus use about 10% of the available visibility time for one station, or about 3% if the three stations are used. The spacecraft RF link budget is presented in Table 15.

Table 15: All-Sky-ASTROGAM satellite RF link budget.

Link parameters	Units	Des	Adv	Fav	AVG	VAR	Notes	Source
S/C altitude	Km	1500000.0	1500000.0	1500000.0	1500000.0	0.0		
Elevation angle	°	10.0	10.0	10.0	10.0		Minimum considered	
Slant Range	Km	1505257.5	1505257.5	1505257.5	1505257.5			Computation
Downlink frequency	MHz	8500.0	8500.0	8500.0	8500.0	0.0		Heritage
S/C RF power	W	4.0	3.5	4.0	3.8	0.0	at SSPA OUT	Heritage
S/C antenna gain	dBi	37.0	36.5	37.0	36.8	0.0	Reflector diameter <1m	Heritage
S/C circuit losses	dB	1.5	1.7	1.4	1.5	0.0		
S/C EIRP	dBW	41.5	40.2	41.6	41.1	0.0		Computation
TX implementation Losses	dB	2.0	2.5	2.0				Heritage
Free space losses	dB	234.6	234.6	234.6	234.6	0.0		Computation
Atm & rain losses	dB	0.5	0.9	0.4	0.6	0.0		Doc
Polarization loss combined (TX +RX)	dB	0.5	0.5	0.4	0.5	0.0		Computation
Total transmission losses	dB	237.6	238.5	237.4	235.7	0.0		
G/S antenna gain	dBi							
G/S antenna pointing loss	dB	0.0	0.0	0.0	0.0		Included in G/T	Doc
Receiver Implementation Losses	dB	2.5	2.5	2.5	0.0		Includes mod/demod	N/A
Ground Station G/T	dB/K	49.2	48.1	49.4	48.8	0.0	ESTRACK 35 m	Doc
C/No	dBHz	79.2	76.0	79.7	82.8	0.1		Computation
Eb/No @ Ground		7.2	3.9	7.7				
Data rate	Mbps	16.0	16.0	16.0	16.0			
BER req		0.0	0.0	0.0	0.0			
Eb/No req OQPSK+Viterbi rate 1/2	dB	5.6	5.6	5.6	5.6			
C/No req	dBHz	77.6	77.6	77.6	77.6			Computation
MARGIN DOWNLINK	dB	1.6	-1.7	2.1	5.2	0.1		
VAR	0.1							
Margin Mean - 3σ	4.5							
W.C. RSS Margin	-0.3							

5.8 Ground segment

5.8.1 Mission Control Center and ground stations

The All-Sky-ASTROGAM satellite will be managed by an ESA Mission Control Center (MOC). Standard operations and activities will be performed by the MOC (satellite control, flight dynamics, mission planning). The ESA tracking station network (Estrack) will be used to communicate with the spacecraft. No specific requirements are envisioned regarding satellite telemetry, tracking and command. The MOC will be in charge of **(i)** commanding the instrument and spacecraft; **(ii)** mission planning; **(iii)** flight dynamics; **(iv)** instrument and satellite health monitoring; **(v)** telecommand and telemetry (TM) history; **(vi)** spacecraft TM management; **(vii)** auxiliary data production (attitude reconstruction, time calibration, orbit reconstruction) and transmission to the SOC; **(viii)** scientific TM acquisition and transmission to the SOC.

5.8.2 Scientific ground segment

The All-Sky-ASTROGAM scientific ground segment consists of a Science Operations Center (SOC) and a Science Data Center (SDC).

Science Operations Center (SOC) — The SOC is to be located in an ESA facility under ESA supervision. It is the official interface among the MOC, the SDC, and the scientific community (users and guest observers). The SOC is in charge of: **(i)** TM acquisition from the MOC; **(ii)** scientific mission planning, including management of Target of Opportunities; **(iii)** running data pre-processing (from level L0 to L1); **(iv)** running quick-look analysis; **(v)** issuing scientific alerts (GRBs, transient sources, TGFs); **(vi)** managing the Guest Observer programme (including scientific tool delivery); **(vii)** managing the science data archive. The SOC is coordinated by ESA, which enacts the planning/operational decisions regarding the mission.

Science Data Center (SDC) — The SDC will be based on both ESA and Science Team contributions. The SDC is in charge of **(i)** L1 data acquisition from the SOC; **(ii)** running data pipeline and data reduction (from L1 to L2); **(iii)** instrument monitoring and support to payload diagnostic; **(iv)** instrument calibration and calibration archive; **(v)** final stage of scientific software development and testing; **(vi)** development of scientific products and data analysis (imaging, lightcurves, spectral and temporal analysis, etc.); **(vii)** production of tools for quick-look analysis

and alert generation; **(viii)** production and validation of Guest Observer analysis tools.

The All-Sky-ASTROGAM scientific ground segment will use a sophisticated data reduction and analysis system that merges the Compton and the pair production regimes. It will be based on advanced techniques of pattern recognition for the classification of different event topologies originated by two interaction processes. The All-Sky-ASTROGAM Consortium team will be in charge of developing, testing and SDC implementation of the main SW tools and data analysis algorithms.

5.8.3 Data policy, Guest Observer programme, scientific mission planning

The All-Sky-ASTROGAM scientific program will be open to the international community through a Guest Observer (GO) programme. A science management plan will regulate the programmatic activities between ESA, the All-Sky-ASTROGAM team and the scientific community. All-Sky-ASTROGAM will operate as an observatory, and standard guidelines will be applicable. The mission will be operated by ESA following its standard rules in term of Announcement of Opportunities, data right, data distribution, etc. Hundreds of sources will be made available for GO investigations, following the operational examples of *INTEGRAL*, *AGILE* and *Fermi*.

We envision the implementation of a core science programme that should guarantee that the mission key objectives are met. In particular: **(i)** a performance verification phase is foreseen at the beginning of the operations, then a fraction of the observing time will be routinely reserved for in-flight calibrations. All these data will be available to the community after they have been validated by the Collaboration and the SOC. **(ii)** Mission planning will be regulated by a Mission Planning Committee following the indications of a Users' Committee. **(iii)** All data will become public after 1 year of proprietary right. **(iv)** Guest Observers will be supported by the All-Sky-ASTROGAM Science Data Center with data and analysis software.

6 Management Scheme

The management of the All-Sky-ASTROGAM Consortium is aimed at developing the Scientific Instrument and the mission flight segment and ground segment, and performing the related science activities. The management structure is organized with (i) the Lead Proposer, (ii) the All-Sky-ASTROGAM Science Board (SB), (iii) the All-Sky-ASTROGAM Project Office (PO), (iv) the Project Scientist, (v) the Instrument development coordinators, and (vi) the Science Team.

The Lead Proposer (LP), supported by his funding agency, will manage the formal interface with ESA and be the Chairman of the All-Sky-ASTROGAM SB. The SB is constituted of the LP, the detector/sub-system coordinators, and the coordinators of the scientific working groups. The SB will be in charge of coordinating all activities related to the development and scientific work of the mission.

The PO will be composed of both Consortium representatives and industrial partners. A Program Manager (PM) will be assigned to the PO coordination, and will be in charge of periodically reporting to the SB the technical activities. In addition, a Project Scientist is foreseen to facilitate the interface between the Science Team and the Instrument development coordinators.

6.1 Instrument development group

The All-Sky-ASTROGAM Instrument development is based on activities of several European groups as summarized in Table 16. Strong scientific collaboration is also going on with several teams in the US, Russia and Japan.

6.2 Product tree and Work Breakdown Structure

The product tree of the All-Sky-ASTROGAM mission is summarized in Figure 32, where the main sub-systems are clearly indicated. The work breakdown structure of the payload is shown in Figure 33. The involvement/responsibilities of the participating countries are indicated by nation

Table 16: All-Sky-ASTROGAM instrument development team.

Institutions	Countries	Main activities	Main participants
INFN, INAF, Univ. Padova, Univ. and Politecnico Bari, Univ. Roma Tor Vergata, Univ. Siena, Univ. Udine, Univ. Trieste	Italy	PI-ship, Mission and scientific coordination. P/L Management. Management, trigger simulations, manufacturing and AIT of the Si Tracker. Test, trigger simulations and calibration of the Calorimeter detectors and FEE (SDDs) development. Contribution to Science Data Center. Science activities.	A. De Angelis, G. Ambrosi, B. Babussinov, M. Boezio, V. Bonvicini, F. Gargano, F. Longo, M. N. Mazziotta, A. Morselli, P. Lubrano, R. Rando, A. Vacchi, A. Argan, A. Bulgarelli, C. Labanti, M. Marisaldi, M. Tavani, D. Bastieri, G. Busetto, M. Doro, M. Mariotti, N. Giglietto, F. Giordano, F. Loparco, P. Spinelli, A. Morselli, R. Paoletti
CEA/Irfu, CSNSM, APC, IPNO, LLR, CENBG, LUPM, IRAP	France	Si Tracker and Calorimeter FEE. Contribution to Si Tracker and Calorimeter detector manufacturing. P/L calibration activities. Contribution to Science Data Center. Science activities.	O. Limousin, A. Meuris, I. Grenier, V. Tatischeff, C. Hamadache, J. Kiener, P. Laurent, R. Terrier, N. de Séreville, D. Bernard, S. Fegan, T. Reposeur, F. Piron, P. von Ballmoos.
Univ. Mainz, KIT/IPE, RWTH Aachen, Univ. Erlangen, Univ. Postdam, Univ. Würzburg, MPE, TU Dortmund	Germany	Management, manufacturing & AIT of the Calorimeter. Calorimeter back-end electronics. Tracker back-end electronics. On-board data handling. P/L calibration activities. End-to-end simulations. Contribution to Science Data Center. Science activities.	U. Oberlack, C. Sfienti, N. Berger, M. Alfonsi, A. Brogna, Q. Weitzel, M. Hoek, B. Sprück, M. Thiel, M. Weber, M. Kleifges, M. Balzer, S. Funk, J. Wilms, Th. Bretz, M. Pohl, K. Mannheim, R. Diehl, D. Elsässer.
Univ. Barcelona, IMB-CNM (CSIC), ICE (CSIC), IFAE-BIST, PIC, CLPU, Univ. Salamanca, Univ. Complutense Madrid	Spain	Manufacturing, testing & characterization of the Si Tracker detectors. Development and testing of Calorimeter and AC detectors. P/L thermal control. Tracker FEE development and testing. Tracker BEE development and testing. Data Handling development. P/L calibration support. Science activities.	J. Rico, M. Hernanz, J. Isern, J. L. Gálvez, M. Lozano, M. Ullán, G. Pellegrini, J.M. Paredes, D. Gascón, M. Martínez, M. Delfino, J.M. Alvarez, L. Roso, J.A. Barrio, A. Dominguez, M.V. Fonseca, J. Trenado
DPNC Univ. Geneva, Astron. Department, Univ. Geneva, PSI	Switzerland	Co-leadership of Silicon Tracker development. Manufacturing and AIT of the Si Tracker. Characterization & calibration of Si Tracker detectors. EGSE. Polarized photon beam test. P/L calibration activities. Science Data Center. Science activities.	X. Wu, M. Pohl, P. Azzarello, F. Cadoux, M. Cole, R. Walter, W. Hajdas.
KTH and Univ. Stockholm	Sweden	Manufacturing & AIT of the Anticoincidence system. General reconstruction & calibration activities. Science activities.	M. Pearce, F. Ryde, J. Larsson, J. Conrad, L. Bergström, T. Linden.
Space Research Center of PAS, Warsaw	Poland	PDHU, PSU design, manufacturing, testing and integration with S/S and instrument.	P.Orleański, W. Nowosielski
Univ. College Dublin & Dublin City University	Ireland	Co-leadership of Calorimeter development. Manufacturing of Calorimeter detectors. P/L calibration activities. Science activities.	L. Hanlon, S. McBreen, M. Chernyakova
DTU	Denmark	Characterization & calibration of Si Tracker detectors. P/L calibration activities. Science activities	I. Kuvvetli, S. Brandt, C. Budtz-Jørgensen, A. Hornstrup, N. Lund
LIP University of Coimbra IST University of Beira Interior	Portugal	Calorimeter detector manufacturing. Contribution to Calorimeter. Experimental and simulated polarimetric characterisation of Si Tracker and Calorimeter detectors. Detectors' radiation hardness testing and simulation	R.M. Curado da Silva, J. M. Maia, P. Gonçalves, A. Cortez, H. Neves, G. Canezin

flags. Figure 33 shows explicitly the roles of the instrument team. Industrial activities will include the instrument project office, AIV, and support to the development of the sub-systems.

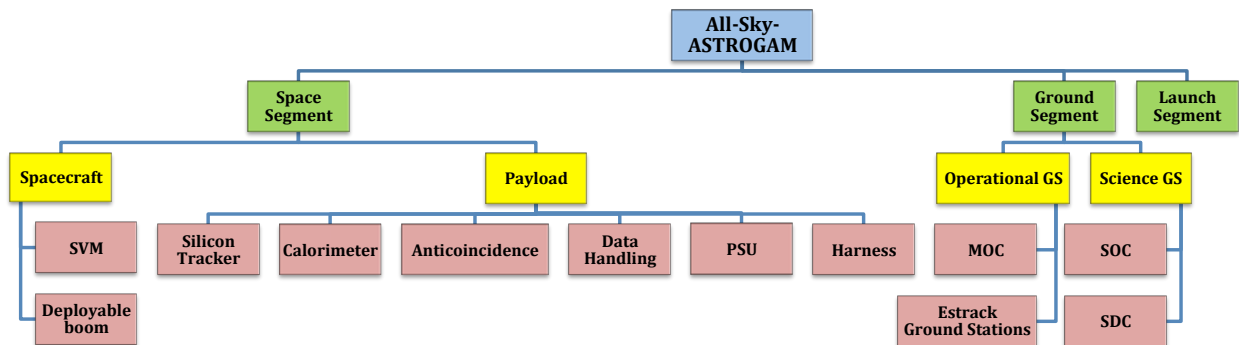


Figure 32: All-Sky-ASTROGAM product tree.

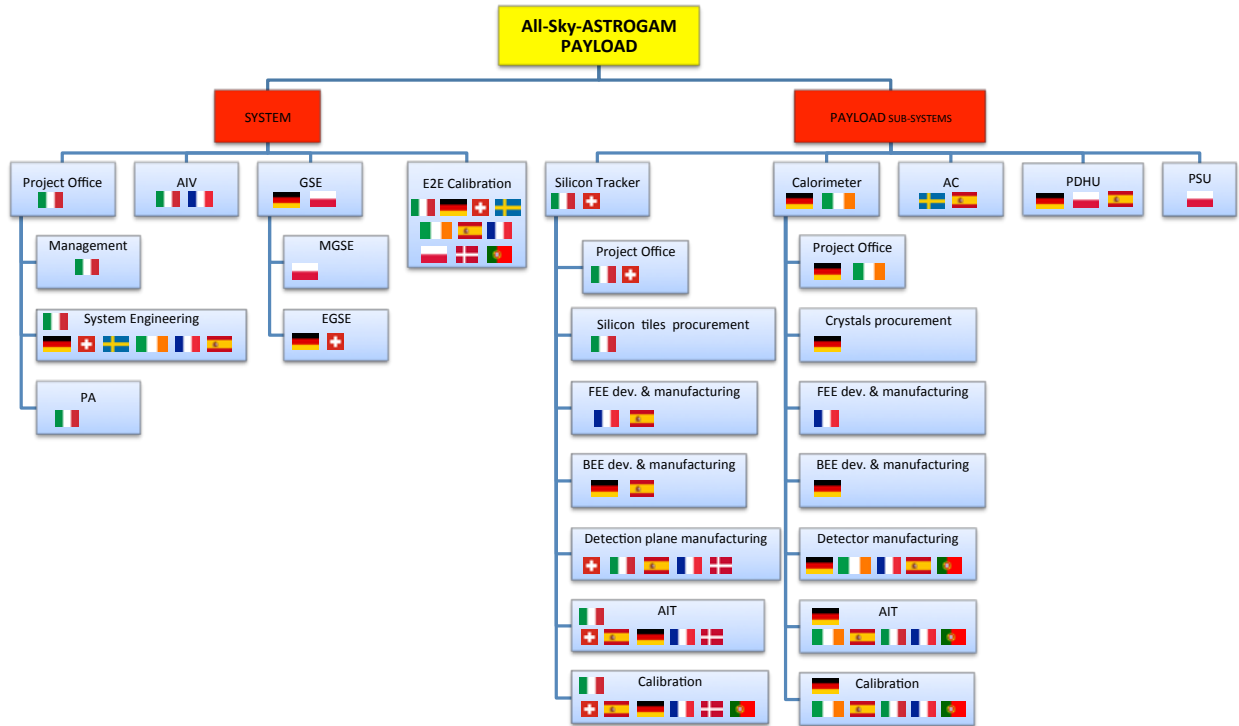


Figure 33: AllSky-ASTROGAM Work Breakdown Structure.

6.3 Procurement Scheme

Taking into account the reduced envelope of the All-Sky-ASTROGAM Instrument, the procurement of all the selected components is not considered a critical issue. Here below the proposed procurement scheme of the main Instrument parts.

Double-sided silicon detectors. The number of Si tiles required for the flight model is 450. Considering the detectors needed to implement the prototypes, the development models and the spare detectors, the total number of DSSDs to be procured will be of the order of 700. Possible manufacturers operating on the field and well within the productive capability are Hamamatsu, FBK, and IMB-CNM (CSIC); note that 1200 Si tiles of the same size were produced in one year for DAMPE by HAMAMATSU. These companies have relevant heritage on the manufacturing of Si detectors for space applications and mass production (Hamamatsu for the *Fermi* mission, FBK for the AMS-02 mission, and CNM for the LHC/ATLAS experiment at CERN). No specific technology development will be requested with respect to the already used components.

Silicon Tracker and Calorimeter FEE ASIC. In order to optimize the Instrument development, we envisage to use the same readout ASIC with different input stages for both the Tracker and the Calorimeter. The FM of the Tracker FEE will need 3600 ASICs of 32 channels each for its readout. The FM of the Calorimeter FEE will need 100 ASICs of 32 channels each for its readout. Taking into account the other models and contingencies, we estimate that 5000 ASICs will be necessary in total. We foresee the selection of the Idef-X BD ASICs for the Tracker and the Idef-X HD ASICs for the Calorimeter, which have been already conceived, tested and qualified by CEA. The ASICs would be produced by the AMS company, which has a very long heritage in mass production. The production and backend process of this ASIC would be under the coordination of CEA, which has, for instance, already controlled the process of production of the nearly 6,000 space qualified ASICs necessary for the *INTEGRAL*/IBIS ISGRI instrument.

Calorimeter Crystals. CsI(Tl) is a well known scintillator that has already been used for several high-energy astronomy missions (e.g. 4096 crystals in *INTEGRAL*/PICsIT). The number of CsI(Tl) bars required for the FM of All-Sky-ASTROGAM is 784, which has to be extended to about 1500 when considering prototyping and development. Possible manufacturers operating on the field are Saint-Gobain Crystals and Detect Europ (Amcrys).

Calorimeter Silicon drift detectors. SDDs will be designed by INFN Trieste and fabricated by FBK, Trento, which has a 6" wafer production line available and mass production capabilities, as demonstrated within the assessment phase of the LOFT M3 mission. The overall SDD Silicon area required, accounting for spare components and device production yield, is compatible with 23 Si wafers of 6".

6.4 Model philosophy and schedule

All-Sky-ASTROGAM will be developed envisioning the following steps/models for the Payload: (i) a demonstration model aimed at validating the Instrument concept by mission adoption; (ii) a structural & thermal model (STM); (iii) an engineering model (EM); (iv) a functional model of the Data Handling; and (v) the proto-flight model (PFM). For the deployable boom, we foresee a PFM development approach with the addition of a demonstration model aimed at proving the TRL 6 by the mission adoption (see Sect. 6.5 below). For the service module (SVM), we propose a standard PFM development approach.

The mission master schedule is shown in Figure 34.

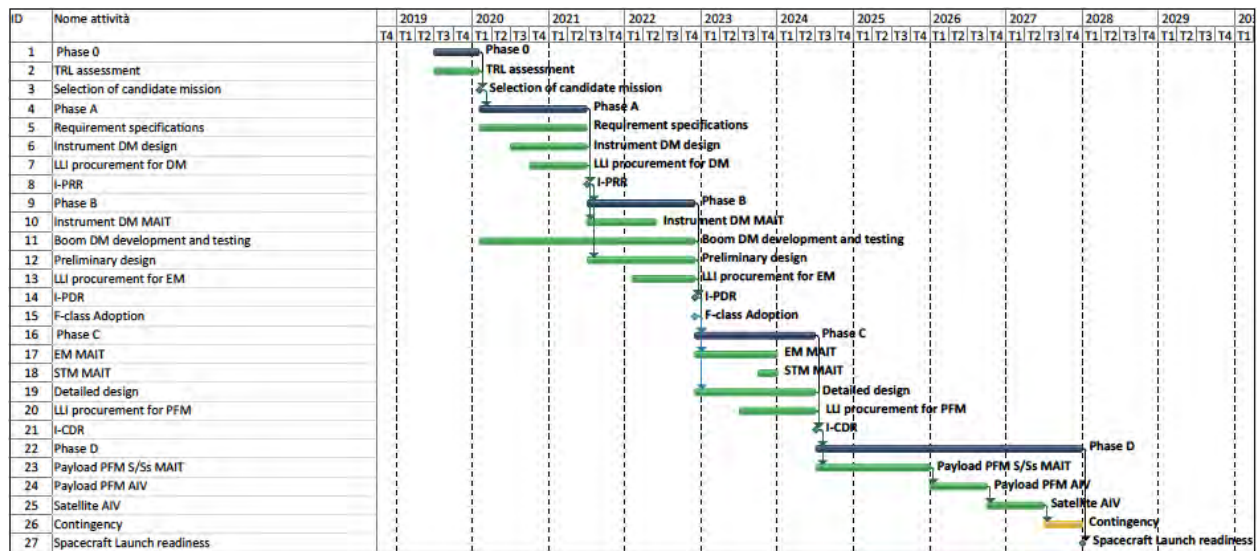


Figure 34: All-Sky-ASTROGAM master schedule

Following the proposed development approach, all the P/L sub-systems and units will be ready for the Payload AIV by end of 2025. The All-Sky-ASTROGAM satellite will be ready for the launch by end of 2027 with a contingency of 6 months.

6.5 Technology development activity for the deployable boom

All the technologies involved in the mission have $TRL \geq 5$ except for the deployable boom for which we propose a development plan aimed at reaching the requested maturity by the time of mission adoption (end 2022). The technology development activity for the deployable boom aims at:

- Demonstrating Hold down concept of large payloads compatible with deployment trajectory;
- Characterizing expected disturbances on S/C during deployment on different deployment steps;
- Characterizing tip position-orientation after deployment;
- Defining ground verification procedures and tools.

For the achievement of the TRL 6 a dedicated Demonstration Model (DM) is proposed to be built and tested. This DM will be focused on the verification of the compatibility of the holding of a high mass payload with the functional requirements of a deployable boom attached to it. Therefore it is proposed to include the following components:

- Representative hold-down and release mechanisms (HDRMs) to support a dummy payload of 80 kg;
- Structural and functional representative masts to reproduce the launch constraints and the interface to the payload to verify release;
- Representative hinges (2 units);
- Representative rotary actuator.

The model will be used to demonstrate release (with payload and boom constraints), deployment with large inertia and ground verification. The DM will include a payload subassembly, which will be composed of the following items (see Fig. 35):

- Payload simulating the dummy mass;
- HDRMs 2, 3 and 4 (see Fig. 30);
- Boom segment connecting the payload dummy with HDRM2.

This model will be used to demonstrate the structural behavior and the boom release compatibility after vibration and TV environment in order to achieve TRL 6.

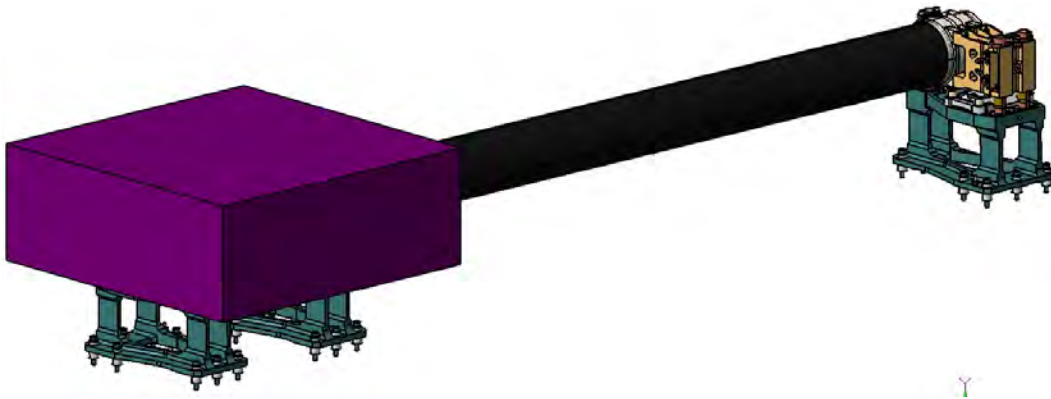


Figure 35: 3D picture of the payload subassembly that will be developed to achieve a TRL of 6 for the deployable boom.

7 Costing

We propose a cost sharing of the All-Sky-ASTROGAM mission between ESA and national funding agencies. ESA will provide the Service Module, the Ariane 6.2 launcher and adapter (co-passenger to the ARIEL mission), launch services, the Ground Segment (MOC, SOC and part of the SDC), and management. The All-Sky-ASTROGAM national funding agencies (currently including Italy, France, Germany, Switzerland, Spain, Sweden, Poland, Ireland, Denmark, and Portugal) will provide the scientific payload and a contribution to the SDC.

Table 17 summarizes the ESA expected cost at completion. The cost of the platform has been estimated by OHB from the list of the SVM elements, which are all off-the-shelf products used in commercially available spacecrafts. The cost of the deployable boom has been evaluated by SENER based on the consolidated cost of the space-proven elements used for its design. Tables 18 summarizes the expected involvement of national groups supported by their funding agencies for the P/L development and operational support. Cost evaluation is based on explicit quotations, previous direct experience of our group, and agency assessments.

Table 17: All-Sky-ASTROGAM cost at completion for ESA.

Activity	Cost (million €)	Notes
1. ESA Project Office	16	15% of ESA cost for items 2 – 5
2. System activities and Platform	80	
3. Deployable boom	5	
4. Launch	0	Co-passenger to the ARIEL M mission
5. Ground Segment & Operations	20	
6. Contingency	12	10% of ESA cost for items 1 – 5
Total cost for ESA	133	

Table 18: Contribution to All-Sky-ASTROGAM P/L development by national agencies.

Sub- Systems	Cost (million €)	Programmatic involvement
P/L System	5	Italy, Germany, France, Switzerland, Spain, Sweden, Poland, Ireland, Denmark, Portugal
Tracker	9	Italy, Switzerland, France, Germany, Spain, Denmark, Portugal
Calorimeter	3	Germany, Ireland, France, Italy, Spain, Portugal
Anticoincidence	1.5	Sweden, Spain
Data Handling & Power Supply	1.5	Germany, Poland, Spain
TOTAL P/L:	20	
Operational Support	5	All

References

- [1] Aartsen, M.G., et al. (IceCube collaboration), 2013, *Science*, 779, 132
- [2] Aartsen, M.G., et al. (IceCube, Fermi-LAT, MAGIC Collaborations et al.), 2018, *Science*, 361, 6398
- [3] Aartsen, M. G., et al. (IceCube collaboration), 2018, *Science*, 361, 147
- [4] Aartsen, M.G., et al. (IceCube collaboration), 2016, *ApJ*, 824, 115
- [5] Aartsen, M.G., et al. (IceCube collaboration), 2017, *ApJ*, 835, 45
- [6] Abbott, B. P., et al. (LVC), 2016, *Living Reviews in Relativity*, 19, 1
- [7] Abbott, B.P., et al., 2017, *ApJ Lett.*, 848, L12
- [8] Abbott, B.P., et al., 2017, *APJ Lett.*, 848, L13
- [9] Abbott, B. P., Abbott, R., Abbott, T. D., et al., 2017, *Phys. Rev. Lett.*, 119, 161101
- [10] Abdo, A.A., et al., 2009, *Science*, 326, 1512
- [11] Ackermann, M., Ajello, M., Albert, A., et al. 2014, *Science*, 345, 554
- [12] Ackermann, M., et al. 2015, *ApJ*, 799, 1
- [13] Ahangarianabhari, M., Macera, D., Bertuccio, G., Malcovati, P., & Grassi, M., 2015, *Nucl. Instr. Methods in Phys. Res. A*, 770, 155
- [14] Ahlers, M., Halzen F., 2015, *Rep. Prog. Phys.*, 78, 126901
- [15] Ajello, M., Costamante, L., Sambruna, R.M., et al., 2009, *ApJ*, 699, 603
- [16] Ajello, M., et al., 2012, *ApJ*, 751, 108
- [17] Albert, A., et al. (ANTARES collaboration), 2017, *JCAP*, 04, 19
- [18] Ansoldi, S., et al. (MAGIC collaboration), 2018, *ApJ Lett.*, 863, L10
- [19] Bagliesi, M.G., Avanzini, C., Bigongiari, C., et al., 2011, *Nucl. Phys. B Proc. Suppl.*, 215, 344
- [20] Barnes, J., et al., 2016, *ApJ*, 829, 110
- [21] Bechtol, K., et al., 2017, *ApJ*, 836, 47
- [22] Berger, E., 2014, *ARA&A*, 52, 43
- [23] Berlin, T. H., Madansky, L., 1950, *Physical Review*, 78, 623
- [24] Band, D., Matteson, J., Ford, L., et al. 1993, *ApJ*, 413, 281
- [25] Bildsten, L., Salpeter, E. E., & Wasserman, I., 1993, *ApJ*, 408, 615
- [26] Bulgarelli, A., Fioretti, V., et al., 2012, *Proc. SPIE*, 8453, 845335
- [27] Cumani, P., Hernanz, M., Kiener, J., Tatischeff, V., & Zoglauer, A., 2019, *Experimental Astronomy* online. <https://doi.org/10.1007/s10686-019-09624-0>. arXiv:1902.06944
- [28] De Angelis, A., Tatischeff, V., Tavani, M., Oberlack, U., et al., on behalf of the e-ASTROGAM Collaboration, 2017, The e-ASTROGAM mission (exploring the extreme Universe in the MeV-GeV range), <https://arxiv.org/abs/1611.02232>, DOI: 10.1007/s10686-017-9533-6, *Experimental Astronomy*, 44, 25
- [29] De Angelis, A., Tatischeff, V., Grenier, I., McEnery, J., Mallamaci, M., et al., 2018, *Science with e-ASTROGAM*, <https://arxiv.org/abs/1711.01265>, *J. High Energy Astrophysics*, 19, 1
- [30] De Angelis, A., Pimenta, M., 2018, *Introduction to Particle and Astroparticle Physics: Multimessenger Astronomy and its Particle Physics Foundations*, Springer Nature, Heidelberg, <https://link.springer.com/book/10.1007%2F978-3-319-78181-5>
- [31] Fong, W., et al., 2014, *ApJ*, 780, 118
- [32] Forot, M., Laurent, P., Grenier, I. A., Gouiffès, C., & Lebrun, F. 2008, *ApJ*, 688, L29

- [33] Gatti, E., & Rehak, P. 1984, Nucl. Instr. Methods in Phys. Res. A, 225, 608
- [34] Götz, D., Laurent, P., Antier, S. et al. 2014, MNRAS, 444, 2776
- [35] GCN IceCube EHE 50579430_130033
- [36] Gevin, O., Lemaire, O., Lugiez, F., et al. 2012, Nucl. Instr. Methods in Phys. Res. A, 695, 415
- [37] Ghisellini, G., Lazzati, D., 1999, MNRAS, 309, 7
- [38] Ghisellini, G., Della Ceca, R., Volonteri, M., et al., 2010, MNRAS, 405, 387
- [39] Ghisellini, G., Haardt, F., Della Ceca, R., Volonteri, M., Sbarrato, T., 2013, MNRAS, 432, 2818
- [40] Goldstein, A., et al., 2017, ApJ, 846, 5
- [41] Granot, J., 2002, ApJ, 570, 61
- [42] Herschel Observers' Manual HERSCHEL-HSC-DOC-0876, Post-Operation Version 5.0.3, <http://herschel.esac.esa.int/Docs/Herschel/html/Observatory.html>
- [43] Hotokezaka, K., et al., 2016, MNRAS, 459, 35
- [44] ISO15390 (ISO-TC, 2004) ISO Technical Committee 20/SC 14, Space environment (natural and artificial) - Galactic cosmic ray model -2004
- [45] Jenke, P.A., et al., 2016, ApJ, 826, 228
- [46] Jiggins, P., Varotsou, A., Truscott, P., et al. 2018, IEEE Trans. on Nucl. Science, 65, 698
- [47] Kanbach, G., Andritschke, R., Zoglauer, A., et al. 2005, Nucl. Instr. Methods in Phys. Res. A, 541, 310
- [48] Kiener, J., Gros, M., Tatischeff, V., et al. 2004, Nucl. Instr. Methods in Phys. Res. A, 519, 623
- [49] Kim, S., et al., 2017, ApJ Lett., 850, L21
- [50] Koljonen, K., et al., 2010, MNRAS, 406, 307
- [51] Krauss, F., et al., 2014, A&A, 566, L7
- [52] Labanti, C., Marisaldi, M., Fuschino, F., et al. 2008, Proc. of the SPIE, 7021, 702116
- [53] Limousin, O., Gevin, O., Lugiez, F., et al. 2005, IEEE Trans. on Nucl. Science, 52, 1595
- [54] Marisaldi, M., Labanti, C., Soltau, H., et al. 2005, IEEE Trans. on Nucl. Science, 52, 1842
- [55] Mirzoyan, R., for the MAGIC collaboration, 2017, Astronomer's Telegram, 10817
- [56] Moiseev, A. A., Hartman, R. C., Ormes, J. F., et al. 2007, Astroparticle Physics, 27, 339
- [57] Murase, K., et al., 2016, Phys. Rev. Lett., 116, 71101
- [58] Nissanke, S., et al., 2013, ApJ, 767, 124
- [59] Paciesas, W. S., Meegan, C. A., Pendleton, G. N., et al. 1999, ApJ Suppl., 122, 465
- [60] Paiano, S., et al., 2018, ApJ Lett., 854, L2
- [61] Patricelli, B., et al., 2016, JCAP, 11, 56
- [62] Perinati, E., Tenzer, C., Santangelo, A., et al. 2012, Experimental Astronomy, 33, 39
- [63] Perotti, F., Fiorini, M., Incorvaia, S., Mattaini, E., & Sant'Ambrogio, E. 2006, Nucl. Instr. Methods in Phys. Res. A, 556, 228
- [64] Phillips, M. M. 1993, ApJ, 413, L105
- [65] Piano, G., et al., 2012, A&A, 545, A110
- [66] Rachevski, A., Zampa, G., Zampa, N., et al. 2014, Journal of Instrumentation, 9, P07014
- [67] Romero, G. E., Vieyro, F. L., & Chaty, S. 2014, A&A, 562, L7
- [68] Roques, J. P., Schanne, S., von Kienlin, A., et al. 2003, A&A, 411, L91

- [69] Roques, J.P., et al., 2015, *ApJ Letters*, 813, L22
- [70] Santander, M., et al., 2017, *PoS, (ICRC2017)*, 618
- [71] Savchenko, V., Ferrigno, C., Kuulkers, E., et al., 2017, *ApJ*, 848, L5
- [72] Senno, N., et al., 2016, *Phys. Rev. D*, 93, 83003
- [73] Siebert, T. et al. 2016, *Nature*, 531, 341
- [74] Tagliaferri, G., Ghisellini, G., Perri, M., et al., 2015, *ApJ*, 807, 167
- [75] Takami, H., Kyutoku, K., & Ioka, K., 2014, *Phys. Rev. D*, 89, 63006
- [76] Tanaka, Y., Buson, S., Kocevski, D., for the Fermi-LAT collaboration, 2017, *Astronomer's Telegram*, 10791
- [77] Tatischeff, V., De Angelis, A., Gouiffès, C. et al. 2018, *JATIS*, 4, 11003
- [78] Tavani, M., et al., 2009, *A&A*, 502, 995
- [79] Tavani, M., Tatischeff, V., von Ballmoos, P., et al., 2014, proposal for the M4 ESA call
- [80] van Eerten, H.J., & A.I. MacFadyen, 2012, *ApJ*, 751, 155
- [81] Volonteri, M., et al., 2011, *MNRAS*, 416, 216
- [82] Zdziarski, A. A., Stawarz, L., Pjanka, P., & Sikora, M. 2014, *MNRAS*, 440, 2238
- [83] Zhang, H., Boettcher, M. 2013, *ApJ*, 774, 18
- [84] Zoglauer, A., Andritschke, R., & Schopper, F. 2006, *New Astronomy Reviews*, 50, 629

Annex 1: List of some core team members

A. De Angelis	INFN & INAF Padova; Univ. Udine and Padova, Italy; LIP/IST Lisboa, Portugal
V. Tatischeff	CSNSM, CNRS and University of Paris Sud, Orsay, France
M. Tavani	INAF/IAPS, Roma, Italy
U. Oberlack	Institute of Physics and PRISMA Excellence Cluster, University Mainz, Germany
R. Walter	University of Geneva, Switzerland
G. Ambrosi	INFN Perugia, Italy
A. Argan	INAF Headquarters, Roma, Italy
P. von Balmoos	IRAP Toulouse, France
S. Brandt	DTU Space, National Space Institute, Technical University of Denmark
A. Bulgarelli	INAF/OAS-Bologna, Italy
A. Bykov	Ioffe Institute, St. Petersburg, Russia
V. Fioretti	INAF/OAS-Bologna, Italy
I.A. Grenier	Laboratoire AIM, CEA-IRFU/CNRS/Univ. Paris Diderot, C.E.A. Saclay, France
L. Hanlon	School of Physics, University College Dublin, Ireland
D. Hartmann	Department of Physics and Astronomy, Clemson University, USA
M. Hernanz	Institute of Space Sciences (CSIC-IEEC), Campus UAB, Barcelona, Spain
G. Kanbach	Max-Planck-Institut für Extraterrestrische Physik, Garching, Germany
I. Kuvvetli	DTU Space, National Space Institute, Technical University of Denmark
P. Laurent	Lab. APC, CEA/DRF CNRS, Univ. Paris Diderot, Paris, France
M.N. Mazziotta	INFN Bari, Italy
J. Mc Enery	NASA Goddard Space Flight Center, MD, USA
S. Mereghetti	INAF/IASF, Milano, Italy
A. Meuris	CEA Saclay, DRF/IRFU/DAP/LSAS, France
A. Morselli	INFN Roma “Tor Vergata”, Italy
K. Nakazawa	Department of Physics, University of Tokyo, Japan
M. Pearce	Physics Department, Royal Institute of Technology (KTH), Stockholm, Sweden
R. Rando	INFN Padova, Italy
J. Rico	IFAE-BIST, Edifici Cn. Universitat Autònoma de Barcelona, Spain
R. Curado da Silva	LIP, Departamento de Física Universidade de Coimbra, Portugal
X. Wu	University of Geneva, Switzerland
A. Zdziarski	Nicolaus Copernicus Astr. Center, Polish Academy of Sciences, Warszawa, Poland
A. Zoglauer	University of California at Berkeley, Space Sciences Laboratory, USA

We thank for the excellent cooperation Paolo Lorenzi, Mark Fittock, Danilo Morea, Floriano Venditti, Maria Lucia Tampellini, Rolf Janovsky from OHB, and Eduardo Ugoiti Bolumburu from SENER. We also acknowledge the contributions by André Laurens (CNES), Harald Ramarijaona (CSNSM), Paolo Cumani (CSNSM), Jordi Isern (ICE - CSIC/IEEC), S. Ciprini (INAF), L. Foffano (Univ. Padova).

Annex 2: Collaboration Members

A. De Angelis,^{1,2,3,4} V. Tatischeff,⁵ M. Tavani,^{6,7,8} U. Oberlack,⁹ R. Walter,¹⁰ L. Hanlon,¹¹ A. Argan,¹² P. Von Ballmoos,¹³ I. A. Grenier,¹⁴ A. Bulgarelli,¹⁵ A. Bykov,¹⁶ M. Hernanz,¹⁷ G. Kanbach,¹⁸ I. Kuvvetli,¹⁹ M. Pearce,²⁰ A. Zdziarski,²¹ G. Ambrosi,²² J. Conrad,²³ R. Curado da Silva,²⁴ G. Ghisellini,²⁵ A. Harding,²⁶ J. Isern,²⁷ M. Leising,²⁸ F. Longo,^{29,30} G. Madejski,³¹ M. Mallamaci,¹ J. McEnery,²⁶ M. N. Mazziotta,³² S. Mereghetti,³³ A. Morselli,⁸ J. M. Paredes,³⁴ M. Pohl,³⁵ R. Rando,^{1,36} M. Razzano,^{37,38} J. Rico,³⁹ S. Brandt,¹⁹ A. Aboudan,^{36,2} M. Ackermann,⁴⁰ A. Addazi,⁴¹ M. Ajello,²⁸ C. Albertus,⁴² J. M. Álvarez,⁴³ S. Antón,^{44,45} L. A. Antonelli,⁴⁶ A. Babic,⁴⁷ B. Baibussinov,¹ M. Balbo,¹⁰ L. Baldini,^{37,38} S. Balman,⁴⁸ C. Bambi,^{41,49} U. Barres de Almeida,⁵⁰ J. A. Barrio,⁵¹ R. Bartels,⁵² D. Bastieri,^{36,1,53} W. Bednarek,⁵⁴ L. Bergström,²³ D. Bernard,⁵⁵ E. Bernardini,^{56,40} T. Bernasconi,¹⁰ B. Bertucci,^{22,57} A. Biland,⁵⁸ E. Bissaldi,^{59,32} M. Boettcher,⁶⁰ V. Bonvicini,³⁰ V. Bosch-Ramon,³⁴ E. Bottacini,^{1,36} V. Bozhilov,⁶¹ T. Bretz,⁶² M. Branchesi,^{63,64} V. Brdar,⁶⁵ T. Bringmann,⁶⁶ A. Brogna,⁹ C. Budtz-Jørgensen,¹⁹ G. Busetto,³⁶ S. Buson,²⁶ M. Busso,^{22,57} A. Caccianiga,²⁵ S. Camera,^{67,68,69,70} R. Campana,¹⁵ G. Canezin,⁷¹ P. Caraveo,³³ M. Cardillo,⁶ P. Carlson,²⁰ S. Celestin,⁷² M. Cermeño,⁴² A. Chen,⁷³ C. C. Cheung,⁷⁴ E. Churazov,^{75,76} S. Ciprini,^{46,22} A. Coc,⁵ A. Coleiro,^{77,78} W. Collmar,⁷⁹ P. Coppi,⁸⁰ A. Cortez,⁷¹ S. Cutini,^{46,22} F. D'Ammando,⁸¹ B. De Lotto,⁸² D. de Martino,⁸³ A. De Rosa,⁶ M. Del Santo,⁸⁴ L. Delgado,¹⁷ R. Diehl,⁷⁹ S. Dietrich,⁸⁵ A. D. Dolgov,^{86,87} A. Domínguez,⁵¹ D. Dominis Prester,⁸⁸ I. Donnarumma,⁶ D. Dorner,⁸⁹ M. Doro,^{1,36} M. Dutra,⁹⁰ D. Elsaesser,⁹¹ M. Fabrizio,^{46,92} A. Fernández-Barral,¹ V. Fioretti,¹⁵ L. Foffano,^{36,1} V. Formato,²² N. Fornengo,^{67,68} L. Foschini,²⁵ A. Franceschini,³⁶ A. Franckowiak,⁴⁰ S. Funk,⁹³ F. Fuschino,¹⁵ D. Gaggero,⁵² G. Galanti,²⁵ F. Gargano,^{32,59} D. Gasparrini,^{46,22} R. Gehrz,⁹⁴ P. Giammaria,⁹² N. Giglietto,^{59,32} P. Giommi,⁹⁵ F. Giordano,³² M. Giroletti,⁸¹ G. Ghirlanda,^{25,96} N. Godinovic,⁹⁷ P. Gonçalves,⁷¹ C. Gouiffés,⁹⁸ J. E. Grove,⁹⁹ C. Hamadache,⁵ D. H. Hartmann,²⁸ M. Hayashida,¹⁰⁰ A. Hryczuk,⁶⁶ P. Jean,¹³ T. Johnson,¹⁰¹ J. José,¹⁰² S. Kaufmann,¹⁰³ B. Khelifi,¹⁰⁴ J. Kiener,⁵ J. Knödseder,¹³ M. Kole,¹⁰ J. Kopp,¹⁰⁵ V. Kozhuharov,⁶¹ C. Labanti,¹⁵ S. Lalkovski,⁶¹ J. Larsson,²⁰ P. Laurent,¹⁰⁶ O. Limousin,¹⁰⁷ M. Linares,¹⁰² T. Linden,²³ E. Lindfors,¹⁰⁸ M. Lindner,⁶⁵ J. Liu,¹⁰⁹ S. Lombardi,^{46,92} F. Loparco,^{32,59} R. López-Coto,¹ M. López Moya,⁵¹ B. Lott,¹¹⁰ P. Lubrano,²² J.M. Maia,⁷¹ D. Malyshev,¹¹¹ N. Mankuzhiyil,¹¹² K. Mannheim,⁸⁹ M. J. Marchã,¹¹³ A. Marcianò,⁴¹ B. Marcote,¹¹⁴ M. Mariotti,¹ M. Martinez,³⁹ M. Marisaldi,¹¹⁵ S. McBreen,¹¹ A. Merle,¹¹⁶ R. Mignani,^{117,118} G. Minervini,⁶ A. Moiseev,¹¹⁹ K. Nakazawa,¹²⁰ L. Nava,^{25,30,121} H. Neves,⁷¹ D. Nieto,⁵¹ M. Orienti,⁸¹ M. Orio,^{122,2} E. Orlando,³¹ P. Orleanski,¹²³ S. Paiano,² R. Paoletti,³⁷ A. Papitto,⁹² M. Pasquato,² B. Patricelli,^{124,37} M. Á. Pérez-García,⁴² M. Persic,¹²¹ G. Piano,⁶ A. Pichel,¹²⁵ M. Pimenta,⁴ C. Pittori,^{46,92} T. Porter,³¹ J. Poutanen,¹⁰⁸ E. Prandini,^{36,1} N. Prantzos,¹²⁶ N. Produit,¹⁰ S. Profumo,¹²⁷ F. S. Queiroz,¹²⁸ S. Rainó,^{32,59} A. Raklev,⁶⁶ M. Regis,^{67,68} I. Reichardt,¹²⁹ Y. Rephaeli,^{130,131} W. Rodejohann,⁶⁵ G. Rodriguez Fernandez,⁸ M. Roncadelli,¹³² L. Roso,¹³³ A. Rovero,¹²⁵ R. Ruffini,¹³⁴ F. Ryde,¹³⁵ G. Sala,¹⁰² M. A. Sánchez-Conde,¹³⁶ A. Santangelo,¹³⁷ P. Saz Parkinson,^{138,139} T. Sbarrato,⁹⁶ A. Shearer,¹⁴⁰ R. Shellard,⁵⁰ K. Short,⁵² T. Siebert,⁷⁹ C. Siqueira,^{65,141} P. Spinelli,³² A. Stamerra,¹⁴² S. Starrfield,¹⁴³ A. Strong,⁷⁹ I. Strümke,¹⁴⁴ F. Tavecchio,²⁵ R. Taverna,³⁶ T. Terzić,⁸⁸ D. J. Thompson,²⁶ O. Tibolla,¹⁰³ D. F. Torres,^{145,146,147} R. Turolla,³⁶ A. Ulyanov,¹¹ A. Ursi,⁶ A. Vacchi,⁸² J. Van den Abeele,⁶⁶ G. Vankova-Kirilovai,⁶¹ C. Venter,⁶⁰ F. Verrecchia,^{46,92} P. Vincent,¹⁴⁸ X. Wang,¹⁴⁹ C. Weniger,⁵² X. Wu,¹⁰ G. Zaharijaš,¹⁵⁰ L. Zampieri,² S. Zane,¹⁵¹ S. Zimmer,^{152,10} and A. Zoglauer¹⁵³

¹*Istituto Nazionale di Fisica Nucleare, Sezione di Padova, I-35131 Padova, Italy*

²*INAF - Osservatorio Astronomico di Padova, I-35122, Padova, Italy*

³*Dipartimento di Matematica, Informatica e Fisica, Università di Udine, I-33100 Udine, Italy*

⁴*Laboratorio de Instrumentação e Partículas and Instituto Superior Técnico, Lisboa, Portugal*

⁵*CSNSM, CNRS and University of Paris Sud, F-91405, Orsay, France*

⁶*INAF/IAPS, via del Fosso del Cavaliere 100, I-00133, Roma, Italy*

⁷*University of Roma "Tor Vergata", I-00133, Roma, Italy*

⁸*Istituto Nazionale di Fisica Nucleare, Sezione di Roma "Tor Vergata", I-00133 Roma, Italy*

⁹*Institute of Physics and PRISMA Excellence Cluster,*

Johannes Gutenberg University Mainz, 55099 Mainz, Germany

¹⁰*University of Geneva, Switzerland*

¹¹*School of Physics, University College Dublin, Ireland*

¹²*INAF Headquarters, Viale del Parco Mellini, 84, I-00136, Roma, Italy*

¹³*IRAP Toulouse, 9 av. du Colonel-Roche - BP 44 346, F-31028 Toulouse Cedex 4, France*

¹⁴*Laboratoire AIM, CEA-IRFU/CNRS/Université Paris Diderot, C.E.A. Saclay, France*

¹⁵*INAF/OAS-Bologna, Via Gobetti 93, I-40129 Bologna, Italy*

¹⁶*Ioffe Institute, St.Petersburg 194021, Russia*

- ¹⁷ *Institute of Space Sciences (CSIC-IEEC), Campus UAB,
C/ Can Magrans s/n, 08193 Cerdanyola del Vallés (Barcelona), Spain*
- ¹⁸ *Max-Planck-Institut für Extraterrestrische Physik, Postfach 1312, 85741 Garching, Germany*
- ¹⁹ *DTU Space, National Space Institute, Technical University of Denmark, Kgs. Lyngby, Denmark*
- ²⁰ *KTH Royal Institute of Technology, Department of Physics,
and Oskar Klein Centre, AlbaNova University Centre, 10691 Stockholm, Sweden*
- ²¹ *Nicolaus Copernicus Astronomical Center, Polish Academy of Sciences, Bartycka 18, PL-00-716 Warszawa, Poland*
- ²² *Istituto Nazionale di Fisica Nucleare, Sezione di Perugia, I-06123, Perugia, Italy*
- ²³ *Stockholm University, Department of Physics, and Oskar Klein Centre,
AlbaNova University Centre, 10691 Stockholm, Sweden*
- ²⁴ *LIP, Departamento de Física Universidade de Coimbra, P-3004-516 Coimbra, Portugal*
- ²⁵ *INAF - Osservatorio Astronomico di Brera, I-23807 Merate, Italy*
- ²⁶ *NASA Goddard Space Flight Center, Greenbelt, MD 20771, USA*
- ²⁷ *ICE (CSIC-IEEC), Campus UAB, Carrer Can Magrans s/n,
E-08193 Cerdanyola del Valles, Barcelona, Spain*
- ²⁸ *Department of Physics and Astronomy, Clemson University, Clemson, SC 29634, USA*
- ²⁹ *Dipartimento di Fisica, Università di Trieste, I-34127 Trieste, Italy*
- ³⁰ *Istituto Nazionale di Fisica Nucleare, Sezione di Trieste, I-34127 Trieste, Italy*
- ³¹ *W.W. Hansen Experimental Physics Laboratory,
Kavli Institute for Particle Astrophysics and Cosmology, Stanford University, Stanford, CA, 94305, USA*
- ³² *Istituto Nazionale di Fisica Nucleare, Sezione di Bari, I-70126, Bari, Italy*
- ³³ *INAF/IASF, Via Bassini 15, I-20133 Milano, Italy*
- ³⁴ *Departament de Física Quàntica i Astrofísica, Institut de Ciències del Cosmos (ICCUB),
Universitat de Barcelona, IEEC-UB, Martí i Franquès 1, E08028 Barcelona, Spain*
- ³⁵ *Institute of Physics and Astronomy, University of Potsdam, 14476 Potsdam, Germany*
- ³⁶ *Dipartimento di Fisica e Astronomia “G. Galilei”, Università di Padova, I-35131 Padova, Italy*
- ³⁷ *Istituto Nazionale di Fisica Nucleare, I-56127, Pisa, Italy*
- ³⁸ *Dipartimento di Fisica “E. Fermi”, Università di Pisa, I-56127, Pisa, Italy*
- ³⁹ *IFAE-BIST, Edifici Cn. Universitat Autònoma de Barcelona, E-08193 Bellaterra, Spain*
- ⁴⁰ *Deutsches Elektronen Synchrotron (DESY), Platanenallee 6, D-15738, Zeuthen, Germany*
- ⁴¹ *Center for Field Theory and Particle Physics & Department of Physics, Fudan University, 200433 Shanghai, China*
- ⁴² *Department of Fundamental Physics and IUFFyM University of Salamanca, Plaza de la Merced s/n 37008 Spain*
- ⁴³ *Spanish Center for Pulsed Lasers (CLPU), M5 Bldg. Science Park, Villamayor, Salamanca (Spain)*
- ⁴⁴ *CIDMA, Dep. de Física, Univ. de Aveiro, Campus de Santiago, 3810-193 Aveiro, Portugal*
- ⁴⁵ *Inst. Telecomunicações, Campus de Santiago, 3810-193 Aveiro, Portugal*
- ⁴⁶ *Space Science Data Center, Agenzia Spaziale Italiana, I-00133, Roma, Italy*
- ⁴⁷ *Faculty of Electrical Engineering and Computing, University of Zagreb, Croatia*
- ⁴⁸ *Department of Physics, Middle East Technical University, Ankara, Turkey*
- ⁴⁹ *Eberhard-Karls Universität Tübingen, 72076 Tübingen, Germany*
- ⁵⁰ *Brazilian Center for Research in Physics, Rio de Janeiro, Brazil*
- ⁵¹ *Unidad de Partículas y Cosmología (UPARCOS),
Universidad Complutense, E-28040 Madrid, Spain*
- ⁵² *GRAPPA and Institute of Physics, University of Amsterdam,
Science Park 904, 1098XH Amsterdam, The Netherlands*
- ⁵³ *Center for Astrophysics, Guangzhou University, Guangzhou 510006, China*
- ⁵⁴ *Department of Astrophysics, University of Lodz, ul. Pomorska 149/153, 90-236 Lodz, Poland*
- ⁵⁵ *LLR, École Polytechnique, CNRS/IN2P3, 91128 Palaiseau, France*
- ⁵⁶ *Institut für Physik, Humboldt-Universität zu Berlin, D-12489 Berlin, Germany*
- ⁵⁷ *Università di Perugia, I-06123 Perugia, Italy*
- ⁵⁸ *ETH, Zürich, Switzerland*
- ⁵⁹ *Dipartimento di Fisica “M. Merlin” dell’Università e del Politecnico di Bari, I-70126, Bari, Italy*
- ⁶⁰ *North-West University, Potchefstroom, South Africa*
- ⁶¹ *Faculty of Physics, University of Sofia “St. Kl. Ohridski”, Sofia 1164, Bulgaria*
- ⁶² *RWTH Aachen University, D-52074 Aachen, Germany*
- ⁶³ *GSSI, L’Aquila, Italy*
- ⁶⁴ *Istituto Nazionale di Fisica Nucleare, Laboratori Nazionali del Gran Sasso, L’Aquila, Italy*
- ⁶⁵ *Max Planck Institut für Kernphysik, Postfach 103980, 69029 Heidelberg, Germany*
- ⁶⁶ *Department of Physics, University of Oslo, Box 1048, NO-0371 Oslo, Norway*
- ⁶⁷ *Dipartimento di Fisica, Università degli Studi di Torino, Via P. Giuria 1, 10125 Torino, Italy*
- ⁶⁸ *Istituto Nazionale di Fisica Nucleare, Sezione di Torino, Via P. Giuria 1, 10125 Torino, Italy*
- ⁶⁹ *Istituto Nazionale di Astrofisica, Osservatorio Astrofisico di Torino,
Strada Osservatorio 20, 10025 Pino Torinese, Italy*
- ⁷⁰ *Department of Physics & Astronomy, University of the Western Cape, Cape Town 7535, South Africa*

- ⁷¹LIP Portugal
- ⁷²LPC2E, University of Orléans, CNRS, France
- ⁷³School of Physics, Wits University, Johannesburg, South Africa
- ⁷⁴Space Science Division, Naval Research Laboratory, Washington, DC 20375-5352, USA
- ⁷⁵Max Planck Institut für Astrophysik, Garching D-85741, Germany
- ⁷⁶Space Research Institute, Moscow 117997, Russia
- ⁷⁷Instituto de Física Corpuscular (CSIC - Universitat de València)
c/ Catedrático José Beltrán, 2 E-46980 Paterna, Valencia, Spain
- ⁷⁸APC, Université Paris Diderot, CNRS/IN2P3, CEA/Irfu,
Observatoire de Paris, Sorbonne Paris Cité, France
- ⁷⁹Max Planck Institut für extraterrestrische Physik, D-85748 Garching, Germany
- ⁸⁰Department of Astronomy, Yale University, P.O. Box 208101, New Haven, CT 06520-8101, USA
- ⁸¹INAF/IRA Bologna, Via Gobetti 101, I-40129 Bologna, Italy
- ⁸²University of Udine and Istituto Nazionale di Fisica Nucleare GC di Udine, via delle Scienze, I-33100 Udine, Italy
- ⁸³INAF - Osservatorio Astronomico di Capodimonte, Salita Moiariello 16, I-80131 Napoli, Italy
- ⁸⁴INAF/IASF-Palermo, Italy
- ⁸⁵ISAC-CNR, Roma, Italy
- ⁸⁶Novosibirsk State University, 630090 Novosibirsk, Russia
- ⁸⁷ITEP, 117259 Moscow, Russia
- ⁸⁸University of Rijeka - Department of Physics, Radmile Matejčić 2, 51000 Rijeka, Croatia
- ⁸⁹University Würzburg, D-97074 Würzburg, Germany
- ⁹⁰Laboratoire de Physique Théorique, CNRS – UMR 8627,
Université de Paris-Saclay 11, F-91405 Orsay Cedex, France
- ⁹¹University of Wuerzburg, Germany
- ⁹²INAF - Osservatorio Astronomico di Roma, I-00078, Monte Porzio Catone, Italy
- ⁹³Erlangen Centre for Astroparticle Physics, D-91058 Erlangen, Germany
- ⁹⁴University of Minnesota, Minneapolis, MN 55455, USA
- ⁹⁵Agenzia Spaziale Italiana, Roma, Italy
- ⁹⁶Dipartimento di Fisica G. Occhialini, Università di Milano Bicocca, Piazza della Scienza 3, I-20126 Milano, Italy
- ⁹⁷University of Split, Croatia
- ⁹⁸Laboratoire AIM, UMR 7158, CEA/DRF, CNRS,
Université Paris Diderot, IRFU/Sap, F-91191 Gif-sur-Yvette, France
- ⁹⁹U.S. Naval Research Laboratory, 4555 Overlook Ave SW, Washington, DC 20375, USA
- ¹⁰⁰Institute for Cosmic Ray Research, the University of Tokyo, Kashiwa, Chiba, 277-8582, Japan
- ¹⁰¹College of Science, George Mason University, Fairfax, VA 22030, USA,
resident at Naval Research Laboratory, Washington, DC 20375, USA
- ¹⁰²Departament de Física, EEBE, UPC, 08019 Barcelona, Spain
- ¹⁰³Mesoamerican Center for Theoretical Physics (MCTP),
Universidad Autonoma de Chiapas (UNACH), 29050 Tuxtla Gutierrez, Chiapas, Mexico
- ¹⁰⁴Laboratoire APC, 10, rue Alice Domon et Léonie Duquet, 75013 Paris
- ¹⁰⁵Johannes Gutenberg-Universität Mainz, 55099 Mainz, Germany
- ¹⁰⁶Laboratoire APC, UMR 7164, CEA/DRF CNRS, Université Paris Diderot, Paris, France
- ¹⁰⁷CEA/Saclay IRFU/Department of Astrophysics, Bat. 709, F-91191, Gif-Sur-Yvette, France
- ¹⁰⁸Tuorla observatory, University of Turku, FIN-21500 Piikkiö, Finland
- ¹⁰⁹Enrico Fermi Institute, University of Chicago, Chicago, IL 60637, USA
- ¹¹⁰IN2P3/CNRS, Université Bordeaux 1, BP120, Gradignan Cedex, France
- ¹¹¹Erlangen Centre for Astroparticle Physics, Erwin-Rommel-Str. 1, Erlangen, Germany
- ¹¹²Astrophysical Sciences Division, BARC, Mumbai - 400085, India
- ¹¹³Department of Physics and Astronomy, University College London, Gower Street, London WC1E 6BT, UK
- ¹¹⁴Joint Institute for VLBI ERIC, Postbus 2, 7990 AA Dwingeloo, The Netherlands
- ¹¹⁵University of Bergen, Norway
- ¹¹⁶Max-Planck-Institut für Physik, 80805 Munich, Germany
- ¹¹⁷INAF-Istituto di Astrofisica Spaziale, Milano, Italy
- ¹¹⁸University of Zielona Gora, Poland
- ¹¹⁹CRESST/NASA/GSFC and University of Maryland, College Park, USA
- ¹²⁰Department of Physics, the University of Tokyo, 7-3-1 Hongo, Bunkyo-ku, Tokyo 113-0033
- ¹²¹INAF - Osservatorio Astronomico di Trieste, via G. B. Tiepolo 11, I-34143 Trieste, Italy
- ¹²²Department of Astronomy, University of Wisconsin, Madison WI 53704, USA
- ¹²³Space Research Center of Polish Academy of Sciences, Bartycza 18a, PL-00-716 Warszawa, Poland
- ¹²⁴Scuola Normale Superiore, I-56126, Pisa, Italy
- ¹²⁵Instituto de Astronomía y Física del Espacio (IAFE, CONICET-UBA), Buenos Aires, Argentina
- ¹²⁶Institut d'Astrophysique de Paris, F-75014, Paris, France
- ¹²⁷Department of Physics and Santa Cruz Institute for Particle Physics,
University of California, Santa Cruz, CA 95064, USA

- ¹²⁸ *International Institute of Physics, Federal University of Rio Grande do Norte, Campus Universitário, Lagoa Nova, Natal-RN 59078-970, Brazil*
- ¹²⁹ *Universitat Rovira i Virgili, Carrer de l'Escorxador, E-43003 Tarragona, Spain*
- ¹³⁰ *School of Physics, Tel Aviv University*
- ¹³¹ *CASS, UC San Diego*
- ¹³² *Istituto Nazionale di Fisica Nucleare, Sezione di Pavia, Via A. Bassi 6, I-27100 Pavia, Italy, and INAF*
- ¹³³ *University of Salamanca (USAL), Plaza de la Merced s/n, 37008, Salamanca (Spain)*
- ¹³⁴ *ICRANET Roma, Italy*
- ¹³⁵ *Oskar Klein Centre for Cosmoparticle Physics Fysikum, Stockholm University AlbaNova University Centre, SE-10961, Stockholm, Sweden*
- ¹³⁶ *Instituto de Física Teórica (IFT UAM-CSIC) and Departamento de Física Teórica, Universidad Autónoma de Madrid, ES-28049 Madrid*
- ¹³⁷ *Institute of Astronomy and Astrophysics, University of Tübingen, Germany*
- ¹³⁸ *Santa Cruz Institute for Particle Physics, University of California, Santa Cruz, CA, USA*
- ¹³⁹ *Dept. of Physics & Laboratory for Space Research, University of Hong Kong, Hong Kong*
- ¹⁴⁰ *Centre for Astronomy, NUI Galway, Ireland*
- ¹⁴¹ *Departamento de Física, Universidade Federal da Paraíba, Caixa Postal 5008, 58051-970, João Pessoa, PB, Brasil*
- ¹⁴² *Scuola Normale Superiore, Pisa, I-56126, Italy*
- ¹⁴³ *Arizona State University, Tempe, AZ 85287-1504, USA*
- ¹⁴⁴ *University of Bergen, Institute for Physics and Technology, Postboks 7803, N-5020 Bergen, Norway*
- ¹⁴⁵ *Institute of Space Sciences (ICE, CSIC), Campus UAB, Carrer de Magrans s/n, 08193 Barcelona, Spain*
- ¹⁴⁶ *Institució Catalana de Recerca i Estudis Avançats (ICREA), E-08010 Barcelona, Spain*
- ¹⁴⁷ *Institut d'Estudis Espacials de Catalunya (IEEC), 08034 Barcelona, Spain*
- ¹⁴⁸ *LPNHE, CNRS/IN2P3 and Université Pierre et Marie Curie, F-75252 Paris, France*
- ¹⁴⁹ *High Energy Physics Division, Argonne National Laboratory, Argonne, IL 60439, USA*
- ¹⁵⁰ *Center for Astrophysics and Cosmology, University of Nova Gorica, Nova Gorica, Slovenia*
- ¹⁵¹ *Mullard Space Science Laboratory, University College London, Holmbury St. Mary, Dorking, Surrey, RH5 6NT, UK*
- ¹⁵² *Institute of Astro- and Particle Physics, University of Innsbruck, Innsbruck, AT 6020, Austria*
- ¹⁵³ *University of California at Berkeley, Space Sciences Laboratory, 7 Gauss Way, Berkeley, CA 94720, USA*